DECONVOLUTION ALGORITHMS FOR FLUORESCENCE AND ELECTRON MICROSCOPY

by

Siddharth Shah

A dissertation submitted in partial fulfillment
of the requirements for the degree of
Doctor of Philosophy
(Biomedical Engineering)
in The University of Michigan
2006

Doctoral Committee:

Professor Andrew E. Yagle, Chair
Professor Paul L. Carson
Professor Jeffrey A. Fessler
Associate Professor Mary-Ann Mycek
Associate Professor Douglas C. Noll

ACKNOWLEDGEMENTS

This work has been possible only due to the support of several faculty, family members and friends. First, I would like to thank my adviser Andrew Yagle for the support and guidance when I needed them most and for supporting my decision to work toward my thesis at UCSF. I would like to thank John Sedat and David Agard for their tremendrous generosity in letting me work in their microscopy labs for a year. I also thank my committee members Mary-Ann Mycek, Jeffrey Fessler, Douglas Noll and Paul Carson for their insights and guidance. I want to thank Michelle Young for being a wonderful person to work with.

I am grateful to my colleagues Erik Hom, Sebastian Haase, Shawn Zheng, John Lyle and Justin Kollman who helped me in key ways on the electron microscopy projects. Last, I want to thank my family and friends. My brother, Ashwin and sister-in-law Indrayani gave me tremendous moral support, encouragement and most importantly fed me tasty Indian dishes which I by no means can cook ! My parents must be thanked for their support and faith in me when the chips were down. My friends Kurt Christensen, Ken Garber, Josh Hoskins, Rajeeva Kumar and Neal Patwari helped me at various stages of my PhD. To them, a hearty thanks !

TABLE OF CONTENTS

LIST OF FIGURES

Figure

LIST OF TABLES

Table

CHAPTER I

Introduction

For the past three decades, optical and electron microscopy (EM) have been the tools of choice for viewing cellular and sub-cellular biological structures. One of the key challenges in both of these imaging techniques is in viewing the specimen of interest at the highest resolution and contrast. While increasing the laser beam excitation in fluorescence microscopy or electron beam intensity in the case of EM increases both contrast and resolution, it is not possible to do so indiscriminately. High fluorescence excitation from a laser beam can cause photobleaching and permanently damage the specimen. Similarly, high electron beam radiation damages delicate specimen. Thus, the challenge is to develop methods that preserve the specimen while allowing them to be imaged at the desired resolution.

In all imaging systems, two factors ultimately limit the resolution of the image: noise; and the the non-ideal response of the imaging system. Deconvolution refers to a class of computational methods that aim to improve the contrast and resolution of recorded images by reducing the effect of both of these factors. This approach to resolution and contrast enhancement is attractive for two key reasons. First, it is inexpensive, requiring little capital expenditure. Second, it is easy to deploy. A new algorithm can be developed and deployed within weeks. Due to these advantages,

deconvolution has been an area of intense research in the fields of astronomy, biology, geology, mathematics and engineering, and numerous deconvolution algorithms have been developed over the past thirty years. For an overview, the reader is referred to [76, 55, 4] .

Several technological improvements have revolutionized both optical and electron microscopy in recent years. Optical microscopes have become very fast with some of them able to image almost real time in 3-D at tens of frames per second. Electron microscopes have become less noisy and techniques have been developed to analyze large molecules at atomic resolution. At the same time, improvements in CCD technology have enabled images to be captured and stored digitally at high resolutions. Images captured with these microscopes after a successful deconvolution would potentially enable imaging at unprecedented spatial and temporal resolution. Unfortunately, conventional deconvolution algorithms are slow and are not suitable for high throughput applications. Further, deconvolution algorithms for electron microscopy which are suitable for low-resolution images, are not very effective with high resolution images.

In this thesis, we aim to address these problems by developing and exploring deconvolution algorithms that are fast and easy to deploy. We show through simulations and experiments on experimental data that our algorithms are able to deconvolve images successfully, often better than conventional techniques.

1.1 Problem Overview

Conventional deconvolution algorithms are slow because they are iterative, requiring many iterations to give a good result. Most of these algorithms require measurement of the system response, also known as the transfer function, a time-

consuming and often difficult task. This makes them unsuitable for use in high throughput applications where images have to be deconvolved quickly. Hence, there is a need for non-iterative algorithms that can preferably deconvolve without the transfer function information.

In EM, deconvolution is even more difficult, due to the very high noise levels of these images. Many conventional algorithms overcome this by making unrealistic assumptions which ultimately limit their effectiveness. The problem is exacerbated by the fact that few algorithms have been developed that can estimate the transfer function accurately. Thus, a good transfer function estimation method, coupled with an effective deconvolution algorithm, would be an effective solution to this problem.

1.2 Previous Work

1.2.1 Optical Microscopy

One of the first deconvolution algorithms to be applied to optical microscopy was the Van Cittert algorithm [1]. While fast, this algorithm does not promise convergence and requires a good initial guess to give good results. Since then, several deconvolution algorithms have been developed that fall roughly into two categories: linear methods; and statistically derived methods.

Linear methods such as linear least squares, constrained least squares and Wiener filtering, while simple to implement and fast, are commonly used in the context of fluorescence microscopy [55]. Unfortunately, most linear methods suffer from two problems. First, they are not very effective in restoring all spatial frequencies of interest. This is especially problematic for the deconvolution of wide-field optical microscopy images due to the 'missing cone" problem [81]. Second, they overblur the recovered image.

Statistically derived maximum-likelihood (ML) and maximum a posteriori (MAP)

algorithms are more sophisticated, as they allow the imaging noise to be modeled and accounted for in the reconstruction. They may also allow some information about the properties of the object to be included in the problem formulation[13, 54, 32, 33]. Unfortunately, while these methods often provide excellent reconstructions, their iterative nature makes them very slow [55].

All the above methods require the estimation of the transfer function, also known as the Point Spread Function (PSF) of the microscope, which is a measure of the fidelity with which information is transferred from the input to the output of the instrument. Although the form of the PSF is analytically well known, measuring it accurately can be difficult and time consuming [55, 30]. Two potential classes of algorithms attempt to solve this problem. The first, myopic deconvolution algorithms, account for errors in the measured PSF and are partially able to overcome inaccuracies in its measurement [31, 59]. The second, blind deconvolution algorithms, attempt to deconvolve the image without any PSF information. This is a significantly more difficult problem than the other methodologies, and as a result it is relatively unexplored. Further, both myopic and blind algorithms are slow [30].

1.2.2 Electron Microscopy

Deconvolution of EM images is more difficult than the optical case, for two reasons. First, the images here are very noisy. In the case of cryogenic images, signal to noise ratios (SNR) of 0 dB are quite common. Second, due to the low SNR, estimation of the transfer function is very difficult. Without a good transfer function estimate, most deconvolution algorithms will not give good object estimates.

Most algorithms developed in the field use Wiener filtering and its variants [49, 56, 14, 19, 6]. As in optical microscopy, these algorithms overblur the recovered images. Another common approach is to use "phase-flipping" algorithms [56, 80]. While

simple to implement, these algorithms only correct for the phase distortions induced by the transfer function. Moreover, many of these algorithms assume unrealistically that astigmatism is absent in the system.

1.3 Contributions of this Thesis

In this thesis we develop and test four new algorithms. They are as follows:

- The first algorithm is a blind deconvolution algorithm that assumes that the PSF is even, a reasonable assumption for many optical applications. This assumption allows us to decompose the 2-D and 3-D blind deconvolution problem into many small 1-D problems, which in turn speeds up the algorithm significantly. We demonstrate that due to its speed, it become tractable to deconvolve large images in a matter of minutes.

- The second algorithm is also a blind deconvolution technique that assumes that the object can be represented by the a "QUILL" (Quincunx Upsampled Linearly Interpolated) image model. This assumption allows us to break up the problem into a four-blur problem, which can be solved quickly using well-established results in multichannel blind deconvolution. This algorithm is well-suited to large oversampled images at relatively high SNRs. These images are common in fluorescence microscopy.

- The third algorithm is a transfer function estimation algorithm for cryo-EM (cryo-EM) images. While several algorithms of the same class have been developed, this algorithm is unique for several reasons. First, this algorithm performs the estimation in two dimensions, unlike most other algorithms that radially average the transfer function to increase the SNR of the transfer function image. This is significant because radial averaging assumes astigmatism is absent in the

system, an assumption that is not true in most cases. Second, this algorithm is the only algorithm that can estimate transfer functions for tilted images. Third, this is one of two algorithms that has been developed with a Graphic User Interface (GUI) and built on an Open Source Numerical Python platform. This is significant because including the GUI makes the program easy to use for biologists who do not have programming experience.

- The final algorithm deconvolves EM images using an edge-preserving regularizer. We demonstrate that the algorithm reduces noise, while at the same time it preserves high-frequency object information such as edges better than other state of the art algorithms used in EM.

1.4 Organization of this Thesis

In Chapter II, we introduce the physics of image formation for both fluorescence and electron microscopes. In Chapter III we develop the mathematical framework of deconvolution and discuss conventional deconvolution techniques. In Chapters IV-VI, blind deconvolution algorithms are introduced that are suitable for 2-D and 3-D fluorescence and optical microscopy. In Chapter VII, we present an automatic transfer function determination algorithm for electron microscopy. In Chapter VIII, we introduce an edge-preserving deconvolution algorithm and apply it to EM images. Finally in Chapter IX, we present our conclusions and directions for future work.

CHAPTER II

Principles of confocal and electron microscopy

Biomedical imaging has made significant advances in recent decades. While it was advances in physics that primarily led to new imaging modalities such as Magnetic Resonance Imaging (MRI) and PET (Positron Emission Tomography) among others, it was the digital revolution that extended the resolution of both new and time-honored imaging techniques such as light microscopy.

Computational resolution extension algorithms for digital images, also known as *deconvolution* algorithms, we first pioneered by astronomers in the early seventies [48, 68]. Unfortunately, CCD technology at this time was not at a point at which it could be used for biological imaging applications. This precluded the use of computational methods. It was only by the late eighties that the first deconvolution algorithms for optical microscopy appeared. The algorithms of Jansson Van Cittert [41] and others were adapted from well-established algorithms in astronomy and statistics. With growing computational power, starting in the nineties, deconvolution has now become an integral part of light and fluorescence microscopy [55].

The use of deconvolution for electron microscopy (EM) images has not been explored very much. This is due to two reasons: (1) Digital image capture and storage is a relatively new technology in the EM area; (2) Until recently, EM images have

been very noisy. Conventional deconvolution algorithms would not have improved the image quality very much. However, recent advances in EM hardware have made these issues a thing of the past.

2.1 Introduction

2.1.1 The Confocal Microscope

Figure (2.1) shows a schematic diagram of a Laser Scanning Confocal Microscope (LSCM),a commonly used microscope for fluorescence imaging. In LSCM, a laser light beam is turned to a scanning beam and focused to a small spot by an objective lens onto a fluorescent specimen. The fluorescent molecules in the illuminated object are excited by incident light wavelength λ_{ex}. The excited molecules emit light of wavelength λ_{em}. The difference $\delta\lambda = \lambda_{em} - \lambda_{ex} > 0$ between emitted and excitation wavelength is called the Stokes shift of the fluorescent molecule.

The mixture of reflected light and emitted fluorescent light is captured by the same objective, and after conversion into a static beam by the x-y scanner device, it is focused onto a photo detector (photomultiplier) via a dichroic mirror (beam splitter). The reflected light is deviated by the dichroic mirror, while the emitted fluorescent light passes through in the direction of the photomultiplier. A confocal aperture (pinhole) is placed in front of the photo detector, so that the fluorescent light from points on the specimen that are not within the focal plane are largely obstructed by the pinhole. In this way, out-of-focus information (both above and below the focal plane) is greatly reduced. A lateral scan of the sample yields a 2-D image. A lateral and axial scan yields a 3-D image.

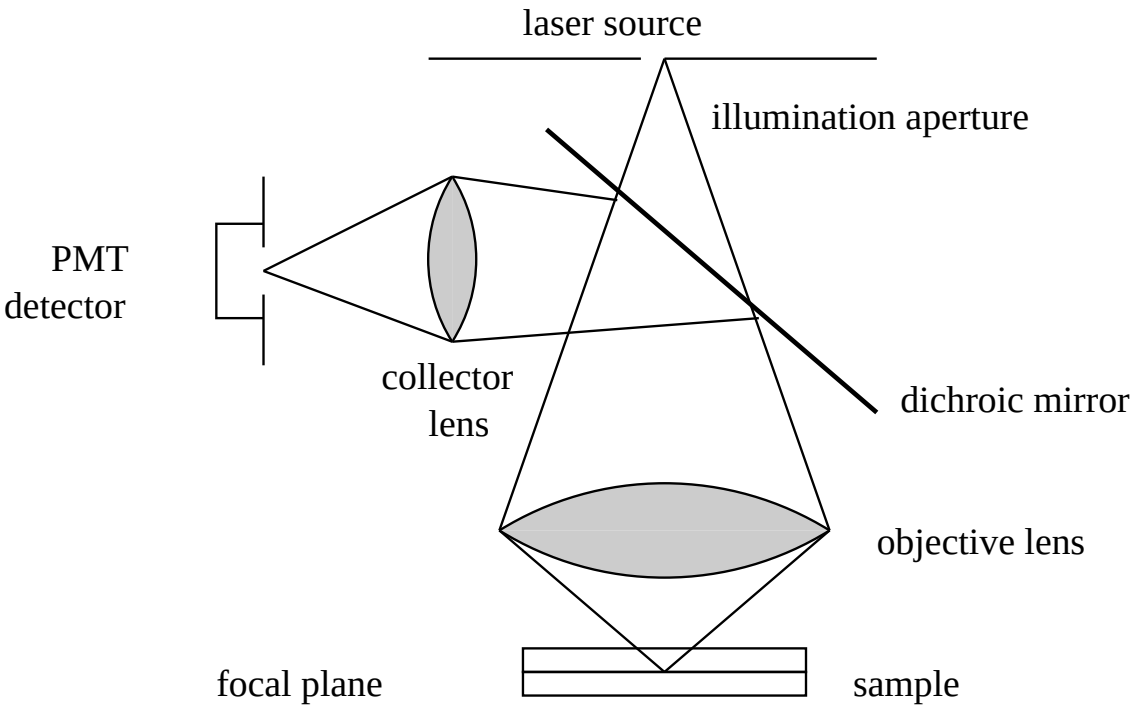

Figure 2.1: Schematic diagram of a laser scanning confocal microscope (LSCM)

2.1.2 The Transmission Electron Microscope

The principle behind the Transmission Electron Microscope (TEM) is similar to that of the compound microscope in optics. As seen in Figure 2.2, a thermionic, Schottky or field emission electron gun emits electrons. A condenser lens system between the specimen and the electron gun ensures that the electron energy is optimally transferred to the specimen. After irradiating the specimen, the electrons contain both phase and amplitude information about the sample. The emergent electrons are then projected onto a photographic plate or a CCD array for recording using a three-lens system.

In light microscopy, two stages of magnification is the norm, as the resolution of the image is limited by the wavelength of light and the required magnification can be obtained by using a two-lens system. In the electron microscope, however, the

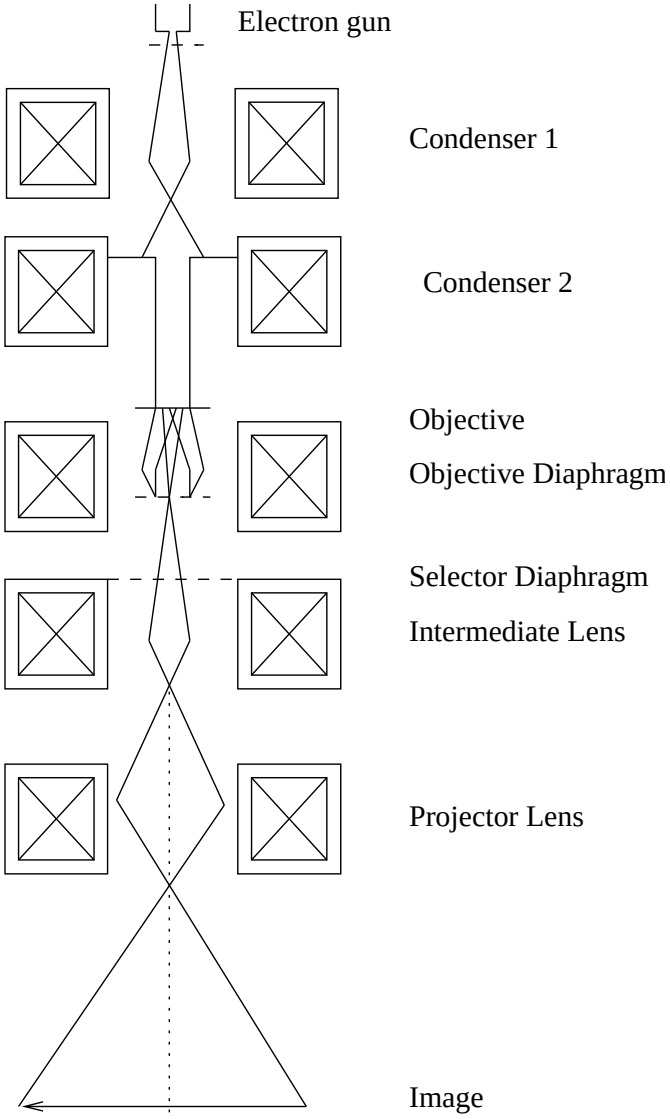

Figure 2.2: Schematic ray path for a transmisson Electron Microscope (TEM). Adapted from [67].

resolution is only limited by the spherical aberration of the lens, and not by the wavelength of the electrons. Hence, three stages of magnification are needed to bring the high magnifications necessary to bring the resolving power of the instrument up to the resolving power of the eye.

The *objective* lens is a strong lens of short focal length that forms the primary image of the specimen. This image is the object for the *intermediate* lens that is a relatively weak lens of adjustable focal length. The image formed by the intermediate lens is then the object for the *projector* lens that performs the final stage of magnification.

Electron microscopy is a coherent imaging method where the emergent electron beam has both phase and amplitude information. Although the mathematical analysis of coherent imaging is different from incoherent imaging, we shall show that for typical imaging conditions of biological samples the EM imaging equation is very similar to the incoherent imaging equation.

2.1.3 Image Formation Processes in EM: A Qualitative Description

In EM, four physical processes, absorption, scattering, interference and diffraction contribute to image formation. Absorption gives rise to amplitude contrast, interference gives rise to phase effects, diffraction leads to formation of haloes and fringes and scattering results in the formation of phase contrast. Diffraction is not discussed in detail, as it is not an important process in EM image formation.

Scattering

Fast electrons passing through a specimen can interact either with the specimen nucleii or with the electron cloud surrounding the nucleus. Due to the large mass difference betweent the nucleus and electron, a fast electron passing close to the

nucleus is deflected by a large angle, suffering almost no energy loss. On the other hand, a fast electron interacting with the slow electron orbiting the nucleus shares its velocity with the slow electron, due to the law of conservation of angular momentum, thereby suffering a change of direction and energy. Interactions of the first type are known as elastic scatter, while the latter type of interactions are known as inelastic scatter.

Scattering is the most important of all image formation processes in the electron microscope, since it is the interference between the scattered and the unscattered wave that leads to the development of a phase contrast.

Absorption

Absorption results in the formation of contrast based on mass-density. High mass-density areas in the image plane appear dark, due to high local absorption of electrons and low mass density areas. That is, electron-transparent areas appear brighter, due to low absorption of electrons. Absorption is not an important factor for thin biological specimens, as an electron has to encounter a whole series of inelastic collisions for absorption.

Interference

For thin samples, which are typical in biological EM imaging, interference is an important image formation process. Interference effects arise due to the following two causes:

- Spherical Abberration: The objective lens of the electron microscope has an uncorrectable spherical aberration. As a result, the path length of the electron beam passing through the periphery of the lens is longer than that of the beam passing through the center. Thus rays from the same point can interfere,

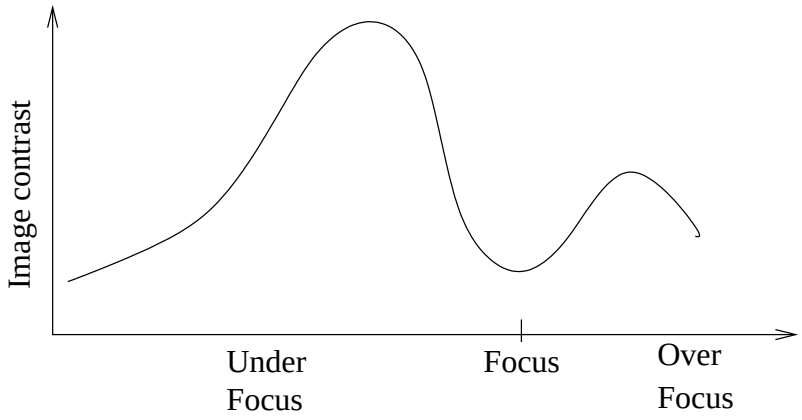

Figure 2.3: Variation of image contrast with objective lens focus. Defocussing increases the contrast of the image at the expense of resolution.

resulting in differences in intensity in the image plane. This effect is only observable close to the absolute limit of the resolution of the lens, and leads to fine image granularity. Interference due to spherical aberration determines the microscope's ultimate resolving power.

- Defocussing: "Defocus contrast" refers to increase in contrast on either side of the point of true focus. It is due to the formation of the Fresnel fringes about any parts of the specimen where there is a rapid change in mass thickness. The fringes enhance the lines and points resulting in an image of better contrast. Unfortunately, defocussing also lowers the highest resolution attainable, and may cause artifacts that appear to be "resolved" especially in images of regular structures.

For biological samples, poor amplitude contrast necessitates artificial contrast enhancement by defocusing. However, due to the resolution-contrast tradeoff, the appropriate defocus must be chosen carefully. Figure 2.3 shows the variation of contrast with the defocus.

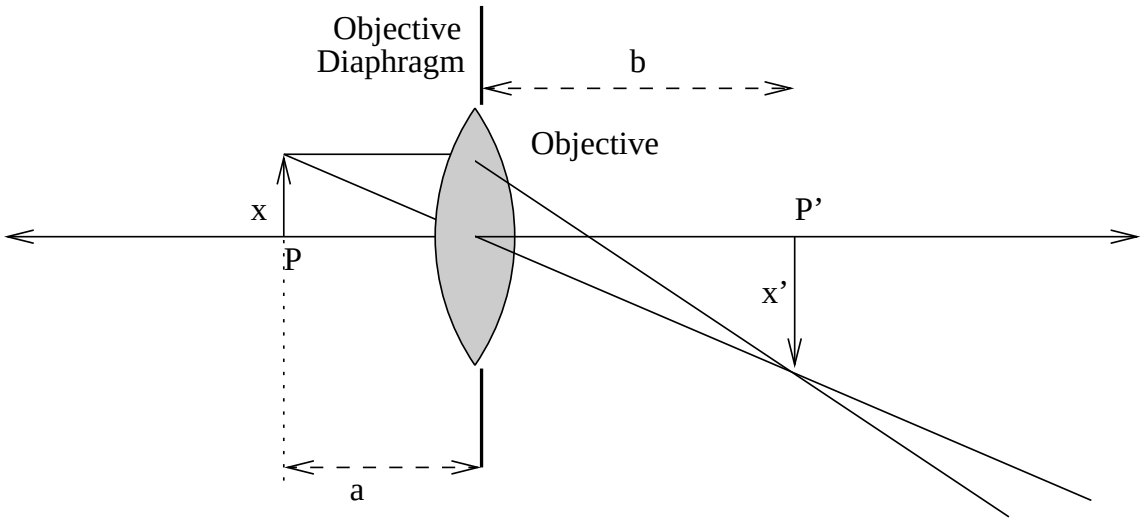

Figure 2.4: Schematic diagram of image formation.

2.2 Wave Optical Theory of Imaging

Fluorescence confocal microscopy is an incoherent imaging technique, and electron microscopy (EM) is a coherent imaging method. While the physical imaging processes for both optical and electron microscopy are very different, they can be expressed by the same equation using the wave optical theory of imaging.

Consider Figure (2.4), where the rays from an object point P are reunited by the lens at the image point P' at a distance x'=-Mx from the optic axis, x being the off-axis distance of P and M=b/a=magnification. Rays with equal scattering angles from different points of the specimen intersect in the focal plane of the lens. By Fraunhofer's approximation, the wave amplitude $F(\mathbf{q})$ in this plane is obtained from the exit wave amplitude distribution $\psi_s(\mathbf{r})$ behind the specimen by a Fourier transform. In other words,

$$F(\mathbf{q}) = \int_s \psi_s(\mathbf{r}) e^{-2\pi i(\mathbf{q}.\mathbf{r})} d^2\mathbf{r} \tag{2.1}$$

In aberration free imaging, the wave amplitude ψ_m at the image point P' is obtained

by integrating over all elements of area $d^2\mathbf{q}$ of the focal plane

$$\psi_m(\mathbf{r}) = \frac{1}{M}\int\int F(\mathbf{q})e^{2\pi i\mathbf{q}.\mathbf{r}}d^2\mathbf{q} = \frac{1}{M}\psi_s(\mathbf{r}) \tag{2.2}$$

In other words, $\psi_m(\mathbf{r})$ is the inverse Fourier transform of $F(\mathbf{q})$. In aberration free imaging there will be no further phase shift. In practice, a maximum scattering angle $\theta_{max} = \alpha_0$ (objective aperture) corresponding to a maximum spatial frequency q_{max} is used. The limitation on spatial frequencies by an objective diaphragm can be expressed by a multiplicative masking $M(q) = 1$ for $q = |\mathbf{q}| < q_{max}$ and $M(q) = 0$ otherwise in the normal bright field mode.

If wave abberation is only a function of $\mathbf{q}$, the action of this contribution can be represented as a multiplication of amplitudes in the focal plane by a phase factor $e^{-iW(q)}$. We rewrite the wave amplitude at P' as

$$\psi_m(\mathbf{r}) = \frac{1}{M}\int\int F(\mathbf{q})\left[e^{-iW(q)}M(q)\right]e^{2\pi iq.r}d^2\mathbf{q} = \frac{1}{M}\psi_s(\mathbf{r}) \tag{2.3}$$

We set $H(q) = \left[e^{-iW(q)}M(q)\right]$. $H(q)$ is known as the pupil function. Setting $h(r) = F^{-1}(H(q))$, (the inverse Fourier transform of the pupil function), we can write

$$\psi_m(r') = \frac{1}{M}\psi_s(\mathbf{r}) \otimes h(\mathbf{r}) \tag{2.4}$$

where $\otimes$ is the convolution operator. $h(r)$ is known as the point spread function (PSF).

(2.4) is a general form of image formation equation. In the case of incoherent image formation, such as fluorescence microscopy, we are only concerned about the intensity of $\psi_m(\mathbf{r}')$. Hence the distribution can be written as a scalar. The ideal intensity image for a confocal microscope can be expressed as [51]

$$i(\mathbf{r}) = h(\mathbf{r}) \otimes o(\mathbf{r}) \tag{2.5}$$

where $i(\mathbf{r})$ is the image, $o(\mathbf{r}$ is the object. Using scalar ordinate variables, the 2-D PSF is given by [51]

$$h(\mathbf{r}) = F^{-1}\left[|H_1(q,\phi)|^2|H_2(q,\phi)|^2\right]. \tag{2.6}$$

Here $H_1(q,\phi)$ is the Fourier transform of the point spread function of the objective lens, $H_2(q,\phi)$ is the Fourier transform of the point spread function of the collector lens, q is the spatial frequency and ϕ is the angle ordinate in the frequency plane.

Applying the Fourier transform, (2.5) can be expressed a multiplicative process in the frequency plane as

$$I(q,\phi) = H(q,\phi)O(q,\phi) \tag{2.7}$$

where q, ϕ are the radial ordinates in the spatial frequency plane.

In the case of EM the imaging equation is not as simple due to the coherence in the image formation process. Fortunately, for thin biological specimen, the imaging equation can be approximated to a form identical to (2.7). We shall derive the EM imaging equation in the next section.

2.3 Derivation of EM Imaging Equation

2.3.1 Angular Deviation of Wavefront in an Electron Lens

When a wavefront passes through an electron lens, it is subject to an angular deviation causing a phase shift in the wavefront. The angular deviation has three causes:

- Spherical abberation: $\epsilon_s = \frac{C_s R^3}{f^4}$, C_s being the spherical aberration coefficient, f being the focal length and R being the distance of the lens from the optic axis.
- Change in specimen position $\epsilon_a = \frac{\Delta a R}{f^2}$, a being the distance of the object from the lens and Δa being the change in specimen position.

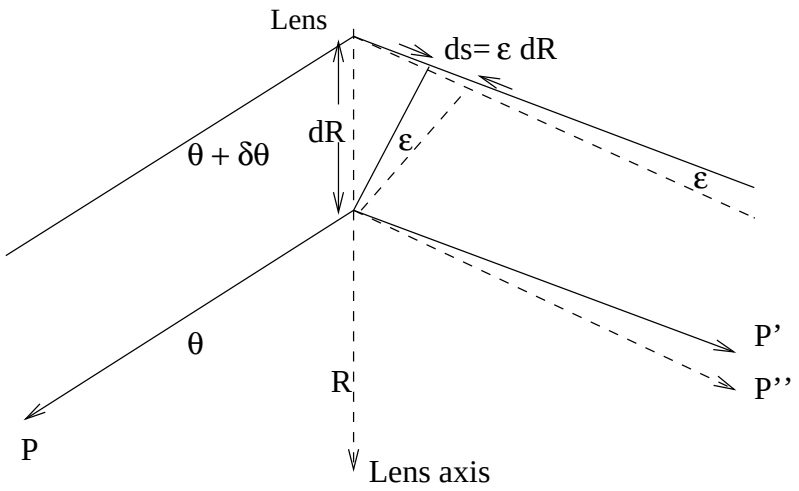

Figure 2.5: Part of the outer zone of a lens shown the relationship between angular deviation ϵ and optical path difference $ds = \epsilon dR$. Adapted from [67]

- Change in focal length $\epsilon_f = \frac{-\Delta f R}{f^2}$, Δf being the change in focal length.

Summing these up, we get the total angular deviation as [67]

$$\epsilon = \epsilon_s + \epsilon_A + \epsilon_f = \frac{C_s R^3}{f^4} - \frac{(\Delta f - \Delta a)R}{f^2}. \tag{2.8}$$

2.3.2 Derivation of Phase Shift

Figure (2.5) shows an enlargement of a part of the lens between two trajectories, and their orthogonal wavefronts, which reaches the lens at distances R and R+dR from the optical axis. The angular difference causes an optical path difference $ds = \epsilon dR$ between the two trajectories. These path differences ds have to be summed to get the total path difference Δs or the phase shift $W(\theta)$ relative to the optic axis. In other words

$$W(\theta) = \frac{2\pi \Delta s}{\lambda} = \frac{2\pi}{\lambda}\int_0^R ds = \frac{2\pi}{\lambda}\int_0^R \epsilon dR \tag{2.9}$$

θ being the scattering angle. We write this as

$$W(\theta) = \frac{2\pi}{\lambda}\left[\frac{1}{4}\frac{C_s R^4}{f^4} - \frac{1}{2}\frac{(\Delta f - \Delta a)R^2}{f^2}\right]. \tag{2.10}$$

We approximate $R/f \approx \theta$ (θ being the deflection angle) and defocussing $\Delta z = \Delta f - \Delta a$. Substituting we get the Scherzer formula [67]

$$W(\theta) = \frac{\pi}{2\lambda}(C_s\theta^4 - 2\Delta z\theta^2) \tag{2.11}$$

Conventionally, when $\Delta z < 0$ it is called overfocussing, and when $\Delta z > 0$ it is called underfocussing. Introducing the spatial frequency $q = \theta/\lambda$ (its derivation comes from wavefront theory) we get

$$W(q) = \frac{\pi}{2}(C_s\lambda^3 q^4 - 2\Delta z\lambda q^2) \tag{2.12}$$

Finally, we introduce an additional term for axial astigmatism

$$W_A = -\frac{\pi}{2}q^2\lambda\Delta f_{diff}\cos\left[2(\phi - \phi_a)\right] \tag{2.13}$$

where ϕ is the azimuthal angle, χ_0 is the azimuthal angle for the direction of defocus, Δf_{diff} is the amount of focus difference due to astigmatism. We approximate $\Delta z \approx \Delta f_{mean}$. Hence, the total phase is now

$$W(q) = \frac{\pi}{2}\left[C_s q^4\lambda^3 - \lambda q^2(2\Delta f_{mean} + \Delta f_{diff}\cos(2\phi - 2\phi_a))\right] \tag{2.14}$$

2.3.3 Weak Amplitude Weak Phase Approximation

By Fraunhoffer's approximation, the exit wave amplitude after passing through a specimen can be described by

$$\psi = \psi_o a_s(\mathbf{r})e^{i\varphi_s(\mathbf{r})}e^{2\pi ikz} = \psi_s e^{2\pi ikz} \tag{2.15}$$

where r is the radius vector in the specimen plane from the origin on the optic axis, $a_s(\mathbf{r})$ is the local decrease of amplitude due to absorption, and $\varphi_s(\mathbf{r})$ is the phase shift caused by the specimen[67]. We normalize the amplitude ψ_o to unity. Next we assume that the sample is thin, so that there is a very small amount of absorption.

Hence, we can assume $a_s(\mathbf{r}) = 1-\epsilon_s(\mathbf{r})$ where $\epsilon_s(\mathbf{r})$ is small. Assuming that the phase shift is also much less than one, the exponential term in (2.15) can be expressed as

$$\psi(\mathbf{r}) = 1 - \epsilon_s(\mathbf{r}) + i\varphi_s(\mathbf{r}) + \dots \tag{2.16}$$

With this approximation, the object is said to be weak-phase-weak-amplitude.[79] In practice, specimens thinner than 10 nm and composed of low atomic number elements such as a hydrogen, carbon, oxygen and nitrogen behave as weak phase objects.

2.3.4 The Contrast Transfer Function

Hanzen and coworkers [26] developed the concept of the Contrast Transfer Function (CTF) for electron microscopy. This enabled the description of an objective lens independent of any particular specimen structure.

In (2.3), consider an idealized point specimen that scatters light isotropically, so that it is a source of spherical waves of amplitude $f(\theta)$, independent of the scattering angle θ. By definition, the point spread function is obtained as the image of this specimen. Introducing polar coordinates r' and ϕ in the image plane and setting magnification to 1, the scalar product becomes $\mathbf{q}\cdot\mathbf{r} = qr'\cos\phi = \theta r'\cos\phi/\lambda$; we have $\mathbf{d^2q} = \theta d\theta/\lambda^2$ and $F(q) = \lambda f(\theta)$. We then get

$$\psi_m(\mathbf{r}') = \frac{1}{0} + \frac{i}{\lambda}\int_0^{\alpha_0}\int_0^{2\pi} f(\theta)e^{-iW(\theta)}e^{\frac{2\pi i}{\lambda}\theta r'\cos\phi}\theta d\theta \tag{2.17}$$

where we use 1 for brightfield mode and 0 for dark field mode. The factor i indicates a phase shift of $\pi/2$ between primary and scattered waves. The difference between bright and dark field modes is that in the former, the primary incident wave (normalized to 1) contributes to the image amplitude, whereas in the dark field mode it

is absorbed by a central beam stop or a diaphragm. The factor i indicates a phase shift of 90° between incident and scattered waves.

Applying the weak amplitude weak phase approximation to this point specimen, using (2.16) for a single spatial frequency q, we can represent the point object's local amplitude modulation and phase shift by $\epsilon_s(\mathbf{r}) = \epsilon_s(2\pi qx)$ and $\varphi_s(\mathbf{r}) = \varphi_q(2\pi qx)$ giving

$$\psi_s(x) = 1 - \epsilon_q \cos(2\pi qx) + i\varphi_q \cos(2\pi qx) + \dots \tag{2.18}$$

Using (2.17), the image intensity becomes

$$I(x') = |\psi_m(x')|^2 \tag{2.19}$$

$$I(x') = 1 - D(q)\epsilon_q \cos(2\pi qx') - B(q)\varphi_q \cos(2\pi qx') \tag{2.20}$$

The CTF is defined as the Fourier transform of the point spread function. Hence, $D(q) = 2\cos W(q)$ is the CTF of the amplitude structure of the specimen and, using (2.12),

$$B(q) = -2\sin W(q) = -2\sin\left[\frac{\pi}{2}(C_s\lambda^3 q^4 - 2\Delta z\lambda q^2)\right] \tag{2.21}$$

is the CTF of the phase structure.The sign of $B(q)$ is chosen so that $B(q) > 0$ for postive contrast. Using (2.14) the phase CTF is given by

$$B(q) = 2\sin\left(\frac{\pi}{2}\left[C_s q^4\lambda^3 - \lambda q^2(2\Delta f + \Delta f_{diff}\cos(2\phi - 2\phi_a))\right]\right) \tag{2.22}$$

Tani et al [77] use a CTF formula that accounts for both phase and amplitude contrast. To derive this form, consider (2.20). Setting $\Delta\phi = \cos^{-1}(\frac{\varphi_q}{\sqrt{\varphi_q^2+\epsilon_q^2}})$ we can

express the intensity as

$$I(x') = 1 + 2\cos(2\pi q x')\sin(W(q) - \Delta\phi) \tag{2.23}$$

Hence the CTF is expressed as

$$CTF(q,\phi) = \sin(\frac{\pi}{2}\left[C_s q^4 \lambda^3 - \lambda q^2(2\Delta f + \Delta f_{diff}\cos(2\phi - 2\phi_a))\right] - \Delta\phi) \tag{2.24}$$

2.3.5 EM Imaging Equation

Using the theory of contrast transfer, the ideal image formation process can be described by

$$I(q,\phi) = CTF(q,\phi)O(q,\phi) \tag{2.25}$$

where $I(q,\phi)$ is the Fourier transform of the image and $O(q,\phi)$ is the Fourier transform of the object.

In this chapter, we have assumed ideal imaging conditions. Noise from sources such photo-detection and photon-counting have not been considered. In the case of EM, we have not included the background signal due to inelastic scatter and the envelope function due to incoherence of the electron beam, stage drift etc [73],[52]. In the subsequent chapters, these issues will be taken into account.

CHAPTER III

Principles and approaches for the deconvolution problem

For incoherent imaging modalities such as optical and fluorescence microscopy and biological electron microscopy, the image formation process can be modeled as a convolution of the object signal with a transfer function. As a result, the image is a distorted version of the object itself, which ultimately limits the resolution available from the imaging instrument. **Deconvolution** aims to correct the image for distortions due to the transfer function, system noise and other non-idealities of the imaging process, thereby improving the imaging resolution.

In this chapter, we briefly study the general image formation process. Next, we briefly describe some of the common deconvolution algorithms that have been developed from linear system theory, and also from a statistical perspective. Finally, we study the Automatic Image Deconvolution Algorithm (AIDA) that forms the basis of Chapter VIII.

3.1 Basic Equation

We assume throughout that the object is spatially bandlimited so that the problem can be spatially sampled. Then in many 2-D imaging applications the image formation process can be modeled as [44, 72]

$$y(n_1, n_2) = h(n_1, n_2) \otimes o(n_1, n_2) + n(n_1, n_2) \tag{3.1}$$

where

(n_1, n_2)	are the discrete pixel coordinates of the image frame;
$y(n_1, n_2)$	is the blurred image (output from device or process);
$o(n_1, n_2)$	is the true image;
$h(n_1, n_2)$	is the transfer function (TF)
	also known as Point Spread Function (PSF)
$n(n_1, n_2)$	is additive noise, and;
$\otimes$	is the discrete 2-D linear convolution operator.

Taking the 2-D DSFT (Discrete Space Fourier Transform) yields

$$Y(\omega_1, \omega_2) = O(\omega_1, \omega_2)H(\omega_1, \omega_2) + N(\omega_1, \omega_2) \tag{3.2}$$

The resulting image y is not an accurate visualization of the object o, since it is a filtered version of o that has been distorted by noise. Deconvolution algorithms attempt to correct the image for the effects of the transfer function, thereby providing an image that better represents the object.

In the Fourier domain, we want to determine $O(\omega_1, \omega_2)$ knowing $Y(\omega_1, \omega_2)$ and $H(\omega_1, \omega_2)$. A naive approach would be a simple division of image Y by the transfer function H, i.e.

$$\hat{O}(\omega_1, \omega_2) = \frac{Y(\omega_1, \omega_2)}{H(\omega_1, \omega_2)} = O(\omega_1, \omega_2) + \frac{N(\omega_1, \omega_2)}{H(\omega_1, \omega_2)} \tag{3.3}$$

This method, called the *Fourier quotient method* [41] or *inverse filtering* [55] gives very poor and unstable results, since the inverse filter $\frac{1}{H}$ is large at frequencies for which H is very small (typically, high frequencies). This results in large noise amplification, and thus a poor reconstruction. As a result, Fourier approaches adopt some strategy to reduce noise amplification.

A variety of deconvolution algorithms have been developed, reflecting the different ways of obtaining the best estimate of the true object. If one has good prior knowledge of the PSF (which is often the case in microscopy), then simple modeling of PSF with a set of variable parameters is used [41]. In many cases, only partial information of the PSF is available, in which case myopic deconvolution methods are used. Finally, in some cases, no information of the PSF may be available, in which case blind deconvolution methods are used.

3.1.1 The Partial Data Problem

In applications such as remote sensing or microscopy, the unknown image often does not have compact support (there is no compact region outside of which the image is known to be zero). Rather, it is just part of a bigger image. In this case, the blurred image that constitutes the data is actually smaller than the image to be reconstructed. This is called the partial data problem [28]. The difficulty of this problem is that it can be formulated as an under-determined system of linear equations. We shall show in the coming sections how one of our algorithms is able to overcome this issue.

3.1.2 The Case For Blind Deconvolution

Deconvolution is an ill-posed problem. This means that small errors in image or PSF information will lead to large errors in object estimates. This problem has traditionally motivated statistical deconvolution methods in which some or all available system information is incorporated in the algorithm in order to make the algorithm more robust. Unfortunately, regardless of the application,obtaining an accurate PSF is difficult [55, 41]. Even if a theoretical PSF model is used, it cannot account for model imperfections. Moreover, in applications such as microscopy, obtaining the

PSF is often time consuming and difficult [55].

Blind deconvolution algorithms seek to estimate not only the original image but also the PSF. In doing so, these methods hold promise for accurate determination of the object. Until now, blind deconvolution algorithms were not very popular, as the difficulty of the problem made computation times very high and often impractical. However, as we shall show in Chapters IV, V and VI, in some cases, a linear algebraic approach to this problem can give us excellent images, often better than non-blind statistical methods.

3.1.3 A Brief Overview of Common Deconvolution Algorithms

Deconvolution algorithms generally fall under two categories: linear algorithms that have been developed with a deterministic approach; and statistical algorithms that use a probabalistic approach.

3.1.4 Linear Methods

Linear methods aim to find the optimal object estimate that minimize the noise term in (3.1) using either a least squares or total least squares approach [35],[36],[47],[63]. Stated mathematically, we find $\hat{o}(n_1, n_2)$ such that

$$\hat{o}(n_1, n_2) = \underset{o(n_1,n_2)}{\operatorname{argmin}} \|n(n_1, n_2)\|^2 = \underset{o(n_1,n_2)}{\operatorname{argmin}} \|y(n_1, n_2) - o(n_1, n_2) \otimes h(n_1, n_2)\|^2 \tag{3.4}$$

A direct minimization of equation (3.4) will produce unstable results due to the ill-posed and ill-conditioned nature of the problem. The results can be made more stable by using Tikhonov regularization. The regularized solution is expressed as

(3.5)

$$\hat{o}(n_1, n_2) = \underset{o(n_1,n_2)}{\operatorname{argmin}} \|y(n_1, n_2) - o(n_1, n_2) \otimes h(n_1, n_2)\|^2 + \lambda \|f(n_1, n_2) \otimes o(n_1, n_2)\|^2$$

where $f(n_1, n_2)$ is a penalty function applied to the data. This error criterion contains two terms, the first representing the fidelity to the data, and the second representing

avoiding roughness in the restored image [41]. λ is the regularization parameter and represents the trade off between data fidelity (variance) and image fidelity (bias). Finding λ requires numerical techniques such as generalized cross validation [43]; there is vast literature on this topic which we will not review here. The solution to (3.5) is easily expressed in the frequency domain as

$$O(\omega_1, \omega_2) = \frac{H^*(\omega_1, \omega_2) Y(\omega_1, \omega_2)}{|H(\omega_1, \omega_2)|^2 + \lambda |F(\omega_1, \omega_2)|^2} \tag{3.6}$$

Generalizing this, we get the filtering [3] solution

$$O(\omega_1, \omega_2) = \frac{W(\omega_1, \omega_2) Y(\omega_1, \omega_2)}{H(\omega_1, \omega_2)}. \tag{3.7}$$

$W(\omega_1, \omega_2)$ is typically a Gaussian, Hanning, Hamming or Blackman window [61].

Linear regularized methods are very attractive from a computational point of view but also suffer from some drawbacks:

- The Wiener and Tikhonov restoration filters are both convolution filters. Their linear nature makes them incapable of restoring frequencies for which the PSF has zero response. In particular, the PSF of a 3-D widefield fluorescence microscope has large regions in the frequency domain with zero response known as the missing cone. These cannot be restored and leads to Gibbs oscillations.
- It is difficult to incorporate a priori information.

One can improve on least squares by using constrained least squares methods [35, 47], which typically enforce non-negativity in the solution. The solution is no longer obtained in a one-pass process, but instead it is obtained iteratively. A commonly used method is the Tikhonov-Miller method, which uses conjugate gradients to solve the problem. The Tikhonov-Miller method provides a theoretical bound on the error in the reconstructed image[9]. The interested reader is referred to [81].

3.1.5 Statistical Methods

Statistical methods treat the deconvolution problem as one of estimating an unknown object $o(n_1, n_2)$ from noisy measurements $y(n_1, n_2)$. This approach allows us to use well known methods from estimation theory. While there are several different statistical methods to solve this problem, the three approaches that are most commonly used are: maximum-likelihood (ML) estimation; Bayesian estimation; and penalized likelihood estimation. Each of these is briefly discussed in the coming sections. The interested reader is referred to [17, 29, 74, 68] for more details.

Maximum Likelihood Methods

Maximum likelihood (ML) methods aim to maximize the "agreement" between the measurement (the image y) and the object o. Mathematically,

$$\hat{o} = \underset{o}{\operatorname{argmax}} \ \log p(y|o) \tag{3.8}$$

For additive zero-mean white Gaussian noise, ML methods are identical to the deterministic methods discussed above, with no penalty functions. As a result, ML methods often result in noisy solutions [17].

Bayesian Methods

Bayesian estimators provide a framework to incorporate information about the object, thereby constraining the solution. This leads to more stable estimates in the presence of noise. The object information is incorporated as a "prior", denoted here by $p(o)$.

Bayesian estimation is most commonly used with the Maximum A Posteriori (MAP) approach, where the solution is defined as

$$\hat{o} = \underset{o}{\operatorname{argmax}} \ p(o|y). \tag{3.9}$$

We need Bayes rule, which is

$$p(o|y) = \frac{p(y|o)p(o)}{p(y)} \tag{3.10}$$

Applying the logarithm to both sides and ignoring $p(y)$ as it is independent of o gives,

$$o_{MAP} = \underset{o}{\text{argmax}} \ [\log p(y|o) + \log p(o)] \tag{3.11}$$

If both the noise and the object are modelled by white Gaussian random fields, MAP methods are identical to the deterministic methods discussed above, where $\log p(o)$ plays the role of the penalty function. If the variance of $p(o)$ is infinite, then MAP reduces to ML.

A major drawback of Bayesian estimation is that it is difficult to design priors that represent the true object accurately. This problem is overcome in the penalized likelihood approach discussed next [17].

Penalized likelihood approach

The MAP estimator attempts to maximize two terms. The first term quantifies the agreement of the distorted object with the measurement. The second term quantifies the agreement with the prior expectation about the object. In contrast, the penalized likelihood method attempts to minimize two terms; the first term quantifies the disagreement of the distorted object and the measurement, and the second term quantifies the disagreement of the estimate with the expected *properties* of the object. Mathematically,

$$o_{PL} = \left[\underset{o}{\text{argmin}} \ -\log p(y|o) + \lambda R(o)\right] \tag{3.12}$$

Since the term $\log p(y|o)$ measures the fidelity of the estimate to the observed data, it is known as the *data fidelity term*.

The term $\lambda R(o)$ is the penalty function that regularizes the estimate. The term λ is known as the regularizing parameter [17] or hyperparameter [59].

While (3.11) and (3.12) look similar, they are philosophically very different. The "prior" term in Bayesian estimation is a function of the object itself; it does not vary with the measurement. In the penalized likelihood approach, we are only concerned about the deviation of the estimate from a certain property of the object, allowing us to change the penalty term depending on the measurement. With the penalized likelihood approach, it is simpler to design and implement penalities incorporating a priori object information than it is to do the same with statistical priors in the MAP approach.

3.2 The Automatic Image Deconvolution Algorithm

The Automatic Image Deconvolution Algorithm (AIDA) is a myopic deconvolution algorithm devloped by Hom et al. [31]. The algorithm is based on the Myopic Iterative STep preserving Restoration ALgorithm (MISTRAL) that was developed for astronomy using a penalized likelihood approach [59]. Although the theoretical development for both algorithms is very similar, AIDA different from MISTRAL in a key way: the hyperparameter is estimated automatically in AIDA, while it has to be determined by trial and error in MISTRAL. This makes AIDA automatic, easy to use, and faster than MISTRAL.

In the rest of this section, we discuss the theory behind the AIDA algorithm. We first discuss the choice of the noise model, data fidelity term, and penalizing function. Next, we discuss the myopic scheme which allows for the joint estimation of the transfer function and the object when the transfer function is not known very well. Finally, we study the hyperparameter estimation scheme which enables AIDA

to be fully automatic.

3.2.1 AIDA Noise Model

In a typical digital imaging setup, we can make the following assumptions: (i) The image formation process is linear and space invariant; (ii) signal-dependent Gaussian and Poisson noise sources are present [70]; and (iii) the response of each CCD pixel is independent of the others. This allows us to write the imaging equation as

$$y(n_1, n_2) = o(n_1, n_2) \otimes h(n_1, n_2) \circ n_p(n_1, n_2) + n_G(n_1, n_2) \tag{3.13}$$

where $n_p(n_1, n_2)$ is a Poisson process with variance σ_P^2 and $n_G(n_1, n_2)$ represents a zero-mean Gaussian random field with variance σ_G^2. When images are not photon limited, a good approximation to the above noise model is[59, 31].

$$w(n_1, n_2) \sim N(o, \sigma_w^2(n_1, n_2)) \tag{3.14}$$

where

$$\sigma_w^2(n_1, n_2) = \sigma_G^2 + \sigma_P^2(n_1, n_2) \tag{3.15}$$

The variance σ_G^2 and the variance map σ_P^2 can be estimated from the image. Assuming the image is background subtracted, one can estimate σ_G^2 by fitting the histogram of negative-valued pixels with the left half of a zero centered Gaussian.

$$\sigma_G^2 = \frac{\pi}{2} \left[< y(n_1, n_2) >_{((n_1,n_2);y(n_1,n_2)\leq 0)} \right]^2 \tag{3.16}$$

If the image does not have any negative pixels, as is often the case in microscopy, a separate dark image is required to estimate σ_G^2. The Poisson contribution (variance map) can be calculated as [31]

$$\sigma_P^2(n_1, n_2) = max\left[y(n_1, n_2), 0\right] \tag{3.17}$$

This estimate is quite accurate for bright areas where the photon noise contribution is much greater than the Gaussian noise. In dark regions this estimate is unimportant, as the Gaussian noise dominates over the Poisson noise contribution.

3.2.2 Data Fidelity Term

We use a weighted maximum likelihood term to describe data fidelity:

$$J_n(y|o) = \frac{1}{2} \sum_{n_1,n_2} \frac{[y(n_1,n_2) - o(n_1,n_2) \otimes h(n_1,n_2)]^2}{w(n_1,n_2)} \tag{3.18}$$

where

$$w(n_1,n_2) = \sigma_G^2 + \sigma_P^2(n_1,n_2) \tag{3.19}$$

$w(n_1,n_2)$ acts as a weighting term. When w is large for a given (n_1,n_2), the data at that point is considered less "reliable", and its contribution to the cost function $J_n(y|o)$ is smaller.

3.2.3 Regularization Term

Most objects in microscopy are smooth or piecewise-smooth. (3.18) may be quadratically regularized using a Gaussian prior. However, quadratic regularization tends to oversmooth the image at the edges, as the Gaussian prior model is not particularly well-suited to real world images [17].

AIDA solves this problem by using the edge-preserving regularizer proposed by Brette and Idier [7, 31]. This regularizer is similar to the Huber functional in that it is quadratic for small gradients and linear for large ones [17]. The quadratic part ensures a good smoothing of the small gradients (often caused by noise), while the linear portion prevents over-penalization of the large gradients to preserve the edges (unlike quadratic regularization). The edge-preserving term is mathematically

described as [31]

$$J_o(o) = \lambda_o \sum_{n_1,n_2} \phi(\gamma(o, \theta_{n_1,n_2})) \tag{3.20}$$

$$\phi(\gamma) = \gamma - \ln(1+\gamma) \tag{3.21}$$

$$\gamma(o, \theta_{n_1,n_2}) = \frac{\|\nabla o(n_1, n_2)\|}{\theta_{n_1,n_2}} \tag{3.22}$$

where $||\nabla o(n_1, n_2)|| = [(\nabla_x o(n_1, n_2))^2 + (\nabla_y o(n_1, n_2))^2]^{\frac{1}{2}}$ and $\nabla_x o(n_1, n_2)$ and $\nabla_y o(n_1, n_2)$ are the object gradients along x and y respectively. The terms θ_{n_1,n_2} and λ_o are known as the "hyperparameters" of the object prior [59].

The term $\phi(\gamma)$ characterizes the local texture of the object. It is called the clique potential. When γ is small, (3.21) approximates to $\phi(\gamma) = \gamma - (\gamma - \gamma^2/2 + \ldots) \approx \gamma^2/2$; for large γ , $\phi(\gamma) = \gamma$.

The hyperparameter terms λ_o and θ_{n_1,n_2} control the amount of regularization. λ_o controls the tradeoff between data fidelity and the edge preservation, while θ_{n_1,n_2} determines when the regularization transitions from being quadratic to being linear.

3.2.4 Myopic Deconvolution

Until now we have assumed that the transfer function is known accurately and the only unknown is the object. In many realistic cases, this is untrue. When the transfer function is poorly known or not known at all, the problem becomes ill-conditioned and ill-posed for the following two reasons: (1) The transfer function is bandlimited by the imaging system; and (2) Noise is present beyond the bandwidth of the system.

Several approaches have been attempted to solve this problem. They generally fall into two categories. In the first, deconvolution is attempted with the assumption that the transfer function is unknown [29, 89]. This is known as blind deconvolution. However, apart from a few specialized cases, blind deconvolution algorithms are not very effective. Constraints such as positivity [44] of the object and transfer function

do aid in deconvolution, but even this scheme is not very effective for large PSFs.

The other class of approaches fall into the Myopic deconvolution category. Here, the transfer function is known but is poorly characterized. AIDA and MISTRAL use this approach where the principle is to constrain the transfer function softly at all frequencies and then jointly estimate the transfer function and object in a MAP framework. We modify (3.10) for the joint estimation as :

$$p(o,h|y) = \frac{p(y|o,h)p(o)p(h)}{p(y)} \tag{3.23}$$

The joint estimates can be written as

$$[\hat{o},\hat{h}] = \underset{o,h}{\operatorname{argmin}} \; -\log p(y|o,h) - \log p(o) - \log p(h) \tag{3.24}$$

The only new term in this scheme is the last one, which accounts for the partial knowledge of the transfer function. We use the following Fourier domain constraint

$$J_h(h) = \frac{\lambda_H}{2} \sum_{\omega_1,\omega_2} \frac{|\hat{H}(\omega_x,\omega_y) - \overline{H}(\omega_x,\omega_y)|^2}{v(\omega_x,\omega_y)} \tag{3.25}$$

where λ_H controls the transfer function regularization relative to the data-fidelity term of (3.12), $\hat{H}(\omega_x,\omega_y)$ is the Fourier transform transfer function estimate, $\bar{H}(\omega_x,\omega_y)$ is the Fourier transform of the averaged PSF. $v(\omega_x,\omega_y)$ is the sampling variance or the power spectral density of the transfer function, and is defined as

$$v(\omega_x,\omega_y) = <| \, H(\omega_w,\omega_y) - \overline{H}(\omega_w,\omega_y) \, |>^2 = <| \, H(\omega_w,\omega_y) \, |>^2 - | \, \overline{H}(\omega_x,\omega_y) \, |^2 \tag{3.26}$$

$v(\omega_x,\omega_y)$ serves as a spring constant that constrains each frequency component of the transfer function to a mean value dervied from a set of transfer functions. Conan et al. [12, 20] have shown that this constraint (also known as a harmonic Optical Transfer Function (OTF) constraint [31]) performs much better in recovering the true PSF than simple bandlimiting of the PSF.

3.2.5 Automatic Hyperparameter Estimation

The MISTRAL algorithm requires a manual selection of the hyperparameters $\theta_{n_1,n_2}, \lambda_o$ for effective regularization. To deconvolve an image optimally, one has to deconvolve the image for a variety of $\theta_{n_1,n_2}, \lambda_o$ sets from which "acceptable" reconstruction $\theta_{n_1,n_2}, \lambda_o$ sets are found. Usually, a plane of such acceptable solutions are found, suggesting that when one hyperparameter is optimally defined the other hyperparameter can be adjusted for optimally balancing the data-fidelity and edge preserving terms [31].

Hom et al. [31] developed an automatic parameter estimation scheme based on the assumption that the probability distribution of the pixels in an image can be interpreted as a Gibbs distribution. If $J(x)$ is the cost function and $Z(x) = \int_x exp\left[-J(x)\right] dx$ is the partition function, then the probability distribution of the pixels is modelled as being given by [5, 22]

$$p(x) = exp\left[-J(x)\right]/Z(x) \tag{3.27}$$

With this assumption, we can define an image as optimally regularized when the Gibbs free energy distribution of all the pixels of the data fidelity term $-\log p(y|o,h)$, equals that of the edge-preserving object term $-\log p(o)$. Defining $\delta \equiv i - o \otimes h$ and $\zeta(n_1,n_2)$ as the combined Gibbs free distribution of all the pixels, we define

$$\zeta_n(n_1,n_2)_\delta \equiv \int_\delta exp\left[-(\delta_{n_1,n_2})^2/2w(n_1,n_2)\right] d\delta \tag{3.28}$$

(3.29)

$$\zeta_o(n_1,n_2)_{\|\nabla o(n_1,n_2)\|} \equiv$$
$$\int_{\|\nabla o(n_1,n_2)\|} exp\left[-\lambda_o\left(\frac{\|\nabla o(n_1,n_2)\|}{\theta(n_1,n_2)} - \ln\left(1+\frac{\|\nabla o(n_1,n_2)\|}{\theta(n_1,n_2)}\right)\right)\right] d\|\nabla o(n_1,n_2)\|$$

Equating these integrals, we get

$$\zeta_n(n_1, n_2)_\delta = \zeta_o(n_1, n_2)_{\|\nabla o(n_1,n_2)\|} \tag{3.30}$$

$$\sqrt{2\pi w(n_1, n_2)} = \theta_{n_1,n_2} e^\lambda \int_1^\infty e^{-\lambda t}/t^{-\lambda} dt \tag{3.31}$$

$$= \theta_{n_1,n_2} \left(\frac{1}{\lambda_o} + 1 \right) \tag{3.32}$$

where the approximation holds for $\lambda_o \leq 10$. By equating these integrals on an element-by-element basis, we are intrinsically assuming that the Gibbs distribution of (3.27) can be represented as a product of sepearable functions. That is, we are assuming that the pixels are independent and identically distributed (i.i.d.). This is also known as the mean-field approximation. Solving for λ_o in (3.31) gives

$$\lambda_o = (\sqrt{2\pi w(n_1, n_2)}/\theta_{n_1,n_2} - 1)^{-1} \tag{3.33}$$

We can now set

$$\theta_{n_1,n_2} = \sqrt{w(n_1, n_2)/\sigma_G} \tag{3.34}$$

Substituting θ_{n_1,n_2} in (3.33), we get a pixel-independent expression for λ_o.

$$\lambda_o = (\sqrt{2\pi\sigma_G} - 1)^{-1} \tag{3.35}$$

This scheme was found to give good object estimates [31]. In cases where this scheme over-regularized due to model mismatch, scaling the hyperparameter up or down by no more than a factor of 10 was found to be sufficient.

The λ_H parameter from (3.25) also needs to be balanced. By the power conservation relation of Parseval's theorem we know $\sum_{r=0}^{N-1} |x(r)|^2 = (1/N_d) \sum_{k=0}^{N-1} |X(k)|^2$.

The λ_H term operates on a reciprocal space term. Hence, to heuristically balance λ_H with respect to the other terms, we set

$$\lambda_H = 1/N_d \tag{3.36}$$

N_d being the number of pixels in the image.

CHAPTER IV

2-D blind deconvolution of even point-spread functions from compact support images

4.1 Introduction

4.1.1 Blind Deconvolution

The problem of reconstructing a 2-D image with compact support from its 2-D convolution with an unknown blurring or point-spread function (PSF) arises in several disciplines [44], including image restoration from an unknown blurring agent, remote sensing through the atmosphere, and medical imaging. A good introductory review of the history and applications of this problem is available[44].

In many applications in optics, acoustics and electro-magnetics, the point-spread function may be assumed to be an even function of its spatial variables, due to reciprocity. To see this, let $u(x_o)$ be the electromagnetic or acoustic field strength at spatial position x_o. The response $u(y_o)$ to an excitation or source $s(x_o)$ is $u(y_o) = \int G(y_o, x_o)s(x_o)dx_o$, where $G(y_o, x_o)$ is the Green's function. If the Green's function is translation-invariant, then $G(y_o, x_o) = G(y_o - x_o)$. If reciprocity holds, then by definition $G(y_o, x_o) = G(x_o, y_o)$, and $G(\cdot)$ is an even function.

Since both the image and the point-spread function can be assumed to have finite spatial extent (i.e., finite support), their Fourier transforms may be sampled in wavenumber. Most images are approximately bandlimited to the extent that they

may also be sampled spatially as well. This leads to the discrete version of this problem, in which a discrete-time image known to have finite spatial extent is to be reconstructed from its convolution with an also-unknown point-spread function (PSF). This precludes methods based on oversampling of continuous images.

4.1.2 Previous Work

A common approach for blind deconvolution problems is to use an iterative transform algorithm [44], which alternate between the spatial and wavenumber domains. However, these algorithms often stagnate, failing to converge to a solution[18, 83]. Other approaches require the computationally expensive and extremely unstable numerical operation of tracking zero sheets of algebraic functions, or statistical estimation algorithms that also may not converge. Another iterative approach (NAS-RIF) is guaranteed to converge, but assumes the PSF has an inverse PSF of small size. We will not attempt to list all approaches here.

The problem addressed in this paper should be distinguished from the problem of multichannel blind deconvolution, addressed in many recent papers. In the latter problem, a single unknown signal or image is filtered with several unknown blurring functions, resulting in several known outputs. This is conceptually a much simpler problem than single-blur blind deconvolution.

4.1.3 Problem Formulation

The 2-D discrete blind deconvolution problem is as follows [44]. We observe

$$y(i_1, i_2) = h(i_1, i_2) * *u(i_1, i_2) + n(i_1, i_2) \tag{4.1}$$

where $**$ denotes convolutions in i_1 and i_2. The 1-D convolution $*$ is defined here as

$$h(n) * u(n) = \sum_{i=0}^{n} h(n-i)u(i) = \sum_{i=0}^{n} h(i)u(n-i) \tag{4.2}$$

We make the following assumptions (N=L+M-1):

1. Image $u(i_1, i_2) \neq 0$ only for $0 \leq i_1, i_2 \leq M - 1$;
2. PSF $h(i_1, i_2) \neq 0$ only for $0 \leq i_1, i_2 \leq L - 1$;
3. Data $y(i_1, i_2) \neq 0$ only for $0 \leq i_1, i_2 \leq N - 1$;
4. PSF $h(i_1, i_2) = h(L - i_1, L - i_2)$ (even PSF);
5. $n(i_1, i_2)$ is a zero-mean white Gaussian noise field;
6. All variables are real.

Given knowledge of only the data $y(i_1, i_2)$, the goal is to reconstruct the image $u(i_1, i_2)$ and PSF $h(i_1, i_2)$; hence the term "blind deconvolution." No stochastic assumptions are made about either the image or the point-spread function. This precludes use of methods based on cumulants, ARMA or Poisson image models or stochastic equalization. Neither the image nor the PSF need be nonzero for all i_1, i_2 in the above ranges; the support constraints need only prevent translational ambiguity.

This formulation is necessary in order to have a well-posed inverse problem, for which there is almost surely only one solution (to the ambiguities listed below). However, we also demonstrate that our method works fairly well in the partial data case where the blurred image is cropped to the same size as the original image, and the missing data are windowed to zero. This seems to be the case when the PSF has long and small tails, so that the missing data are close to zero anyways. We also note that the actual size of the PSF need not be known, since the PSF itself is not recovered as part of our procedure.

4.1.4 Problem Ambiguities

There are three trivial ambiguities to the 2-D blind deconvolution problem:

1. *Scale factor:* If $\{h(i_1, i_2), u(i_1, i_2)\}$ are a solution, then $\{ch(i_1, i_2), \frac{1}{c}u(i_1, i_2)\}$ is also a solution for any real constant c. If c cannot be determined from the image energy, it usually is irrelevant. We consider the problem to be solved when the image is determined to a scale factor;

2. *Translation:* If $\{h(i_1, i_2), u(i_1, i_2)\}$ are a solution, then $\{h(i_1 + d_1, i_2 + d_2), u(i_1 - d_1, i_2 - d_2)\}$ is also a solution for any constants d_1, d_2. We eliminate this ambiguity by specifying the supports, as below (1);

3. *Exchange:* We need to be able to distinguish $h(i_1, i_2)$ from $u(i_1, i_2)$. Since $h(i_1, i_2)$ is an even function by assumption, this requires that the image not *also* be an even function, or that $L \neq M$.

We assume that the 2-D z-transforms

$$H(x, y) = \sum_{i_1=0}^{L-1} \sum_{i_2=0}^{L-1} h(i_1, i_2) x^{i_1} y^{i_2} \tag{4.3a}$$

$$U(x, y) = \sum_{i_1=0}^{M-1} \sum_{i_2=0}^{M-1} u(i_1, i_2) x^{i_1} y^{i_2} \tag{4.3b}$$

are irreducible (they cannot be factored). This is almost surely true [34]. One way to see this quickly is to note that in the noiseless case, (4.1) is $N^2 = (L + M - 1)^2$ simultaneous quadratic equations in $L^2 + M^2$ unknowns. Since the problem is overdetermined, by Bezout's theorem [34] there is almost surely no more than one solution. In fact, there are generically *no* solutions; only from (4.1) do we know that there is a perturbation of the data for which a solution exists[34].

4.2 1-D Blind Deconvolution

4.2.1 Formulation

We quickly review noiseless 1-D blind deconvolution, *for later use below.* We observe, under assumptions analogous to those listed above,

$$y(n) = h(n) * u(n), h(n) = h(-n). \tag{4.4}$$

Taking z-transforms gives

$$Y(z) = H(z)U(z) = z^L H(1/z)U(z). \tag{4.5}$$

The zeros of $H(z)$ occur in conjugate reciprocal quadruples Q_i, where

$$Q_i = \{z_i, z_i^*, 1/z_i, 1/z_i^*\} \tag{4.6}$$

$$|z_i| = 1 \rightarrow z_i^* = \frac{1}{z_i}, \quad z_i = \frac{1}{z_i^*} \tag{4.7}$$

So one way to solve the 1-D problem is to look for Q_i among the zeros of $Y(z)$. Provided $U(z)$ has no Q_i among its zeros, there is no ambiguity.

This is impractical, but does show that even the 1-D problem almost surely has a unique solution, to the trivial ambiguities noted above. We require only that $U(z)$ have no Q_i; in practice, this means no zeros on the unit circle. While sampled signals often have zeros near the unit circle, they almost never have zeros on the unit circle.

4.2.2 Resultant Solution

A more practical solution is as follows. From (4.5),

$$Y(z)z^M U(\frac{1}{z}) = U(z)H(z)z^M U(\frac{1}{z}) = z^{N+1}Y(\frac{1}{z})U(z) \tag{4.8}$$

Equating coefficients in (4.8) results in

$$(4.9)\quad \begin{bmatrix} y(0) & 0 & 0 & y^*(N-1) & 0 & 0 \\ y(1) & \ddots & 0 & y^*(N-2) & \ddots & 0 \\ \vdots & \ddots & \vdots & \vdots & \ddots & \vdots \\ 0 & \ddots & y(N-2) & 0 & \ddots & y^*(1) \\ 0 & 0 & y(N-1) & 0 & 0 & y^*(0) \end{bmatrix} \times \begin{bmatrix} u(M-1) \\ \vdots \\ u(0) \\ -u(0) \\ \vdots \\ -u(M-1) \end{bmatrix} = \begin{bmatrix} 0 \\ \vdots \\ 0 \\ 0 \\ \vdots \\ 0 \end{bmatrix}$$

The size of the resultant matrix in (4.9) is

$$(N+M-1) \times (2M) = (2M+L-2) \times (2M)$$

so the matrix is overdetermined if $L > 2$. The overdetermination increases with L; this makes sense since larger L means more Q_i among the zeros of $Y(z)$, which means more constraints on the $y(n)$.

4.2.3 Resultant Example

As an example, solve

$$(4.10)\qquad \{24, 57, 33\} = \{h(0), h(0)\} * \{u(0), u(1)\}$$

The resultant system (4.9) is

$$(4.11)\quad \begin{bmatrix} 33 & 0 & 24 & 0 \\ 57 & 33 & 57 & 24 \\ 24 & 57 & 33 & 57 \\ 0 & 24 & 0 & 33 \end{bmatrix} \begin{bmatrix} u(0) \\ u(1) \\ -u(1) \\ -u(0) \end{bmatrix} = \begin{bmatrix} 0 \\ 0 \\ 0 \\ 0 \end{bmatrix}$$

which has the solution

$$(4.12)\qquad [u(0), u(1)] = [8, 11]$$

The solution is only determined to a scale factor, as expected, since the null vector of the resultant matrix is only determined to a scale factor.

4.2.4 Resultant Reformulation

The resultant matrix in (4.11) can be written as

$$\begin{bmatrix} T_1 & JT_2J \\ T_2 & JT_1J \end{bmatrix} \quad T_1 = \begin{bmatrix} 33 & 0 \\ 57 & 33 \end{bmatrix} \quad T_2 = \begin{bmatrix} 24 & 57 \\ 0 & 24 \end{bmatrix} \tag{4.13}$$

where the T_i are Toeplitz matrices and J is an exchange matrix having ones along the main antidiagonal and zeros elsewhere. For (4.11) in particular,

$$J = \begin{bmatrix} 0 & 1 \\ 1 & 0 \end{bmatrix} \tag{4.14}$$

This shows that the null vector of (4.11) has form $[v^T, \pm(Jv)^T]^T$ for some vector v. Hence the null vector of (4.11) will have the form shown.

We can eliminate this redundancy and reduce the system size by half by writing (10) as the Toeplitz-plus-Hankel system

$$(T_1 + J_1T_2)v = 0 \tag{4.15}$$

The null vector of (4.15) can be found using a fast split algorithm[87].

Alternatively, we can recognize that (4.11) has Toeplitz blocks. A system with Toeplitz blocks can be rearranged into a block-Toeplitz system, which can be solved using the multichannel Levinson algorithm [42]. The blocks in the block-Toeplitz system are 2×2, so this has computational complexity only quadruple that of the scalar Levinson algorithm. The Levinson algorithm can be used to find the null vector of a singular matrix, as long as none of the principal submatrices are also singular; the last reflection coefficient is ± 1 in the scalar case, and has eigenvalues on the unit circle in the multichannel case.

4.3 2-D Blind Deconvolution

4.3.1 Resultant Solution

Noiseless 2-D blind deconvolution can be rewritten as (compare to (4.5))

$$Y(x,y) = H(x,y)U(x,y) = (xy)^L H(\frac{1}{x},\frac{1}{y})U(x,y) \tag{4.16}$$

This leads to (compare to (4.8))

$$Y(x,y)(xy)^M U(\frac{1}{x},\frac{1}{y}) = (xy)^N Y(\frac{1}{x},\frac{1}{y})U(x,y). \tag{4.17}$$

Equating coefficients results in a resultant-like matrix which is block Toeplitz with Toeplitz blocks. This is also known as Toeplitz-block-Toeplitz or multilevel Toeplitz structure. If more about the image support is known than confinement to $[0, M-1]^2$, e.g., the irregular border of the nonzero region is known, the structure becomes mosaic Toeplitz.

The matrix is formed by *nesting* the Toeplitz matrices that implement 1-D convolutions. The matrix size is found by squaring the 1-D matrix size:

$$(N+M-1)^2 \times (2M^2) = (2M+L-2)^2 \times (2M^2)$$

(except that the number of unknown image pixels is always just doubled). Again the matrix is overdetermined if $L > 2$. However, overdetermination is much greater than in 1-D.

This formulation has several major advantages:

1. The unknowns are the image pixel values themselves. Hence it is a "direct" method, not a multistage method in which intermediate quantities (such as the PSF $h(i_1, i_2)$) must be computed. Indeed, we never even use the size of the PSF;

2. The data are the observations themselves. This is important for the noisy data problem; perturbations are made directly to data, not some function of it;

3. Deterministic prior knowledge about the image support (an irregular border of the support, some regions known to be zero) can be incorporated *directly* into the reconstruction algorithm: Form the system (4.17) and omit matrix columns multiplied by $u(i_1, i_2)$ values known to be zero;

4. Edge-preserving regularization techniques can be used as follows: Let R be the resultant matrix formed from (4.17). Minimize a functional of the form $u^T Ru + f(u)$ where $f(\cdot)$ is an edge-preserving regularization function such that the functional is a convex function of u. This is a well-established procedure [10].

The precise form of the structure is best illustrated with a simple example.

4.3.2 Resultant Example

The goal is to solve the 2-D blind deconvolution

$$\begin{bmatrix} 3 & 10 & 8 \\ 11 & 28 & 18 \\ 10 & 19 & 7 \end{bmatrix} = \begin{bmatrix} h_0 & h_1 \\ h_1 & h_0 \end{bmatrix} ** \begin{bmatrix} u_0 & u_1 \\ u_2 & u_3 \end{bmatrix} \tag{4.18}$$

The resultant system from equating coefficients of (4.17) is

$$
\begin{bmatrix}
10 & 0 & 0 & 0 & 8 & 0 & 0 & 0 \\
11 & 10 & 0 & 0 & 18 & 8 & 0 & 0 \\
3 & 11 & 0 & 0 & 7 & 18 & 0 & 0 \\
0 & 3 & 0 & 0 & 0 & 7 & 0 & 0 \\
19 & 0 & 10 & 0 & 10 & 0 & 8 & 0 \\
28 & 19 & 11 & 10 & 28 & 10 & 18 & 8 \\
10 & 28 & 3 & 11 & 19 & 28 & 7 & 18 \\
0 & 10 & 0 & 3 & 0 & 19 & 0 & 7 \\
7 & 0 & 19 & 0 & 3 & 0 & 10 & 0 \\
18 & 7 & 28 & 19 & 11 & 3 & 28 & 10 \\
8 & 18 & 10 & 28 & 10 & 11 & 19 & 28 \\
0 & 8 & 0 & 10 & 0 & 10 & 0 & 19 \\
0 & 0 & 7 & 0 & 0 & 0 & 3 & 0 \\
0 & 0 & 18 & 7 & 0 & 0 & 11 & 3 \\
0 & 0 & 8 & 18 & 0 & 0 & 10 & 11 \\
0 & 0 & 0 & 8 & 0 & 0 & 0 & 10
\end{bmatrix}
\begin{bmatrix}
u_1 \\ u_3 \\ u_0 \\ u_2 \\ -u_2 \\ -u_0 \\ -u_3 \\ -u_1
\end{bmatrix}
=
\begin{bmatrix}
0 \\ 0 \\ 0 \\ 0 \\ 0 \\ 0 \\ 0 \\ 0 \\ 0 \\ 0 \\ 0 \\ 0 \\ 0 \\ 0 \\ 0 \\ 0
\end{bmatrix}
\tag{4.19}
$$

This has the solution

$$
\begin{bmatrix}
u_0 & u_1 \\
u_2 & u_3
\end{bmatrix}
=
\begin{bmatrix}
3 & 4 \\
5 & 7
\end{bmatrix}
\tag{4.20}
$$

Again, the solution is only determined to a scale factor.

4.3.3 Fourier Decomposition

The huge size of (4.20) demonstrates a need for a formulation which requires solution of smaller systems of equations. This can be done as follows.

Let $x_k = e^{j2\pi k/M}$ and y_k similarly. Setting $y = y_k$ in (4.17) yields

$$Y(x, y_k)(xy_k)^M U(\frac{1}{x}, \frac{1}{y_k}) = (xy_k)^N Y(\frac{1}{x}, \frac{1}{y_k})U(x, y_k) \tag{4.21}$$

Since $y(i_1, i_2)$ and $u(i_1, i_2)$ are real, by conjugate symmetry we have $U(\frac{1}{x}, \frac{1}{y_k}) = U^*(\frac{1}{x^*}, \frac{1}{y^*}) = U^*(\frac{1}{x^*}, y_k)$ and similarly for $Y(\cdot)$, since $y_k y_k^* = 1$. This allows (4.21) to be rewritten as

$$Y(x, y_k)y_k^M x^M U^*(\frac{1}{x^*}, y_k) = y_k^N x^N Y^*(\frac{1}{x^*}, y_k)U(x, y_k) \tag{4.22}$$

We recognize (4.22) as a decoupled (in k) set of 1-D complex-valued blind deconvolution problems. Each of these can be solved in parallel using any of the methods in Section 4.2 above.

We can also derive this result directly from the 2-D problem statement (4.16). Setting $y = y_k$ in (4.16) yields

$$Y(x, y_k) = H(x, y_k)U(x, y_k) = H^*(\frac{1}{x^*}, y_k)U(x, y_k) \tag{4.23}$$

from which (4.22) can be derived. And of course we may set $x = x_k$ and obtain an equation like (4.22) with x and y interchanged:

$$Y(x_k, y)y^M x_k^M U^*(x_k, \frac{1}{y^*}) = x_k^N y^N Y^*(x_k, \frac{1}{y^*})U(x_k, y) \tag{4.24}$$

Still another way to see this quickly is to note that since $h(i_1, i_2)$ is a real and even function, its 2-D discrete Fourier transform $H(x_i, y_j)$ ($H(x, y)$ sampled on the unit circle) will also be a real and even function. Hence the singly-transformed $\tilde{h}(i_1, y_k)$ will also be real and even. This shows most directly why the decoupled 1-D problems have even PSFs. Of course the FFT may be used to compute quickly $Y(x, y_k)$ from $y(i_1, i_2)$ and also to compute $u(i_1, i_2)$ from $U(x, y_k)$.

4.3.4 Scale Factors

There is still one problem. Each decoupled 1-D problem is only solvable to a scale factor, as noted in Section 2. Hence (4.22) only yields $c_k U(x, y_k)$, where c_k is the unknown scale factor for the k^{th} problem. The c_k must be determined in order to recover $u(i_1, i_2)$.

One way to compute the c_k is to make use of the known finite support of $u(i_1, i_2)$ and solve the linear system of equations

$$\sum_{k=0}^{M} c_k \tilde{u}(i_1, y_k) e^{j\frac{2\pi M}{M+1}k} = u(i_1, M) = 0 \tag{4.25a}$$

$$\tilde{u}(i_1, y_k) = \sum_{i_2=0}^{M} u(i_1, i_2) e^{-j\frac{2\pi}{M+1}i_2 k} \tag{4.25b}$$

where $U(x, y)$ has now been sampled at $y_k = e^{\frac{j2\pi k}{M+1}}$ and $0 \leq i_1 \leq M-1$. This gives M equations in $M+1$ unknowns c_k, but the latter are only determined to an overall scale factor anyways. However, the linear system (4.25a), (4.25b) is dense and unstructured.

A simpler way is to solve (4.22) for $c_k U(x, y_k)$ and (4.24) for $d_k U(x_k, y)$. It is then a simple matter to read off the relative ratios of the c_k from the latter, and the relative ratios of the d_k from the former. There is still an overall scale factor ambiguity, as expected.

4.3.5 Fourier Example

To illustrate this, we apply (4.22) and (4.24) to the 2-D blind deconvolution problem (4.18). Since $M = 2$, we set $y_k = \pm 1$ and $x_k = \pm 1$. Setting $y_k = 1$ produces

the 1-D problem solved in Section 2. Setting $y_k = -1$ gives

$$\begin{bmatrix} -3 & 0 & 2 & 0 \\ 1 & -3 & 1 & 2 \\ 2 & 1 & -3 & 1 \\ 0 & 2 & 0 & -3 \end{bmatrix} \begin{bmatrix} u(0) \\ u(1) \\ u(1) \\ u(0) \end{bmatrix} = \begin{bmatrix} 0 \\ 0 \\ 0 \\ 0 \end{bmatrix} \tag{4.26}$$

which has the solution (to a scale factor)

$$[u(0), u(1)] = [2, 3] \tag{4.27}$$

From (4.12) and (4.27) and using the notation of (4.18),

$$u_0 + u_2 = 8c_1; \quad u_1 + u_3 = 11c_1; \tag{4.28}$$

$$u_0 - u_2 = 2c_2; \quad u_1 - u_3 = 3c_2. \tag{4.29}$$

Proceeding similarly with $x_k = \pm 1$, we obtain

$$u_0 + u_1 = 7d_1; \quad u_2 + u_3 = 12d_1; \tag{4.30}$$

$$u_0 - u_1 = 1d_2; \quad u_2 - u_3 = 2d_2. \tag{4.31}$$

From (4.28) and (4.30) we quickly obtain

$$[u_0, u_1, u_2, u_3] = [3, 4, 5, 7] \tag{4.32}$$

which agrees with the solution (4.20) (to a scale factor).

4.3.6 Computational Savings

The computational savings using the Fourier decomposition method can be quite significant. The direct method requires computing the null vector of a $(2M + L - 2)^2 \times (2M^2)$ matrix. The Fourier decomposition method requires computing the null vector of $M + 1$ $(2M + L - 2) \times (2M)$ matrices and M $(M + 1)$-point (or larger) discrete Fourier transforms.

The number of arithmetic operations required by each of these approaches depends heavily on the method used. For example, the null vector may be found using the split algorithm of [87], the multichannel Levinson algorithm, or the inverse power method. It is clear that savings using the Fourier decomposition method are very large.

4.4 Noisy Data Case

4.4.1 Formulation

We now consider the noisy data problem. The log-likelihood function is (recall the assumption of an additive white Gaussian noise field)

$$\log p_{Y|U}(y|u) = -\frac{N^2}{2}\log(2\pi\sigma^2) - \frac{1}{2\sigma^2}\sum_{i_1=0}^{N-1}\sum_{i_2=0}^{N-1}[y(i_1,i_2) - h(i_1,i_2) * * u(i_1,i_2)]^2. \tag{4.33}$$

Since the problem is overdetermined, the maximum likelihood estimate (MLE) of $u(i_1, i_2)$ is the solution to a 2-D blind deconvolution problem in which the noisy data $y(i_1, i_2)$ has been replaced with $\hat{y}(i_1, i_2)$. $\hat{y}(i_1, i_2)$ has the following two properties:

1. A solution exists to the overdetermined blind deconvolution $\hat{y}(i_1, i_2) = \hat{h}(i_1, i_2) * * \hat{u}(i_1, i_2)$;

2. $\sum_{i_1=0}^{N-1}\sum_{i_2=0}^{N-1}[y(i_1, i_2) - \hat{y}(i_1, i_2)]^2$ is minimized.

That is, we need to find the minimum least-squares norm perturbation of the noisy data $y(i_1, i_2)$ to admissible data $\hat{y}(i_1, i_2)$ for which a solution to the overdetermined 2-D blind deconvolution problem exists. Then $\hat{u}(i_1, i_2)$ is the MLE of $u(i_1, i_2)$.

Another way to say this is that we need to project the noisy data onto the set of admissible data for which the overdetermined problem can be solved.

4.4.2 Resultant Solution

Fortunately, the formulation (4.17) allows a straightforward solution to this problem. Since each column of the resultant matrix R consists of the noisy data $y(i_1, i_2)$ unwrapped by columns and some zeros (e.g., (18)), we have

$$2M^2 \sum_{i_1=0}^{N-1} \sum_{i_2=0}^{N-1} [y(i_1, i_2) - \hat{y}(i_1, i_2)]^2 = ||R - \hat{R}||_F^2 \tag{4.34}$$

where

1. R is the resultant matrix constructed from $y(i_1, i_2)$;
2. $\hat{R}$ is the resultant matrix constructed from $\hat{y}(i_1, i_2)$;
3. $2M^2$ comes from the $2M^2$ columns of R and $\hat{R}$;
4. $||A||_F^2 = \frac{1}{N^2} \sum_{i=1}^{N} \sum_{j=1}^{N} |A_{i,j}|^2$ is the Frobenius or Hilbert-Schmidt matrix norm of A.

Hence the problem has been reformulated as follows: Compute the minimum Frobenius norm perturbation $\hat{R}$ of R such that: (1) $\hat{R}$ keeps the multilevel Toeplitz structure of R; and (2) $\hat{R}$ drops rank.

This is a well-know problem in linear algebra. There are at least two known approaches:

1. Structured total least squares (STLS) [37];
2. Lift-and-project (LAP) [8].

Since these are quite well known we do not review them here. Their relative performance on this problem is examined below.

4.4.3 Sufficiency Considerations

The above procedure computes an estimate of the image $u(i_1, i_2)$ that by construction is $M \times M$. Since the observed blurred image $y(i_1, i_2)$ is $(M+L-1) \times (M+L-1)$, this does not by itself seem to guarantee that the blurred image is obtained from the original image by convolution with an $L \times L$ PSF $h(i_1, i_2)$.

The following argument shows that in fact the PSF $h(i_1, i_2)$ is in fact almost surely constrained to have $L \times L$ support. That is, the procedure recovers not only an estimate of the image, but an $L \times L$ estimate of the PSF, so that it does in fact find the nearest solution to (1).

First, note that setting $y = x^{N+M-1}$ in (4.16) unwraps the 2-D problem into

$$\begin{aligned} &Y(x, x^{(N+M-1)})x^{(N+M)M}U(\frac{1}{x}, (\frac{1}{x})^{(N+M-1)}) = \\ &x^{(N+M)N}Y(\frac{1}{x}, (\frac{1}{x})^{(N+M-1)})U(x, x^{(N+M-1)}) \end{aligned} \tag{4.35}$$

This is known as the Kronecker substitution; it amounts to taking repeated slices of slope $(N + M - 1)$ through the 2-D wavenumber domain. It effectively unwraps the 2-D problem into a huge 1-D problem.

The example (4.18) unwraps to the 1-D problem with bands of zeros

$$\begin{aligned} &\{10, 11, 3, 0, 19, 28, 10, 0, 7, 18, 8\} = \\ &\{h_1, h_0, 0, 0, h_0, h_1\} * \{u_2, u_0, 0, 0, u_3, u_1\} \end{aligned} \tag{4.36}$$

Equating coefficients in (4.17) and (4.35) show that they both implement the same equations. This is useful in setting up the system, as follows:

1. Unwrap $y(i_1, i_2)$ by columns;

2. Insert bands of $(M - 1)$ zeros between each unwrapped column;

3. Form a 1-D resultant matrix with this as its first column, as in Section 4.2;

4. Delete each column of the resulting matrix which is multiplied by a $u(i_1, i_2)$ value known to be zero.

Second, note that while $u(i_1, i_2)$ is guaranteed to have the proper support $0 \leq i_1, i_2 \leq (M-1)$ by construction, $h(i_1, i_2)$ is not. However, the unwrapped h is guaranteed to have only a finite number of nonzero values, provided that the unwrapped u has no Q_i. To see this, suppose h has infinite support. Then h must have poles, and since h is even these poles must form Q_i. Since the unwrapped y has no poles, the poles of h must be cancelled by zeros of u; to cancel all of the poles of h requires that the zeros of u be in Q_i.

Finally, to show that the unwrapped h has zero bands where it should, suppose that the two zeros in the zero band of h in (33) are replaced with variables a and b. Then we have from (33) that

$$\begin{bmatrix} u_0 & u_2 \\ u_1 & u_3 \end{bmatrix} \begin{bmatrix} a \\ b \end{bmatrix} = \begin{bmatrix} 0 \\ 0 \end{bmatrix} \tag{4.37}$$

This forces $a = b = 0$ unless the image pixels u_i are such that the matrix in (4.37) is singular. For a random image, this is almost surely not true. Hence the unwrapped h will almost surely have its required zero bands, provided that the image pixels are random.

4.4.4 Fourier Decomposition

We show that if the above approach is applied to the Fourier decomposition of the 2-D blind deconvolution problem, the result is the maximum likelihood estimator for a problem with fewer constraints.

Consider the problem defined by (4.1), but with the support constraints

1. Image $u(i_1, i_2) \neq 0$ only for $0 \leq i_1 \leq M-1$;

2. PSF $h(i_1, i_2) \neq 0$ only for $0 \leq i_1 \leq L-1$;

3. Data $y(i_1, i_2) \neq 0$ only for $0 \leq i_1, i_2 \leq N-1$.

That is, the image and PSF have support constraints in only one dimension, even though their 2-D convolution is constrained in both dimensions. In the noiseless case this makes no difference; there is only one solution (to a scale factor), so dropping some of the constraints has no effect, as long as the remaining constraints are sufficient to determine a unique solution. In the noisy case, where we are projecting the data onto the set of feasible solutions, fewer constraints means the closest feasible data set is likely to be different from before. Then the reconstructed image will have some energy in the unconstrained region. But for low noise levels, this is unlikely to matter much.

Using the Fourier decomposition (4.23) produces a set of decoupled 1-D blind deconvolution problems in which no support constraints are imposed in the y direction. This is precisely the problem defined above. Hence solving each of the decoupled 1-D noisy blind deconvolution problems separately and then combining them will produce the maximum likelihood estimate for the above problem, since

1. The k^{th} 1-D problem will involve the singly-transformed data $\tilde{y}(i_1, y_k)$, which will be arranged into a resultant matrix. Since the different Fourier components are independent, the perturbations used in one problem have no effect or constraint on those used in another problem;

2. To ensure this, use $y_k = e^{\frac{j2\pi k}{N-1}}$ to obtain N different problems. Since $M < N$, this also provides a constraint when the 1-D problem estimates are recombined into the 2-D problem estimate; this can only help;

3. The total squared perturbation of $y(i_1, i_2)$ is the sum of the magnitude-squared

(a) Elaine (452X452) convolved with (61X61) PSF (b) Deconvolved image of Elaine. MSE$\simeq 10^{-31}$

Figure 4.1: Deconvolution test for noiseless data. Deconvolution of Elaine image

perturbations of the 1-D problems, by Parseval's theorem.

4.5 Noiseless Case

4.5.1 Full Data Case

The first test of any algorithm is its performance on noiseless data. Fig. 4.1(a) shows the (512×512) 2-D convolution of a (452×452) image ("Elaine") with an unknown (except for being even) Gaussian-like (61×61) PSF. Since the complete blurred image is used, we call this the "full data case."

The 2-D blind deconvolution was performed using the Fourier decomposition approach. This required computing the null vectors of 512 (963×904) matrices, each having Toeplitz-block-Toeplitz structure. While not exactly trivial, this is actually a relatively small amount of computation for an image restoration problem.

The resulting reconstruction is shown in Fig. 4.1(b). As expected, the reconstruction is perfect, with mean square error (MSE) of order 10^{-31} (due to roundoff error).

A more dramatic example of blurring is given next. Fig. 4.2(a) shows the (256×256) 2-D convolution of the (220×220) "Mandrill" image with an unknown (except

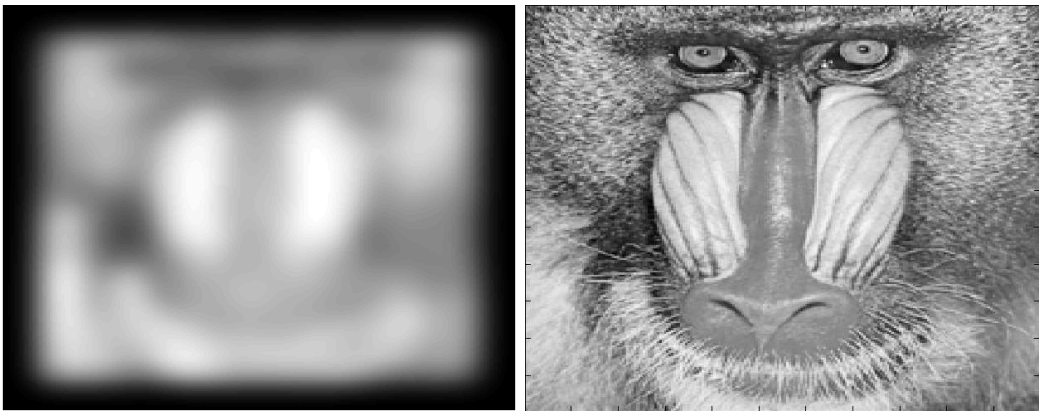

(a) Mandrill (220X220) convolved with a 37X37 PSF (b) Deconvolved image of the mandrill. MSE $\simeq 10^{-31}$

Figure 4.2: Deconvolution test for noiseless data. Deconvolution of Mandrill image

for being even) (37×37) PSF. The blurred image is little more than a blur itself.

Again the Fourier decomposition method was used. This required computing null vectors of 256 (475×440) Toeplitz-block-Toeplitz matrices. The resulting reconstruction is shown in Fig. 4.2(b). Again the reconstruction is perfect, with MSE of order 10^{-31}.

4.5.2 Partial Data Case

What if the complete blurred image is cropped? This might be the case in imaging a portion of a larger scene, as in a remote sensing application.

We have found that if the PSF is rapidly decaying (e.g., a Gaussian PSF), then the edges of the blurred image are very close to zero, and seem to carry little information about the image. Windowing these small border values to zero degrades the results, as expected, but the algorithm still produces a good estimate of the original image. It is important to recall that no prior estimate of the image is used in the algorithm, so this is quite significant.

A typical result is given below. The original 201×201 image shown in Fig.4.3(a) was convolved with the 35×35 Gaussian PSF shown in Fig. 4.3(b). Of course, the

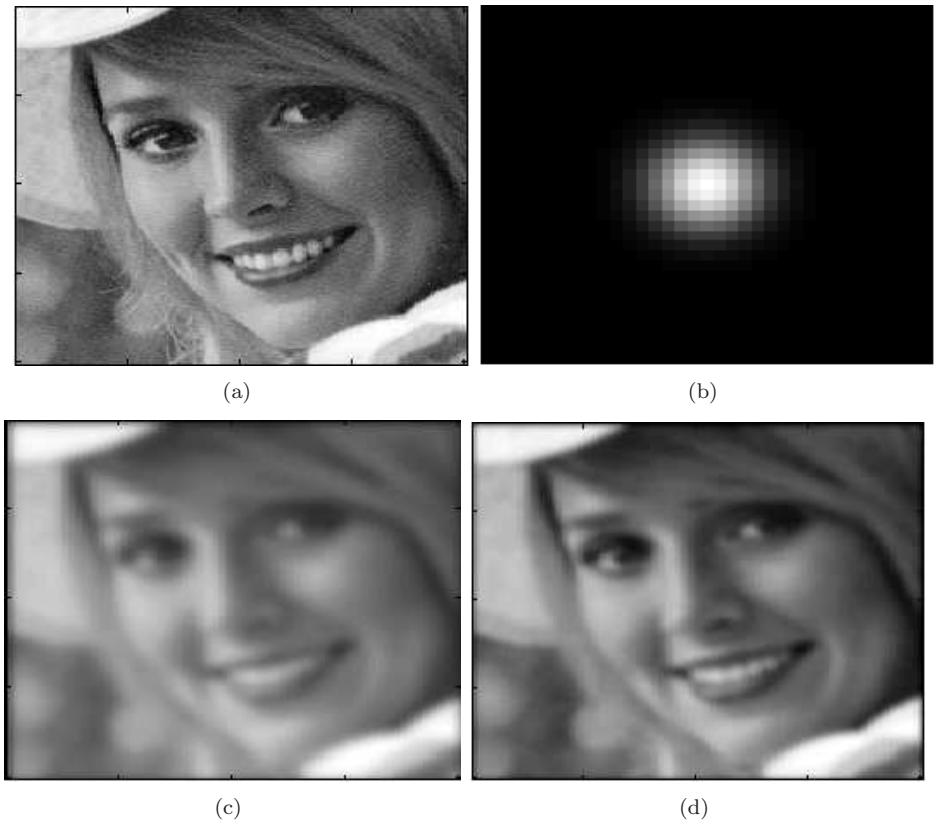

(a) (b)

(c) (d)

Figure 4.3: A 201×201 image (a) blurred with a 35X35 Gaussian. (b) The resultant image is shown in (c). The resulting reconstruction (d) was obtained after 17 rows and columns were discarded from the sides of the image.

algorithm does not know that the PSF is Gaussian. This resulted in a 235×235 blurred image.

This blurred image was cropped to the 201×201 image shown in Fig. 4.3(c) by discarding its $(L-1)/2 = 17$ outermost rows at the top and bottom, and its 17 outermost columns at the left and right. The algorithm was then run under the assumption that this missing data was all windowed to zero. The result is shown in Fig. 4.3(d). While the reconstruction is not perfect, it is a great improvement over the blurred image.

When the cropping is increased beyond discarding the $L/2$ outermost rows and columns, there is a marked degradation in performance. This is illustrated in Fig. 4.4(a). Fig. 4.4(a) is the original image of an eye. Fig. 4.4(b) is the image blurred

by a 7×7 Gaussian PSF. Of course, the algorithm does not know that the PSF is Gaussian. The blurred image was then cropped by discarding its $L - 1 = 6$ outermost rows and columns. The algorithm was then run under the assumption that this missing data was all windowed to zero.

Fig. 4.4(c) is the reconstructed image. There is little improvement over the blurred image. This is hardly surprising, since the support constraint information is no longer valid. Tests showed that there is a threshold at the level where the amount of cropping of the blurred image is half the size of the PSF $(L - 1)/2$. This threshold is not surprising, since beyond this amount of cropping the problem becomes underdetermined. The plot of mean-square error vs. amount of cropping of the blurred image is shown in Fig. 4.4(d).

4.6 Comparision of Rank-Reduction Procedures

4.6.1 Overview of Different Procedures

The next issue is: Which method should be used to determine the closest reduced-rank multilevel Toeplitz matrix to the given data matrix. Three different methods were explored:

1. Total Least Squares (TLS);
2. Structured Total Least Norm (STLN) [37];
3. Lift and Project (LAP) algorithm [8].

TLS means that we determine the closest (in the Frobenius norm sense) reduced-rank matrix to the given data matrix, *without regard to the structure of this matrix.* This amounts to finding the singular vector associated with the minimum singular value of the matrix.

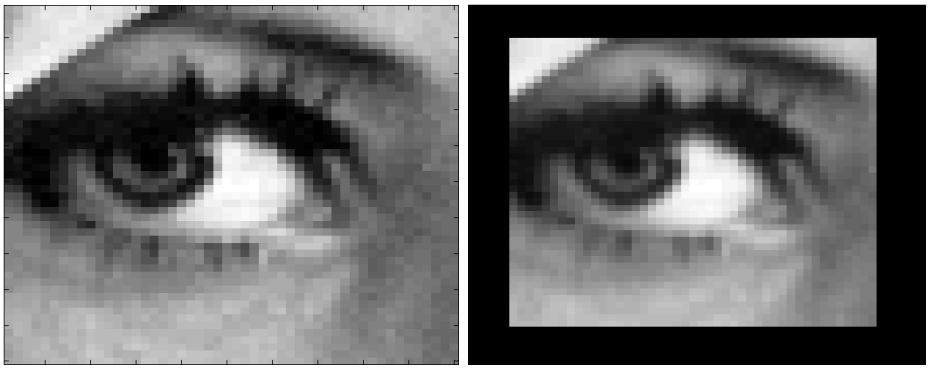

(a) (b)

(c)

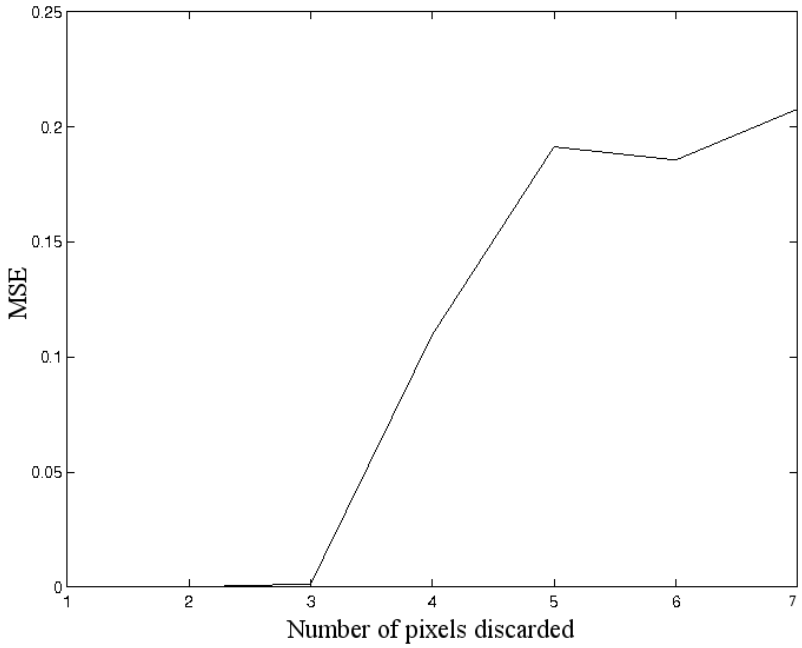

(d)

Figure 4.4: Performance of the deconvolution algorithm when only partial information is present. (a) is the original eye image that has been blurred by (b), a 7X7 Gaussian PSF. The reconstruction is shown in (c) showing little improvement. The plot in (d) shows the relation of Mean Square Error of the reconstruction with respect to the amount of pixels chopped from the edges before deconvolution was performed.

STLN is an incremental method in which the matrix is incrementally perturbed toward a reduced-rank matrix, while maintaining its multilevel Toeplitz structure [37].

LAP is an iterative procedure which works as follows [8]. First, the closest matrix (in the Frobenius norm sense) is found using TLS. Next, the matrix is then averaged along its diagonals (this is also known as *Toeplitzation*). The process is repeated until the increments in the solution are reduced to a preset tolerance.

The tolerance for STLN was set at $\epsilon = 10^{-8}$ with a limit of 100 iterations and ℓ_2 norm minimization. Least squares was used to solve the linear problem at each step. The conjugate gradient least squares (CGLS) method [63] was also tried for solving the linear problem encountered in each iteration of STLN. However, CGLS was found to be very time consuming and did not provide much improvement over least squares minimization when used in STLN.

All simulations were peformed using Matlab. Regularization tools developed for Matlab were also used [25].

4.6.2 Direct Method

The Direct Method is the method of Section III, without Fourier decomposition. Accordingly, only small images were used, in order to conduct an extensive numerical investigation.

A (4×4) test image was generated using **linspace.m** and convolved with a (2×2) even PSF. Zero-mean Gaussian white nose was added with SNRs varying from 0-55 dB. At every noise level, 100 noise realizations were used.

Results are given in Table 4.1. Note that STLN outperformed both LAP and TLS at high noise levels. However, TLS gave the best results at low noise levels. Even at high SNRs, STLN produced MSE$\approx$ 0.001.

Table 4.1: Comparison of MSE of TLS, LAP and STLN for Direct Method

SNR	0	5	10	15	20	25
LAP	.0759	.0477	.0410	.0201	.0179	.008
TLS	.0534	.0449	.0334	.0308	.0206	.0107
STLN	.0407	.0382	.0238	.0145	.0120	.0067

SNR	30	35	40	45	50	55
LAP	.0045	.0030	.0013	.0007	.0004	.0002
TLS	.0036	.0024	.0015	.0007	.0004	.0002
STLN	.0051	.0028	.0013	.0008	.0005	.0003

4.6.3 Fourier Decomposition Method

The Fourier decomposition method requires much less computation than the Direct method, so a larger test image could be used. A (61×61) downsampled image was convolved with an even (3×3) Gaussian-like even PSF. Gaussian white noise with SNRs varying from 0 dB to 55 dB was added, as before. At every noise level, 100 noise realizations were used.

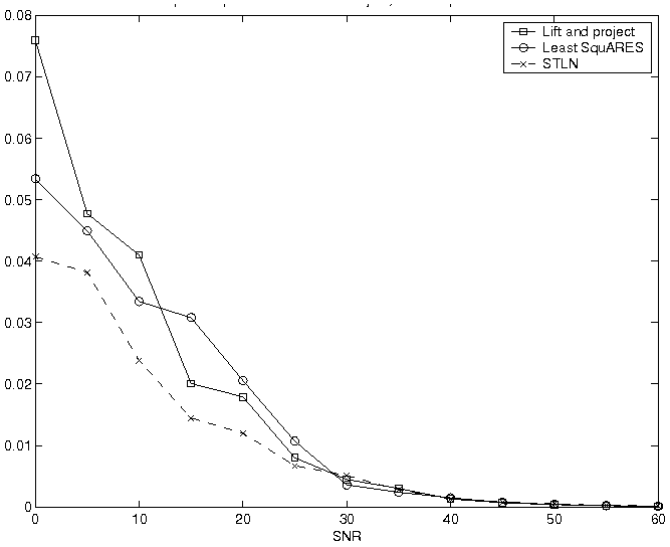

Figure 4.5: Comparision of MSE of TLS, LAP and STLN for Fourier Decomposition method.

Results are shown in Fig. 4.5. We use a plot here to distinguish these results for the Fourier decomposition from the results given in Table 4.1 for the Direct method. Typical reconstructed images are shown in Fig. 4.6(a)- 4.6(d). Note the following:

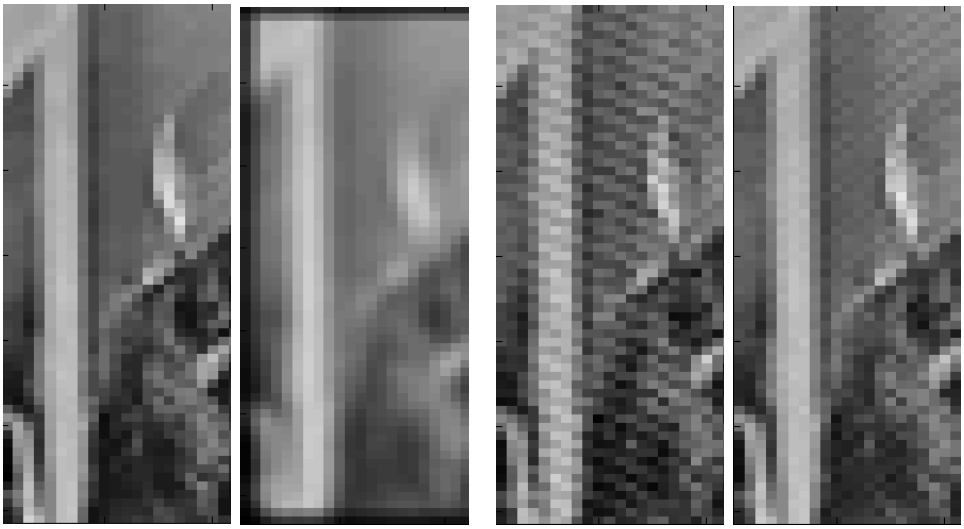

(a) (b) (c) (d)

Figure 4.6: (a) is a section of the original image which has been blurred as shown in (b). (c) is the TLS reconstruction. Significant improvement is observed in (d) which is the STLN reconstruction.

1. STLN gave better results than LAP and TLS;

2. Performance was somewhat worse for the Fourier decomposition method than for the Direct method. This is discussed below;

3. In particular, the reconstructed image using TLS had extensive ringing artifacts (see Fig. 4.6);

4. Our attempt to reduce this using regularization is discussed next.

4.6.4 Regularization

Next, we employed regularization techniques to improve the STLN results. Similar work has been done by Pruessner and O'Leary [65] in a method called RSTLN. In this method, Tikhonov regularization is applied during every iteration of the STLN algorithm. However, the regularization factor was found manually by studying the regularized image over a range of regularization values.

We attempted to improve on this by using the *L-curve method* [63] to determine

the regularization parameter. The L-curve of the matrix obtained while solving a small 2-D problem involving a (10×10) image convolved with a (3×3) PSF is shown in Fig. 4.7(a). (see below). Note that there is no corner point in the L-curve. Hence there is no clear choice for the regularization parameter. Furthermore, the condition number of the matrix was less than 1000 for many different test images.

We believe that the success of the Regularized Structured Total Least Norm (RSTLN) method can be attributed to the choice of test images[65], which have many black areas. We have found that such images, in the presence of noise, lead to ill-conditioned problems during deconvolution, making them suitable candidates for regularization). However, for test images (such as the Mandrill) with few zero-valued pixels, the matrices encountered in our blind deconvolution procedure are well-conditioned.

This is of course good news. It is worth reminding the reader that our procedure is a "direct" method in which the image is reconstructed without the necessity of deconvolving the PSF from it. But it also means that regularization is not helpful here.

4.6.5 Comparison of Direct and Fourier Decomposition Methods

Comparison of Table 4.1 and Fig. 4.5 shows that the Fourier decomposition method, which requires much less computation than the Direct method, does suffer from some relative degradation of performance. This is not surprising; recall that the Fourier decomposition is discarding the support constraint in one direction. But it is important to perform a direct comparison of our two approaches, to see if this loss is acceptable.

Extensive numerical studies of the Direct method again requires that the images be small. We considered three image sizes: (4×4); (8×8); and (14×14). In all

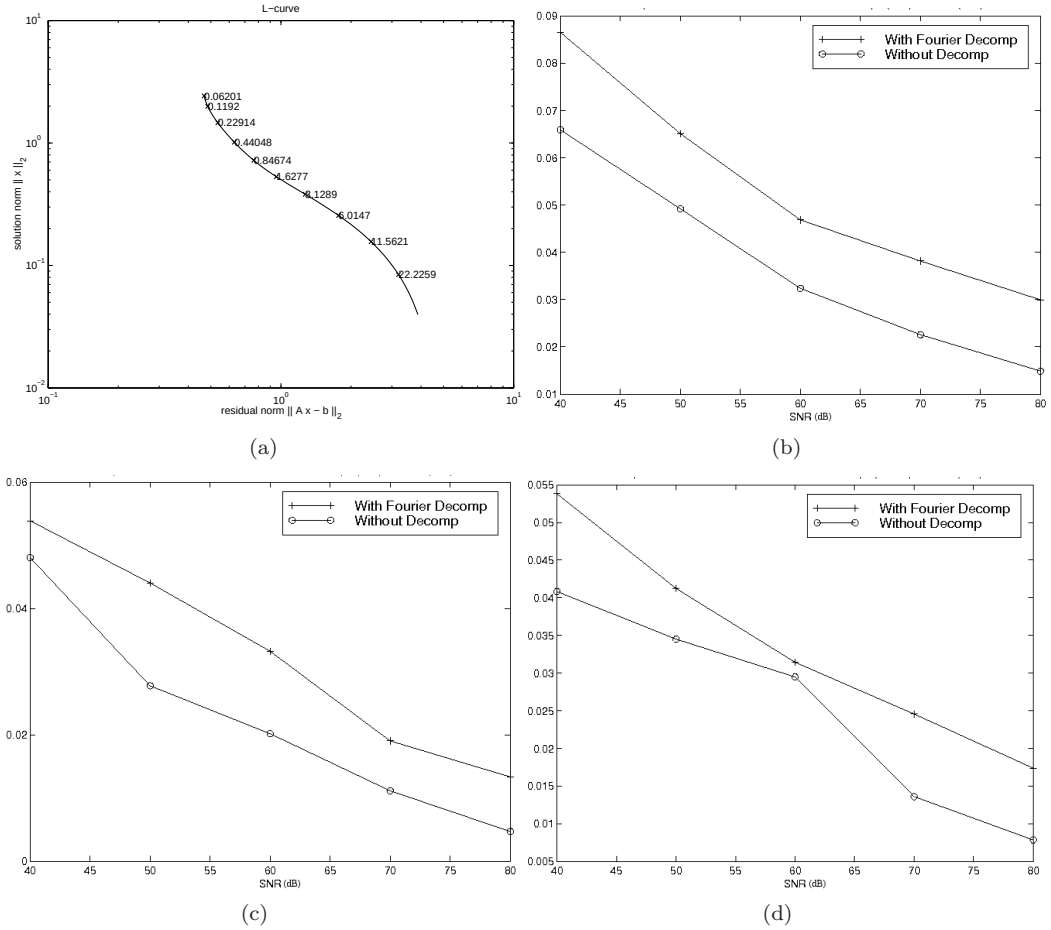

Figure 4.7: (a) L-curve obtained during the deconvolution of a 10X10 image with a 3X3 PSF. Figures (b)-(d) show the MSEs obtained using the Fourier decomposition and direct methods when deconvolution was performed on 4×4, 8×8 and 14×14 images convolved with a 3×3 PSF respectively.

three cases, an unknown (except for being even) Gaussian-like (3×3) PSF was used. White Gaussian noise was added at various SNRs. At every noise level, 100 noise realizations were used.

Results are given in Fig. 4.7(b)-4.7(d), respectively. In each case, the Fourier decomposition method had a larger average MSE than the Direct method. However, it is our judgment that the enormous computational savings of the Fourier decomposition method are worth the higher MSE incurred.

4.7 Conclusion

We have formulated the single-channel 2-D blind deconvolution problem with an even PSF as a linear algebra problem in which the unknown image pixel values are components of the null vector of a Toeplitz-block-Toeplitz matrix of the observed blurred image. Hence the image is found directly; it need not be deconvolved from its blurred version. Two different methods were proposed: one solved the 2-D problem directly; the other decomposed the problem into multiple decoupled smaller 1-D problems. The latter method requires much less computation, but it also has a larger MSE in noise. Our judgment is that the latter method is nonetheless preferable.

Several numerical tests were performed. These included perfect noiseless reconstruction of large (e.g., (452×452)) images and comparison of the above two methods for several different image sizes. Furthermore, three linear algebraic methods for computing the nearest reduced-rank Toeplitz-block-Toeplitz matrix to the given data matrix were compared. It was found that STLN seems to work better than LAP or TLS except in the very low noise level case, in which case TLS worked best (and also required the least amount of computation). However, at lower SNRs, TLS not only gave poorer results but also produced reconstructed images with ringing artifacts. Attempts to correct this with regularization were not successful, and reasons for this were given. We also noted that the partial data case in which a cropped version of the blurred image is used still gave results that were a great improvement over the blurred image.

We have extended the results of this paper to the 3-D case[88]. The scale factor problem becomes much more significant and difficult in the 3-D case, enough so that separate publication is warranted.

CHAPTER V

3-D blind deconvolution of even point-spread functions from compact support images

5.1 Introduction

3-D blind deconvolution refers to the reconstruction of a 3-D image with compact support from its 3-D convolution with an unknown blurring or point spread function. This problem arises frequently in optical sectioning microscopy. Though normally used for deblurring wide-field images it is increasingly being used for improving the resolution of images obtained from confocal microscopy.

In applications such as microscopy where the images are optical in nature, the point-spread function may be assumed to be symmetric i.e. an even function of spatial variables. This is due to reciprocity i.e., an even function of its spatial variables. This is due to reciprocity;if an excitation at spatial position x_o produces a given electromagnetic field at y_o,then the same excitation at y_o should produce the same electromagnetic field at x_o. If the Green's function is translation-invariant $(G(x_o, y_o) = G(x_o - y_o))$,then $G(x_o - y_o) = G(y_o - x_o)$ and $G(\cdot)$ is an even function.

Since both the image and the point-spread function can be assumed to have finite spatial extent (i.e., finite support), their Fourier transforms may be sampled in wavenumber. Most images are approximately bandlimited to the extent that they may also be sampled spatially as well. This leads to the discrete version of this

problem, in which a discrete-time image known to have finite spatial extent is to be reconstructed from its convolution with an also-unknown point-spread function (PSF).

Current deconvolution techniques used in microscopy include the Lucy-Richardson method [48, 68], the Ayers-Dainty method [24], ITCM and Carrington methods[81]. Most of these methods are non-blind iterative methods that require thousands of iterations and are not guaranteed to converge. Methods based on minimization of a residual require good priors for both the image and the PSF which are often not available. PSFs are estimated using polystyrene beads in microscopy. However, this is a tedious task prone to measurement error [55]. These difficulties motivate the use of non-iterative blind deconvolution methods such as the one described in this paper.

5.1.1 Problem Formulaton

The 3-D discrete blind deconvolution problem is as follows [41]. We observe

$$y(i_1, i_2, i_3) = h(i_1, i_2, i_3) * * * u(i_1, i_2, i_3) + n(i_1, i_2, i_3) \tag{5.1}$$

where $* * *$ denotes convolutions in i_1, i_2 and i_3. The 1-D convolution $*$ is defined here as

$$h(n) * u(n) = \sum_{i=0}^{n} h(n-i)u(i) = \sum_{i=0}^{n} h(i)u(n-i). \tag{5.2}$$

We make the following assumptions:

1. $u(i_1, i_2, i_3) \neq 0$ only for $0 \leq i_1, i_2, i_3 \leq M-1$;
2. $h(i_1, i_2, i_3) \neq 0$ only for $0 \leq i_1, i_2, i_3 \leq L-1$;
3. $y(i_1, i_2, i_3) \neq 0$ only for $0 \leq i_1, i_2, i_3 \leq N-1$;

4. $h(i_1, i_2, i_3) = h(L - i_1, L - i_2, L - i_3)$ (even PSF); $N = L + M - 1$;

5. $n(i_1, i_2, i_3)$ is a zero-mean white Gaussian noise random field;

6. All quantities are real functions.

Given knowledge of only the data $y(i_1, i_2, i_3)$, the goal is to reconstruct the image $u(i_1, i_2, i_3)$ and point-spread function (PSF) $h(i_1, i_2, i_3)$; hence the term "blind deconvolution." No stochastic assumptions are made about either the image or the point-spread function. This precludes use of methods based on cumulants, ARMA or Poisson image models or stochastic equalization.

In many applications, only partial information about $Y(i_1, i_2, i_3)$ is available. For example:

$$Y(i_1, i_2, i_3), 0 \leq i_1, i_2, i_3 \leq M - 1$$

i.e. the size of the blur image is the same as that of the original image. We will show that even in this case, good results are sometimes obtained using our method.

The problem addressed in this paper should be distinguished from the problem of *multiple-blur* blind deconvolution, which has been addressed in many recent papers. In the latter problem, a single unknown signal or image is filtered with several unknown blurring functions, resulting in several known outputs. This is conceptually a much simpler problem than the *single-blur* blind deconvolution problem.

5.1.2 Problem Ambiguities

There are three trivial ambiguities to the 3-D blind deconvolution problem:

1. *Scale factor:* If $\{h(i_1, i_2, i_3), u(i_1, i_2, i_3)\}$ is a solution, then $\{ch(i_1, i_2, i_3), \frac{1}{c}u(i_1, i_2, i_3)\}$ is also a solution for any real constant c. If c cannot be determined from the image energy, it usually is irrelevant. We consider the problem to be solved when the image is determined to a scale factor.

2. *Translation:* If $\{h(i_1, i_2, i_3), u(i_1, i_2, i_3)\}$ is a solution, then $\{h(i_1+d_1, i_2+d_2, i_3+d_3), u(i_1-d_1, i_2-d_2, i_3-d_3)\}$ is also a solution for any constants d_1, d_2, d_3. We eliminate this ambiguity by specifying the supports in (2).

3. *Exchange:* We need to be able to distinguish $h(i_1, i_2, i_3)$ from $u(i_1, i_2, i_3)$. Since $h(i_1, i_2, i_3)$ is an even function by assumption, this requires that the image not *also* be an even function, or that $L \neq M$.

We assume that the 3-D z-transforms

$$H(x, y, z) = \sum_{i_1=0}^{L-1} \sum_{i_2=0}^{L-1} \sum_{i_3=0}^{L-1} h(i_1, i_2, i_3) x y z^{-i_1-i_2-i_3} \tag{5.3}$$

and

$$U(x, y, z) = \sum_{i_1=0}^{M-1} \sum_{i_2=0}^{M-1} \sum_{i_3=0}^{M-1} u(i_1, i_2, i_3) x y z^{-i_1-i_2-i_3} \tag{5.4}$$

are irreducible (they cannot be factored). This is almost surely true [44]. One way to see this quickly is to note that in the noiseless case, (5.1) is $N^3 = (L + M - 1)^3$ simultaneous quadratic equations in $L^3 + M^3$ unknowns. Since the problem is overdetermined, by Bezout's theorem there is almost surely no more than one solution. In fact, there are generically *no* solutions; only from (5.1) do we know that there is a perturbation of the data for which a solution exists.

5.2 2-D and 3-D Solution

5.2.1 2-D Solution

It is essential to understand the solution of the 1-D and 2-D problem to understand the solution of the 3-D problem. We shall review noiseless 2-D blind deconvolution first. The 2-D solution is an extension of the 1-D solution [71].

Taking 2-D z-transform of the noiseless 2-D version of (5.1) yields

$$Y(z_1, z_2) = H(z_1, z_2)U(z_1, z_2) = (z_1 z_2)^L H(\frac{1}{z_1}, \frac{1}{z_2})U(z_1, z_2) \tag{5.5}$$

since $h(i_1, i_2) = h(L - i_1, L - i_2)$. This leads to

$$Y(z_1, z_2)(z_1, z_2)^M U(\frac{1}{z_1}, \frac{1}{z_2}) = (z_1 z_2)^N Y(\frac{1}{z_1}, \frac{1}{z_2})U(z_1, z_2) \tag{5.6}$$

Equating coefficients leads to a block Toeplitz matrix with Toeplitz blocks. This is known as Toeplitz block Toeplitz or multilevel Toeplitz structure. The matrix is formed by nesting the Toeplitz matrices that implement 1D convolutions. The matrix size is

$$(N + M - 1)^2 \times (2M^2) = (2M + L - 2)^2 \times (2M^2) \tag{5.7}$$

.

The matrix is overdetermined if $L > 2$. However, the overdetermination is much greater than in the 1-D case. The 2-D problem is best understood with an example.

5.2.2 Fourier Decomposition in 2-D

The 2-D problem is solved by solving a system of equations of a block Toeplitz matrix whose size is given by (5.7). This matrix quickly grows in size, even for small problems. For instance: If $M = 5$ and $L = 3$, then the size of the matrix is 121×50. The huge size of these matrices demonstrate the need for a formulation that can decouple this large system of equations into smaller systems. This can be done as follows.

Let $x_k = e^{j2\pi k/M}$ and y_k be similarly defined. Setting $z_2 = y_k$ in (5.6) yields

$$Y(z_1, y_k)(z_1 y_k)^M U(\frac{1}{z_1}, \frac{1}{y_k}) = (z_1 y_k)^N Y(\frac{1}{z_1}, \frac{1}{y_k})U(z_1, y_k) \tag{5.8}$$

Since $y(i_1, i_2)$ and $u(i_1, i_2)$ are real, conjugate symmetry allows (5.8) to be rewritten as

$$Y(z_1, y_k) y_k^M z_1^M U^*(\frac{1}{z_1^*}, y_k) = y_k^N z_1^N Y^*(\frac{1}{z_1^*}, y_k) U(z_1, y_k) \tag{5.9}$$

since $|y_k| = 1$. We recognize (5.9) as a decoupled (in k) set of 1-D complex-valued blind deconvolution problems. Each of these can be solved in parallel.

Another way to see this quickly is to note that since $h(i_1, i_2)$ is a real and even function, its 2-D discrete Fourier transform $H(z_{1i}, z_{1j})$ ($H(z_1, z_2)$ sampled on the unit circle) will also be a real and even function. Hence the singly-transformed $\tilde{h}(i_1, y_k)$ will also be real and even. This shows most directly why the decoupled 1-D problems have even PSFs. Of course the FFT may be used to compute quickly $Y(z_1, y_k)$ from $y(i_1, i_2)$ and also to compute $u(i_1, i_2)$ from $U(z_1, y_k)$.

5.2.3 Scale Factors in 2-D

The problem is not completely solved yet. Each decoupled 1-D problem is only solvable to a scale factor. Hence (5.9) only yields $c_k U(x, y_k)$, where c_k is the unknown scale factor for the k^{th} problem. The c_k must be determined in order to recover $u(i_1, i_2)$.

The easiest way is to solve (5.9) for $c_k U(x, y_k)$ and (23) for $d_k U(x_k, y)$. We then read off the relative ratios of the c_k from the latter, and the relative ratios of the d_k from the former. There is still an overall scale factor ambiguity, as expected.

5.2.4 3-D Blind Deconvolution

We now specify our new procedure for 3-D blind deconvolution. All of the results to follow are new.

The 3-D analogue to (5.5) is

$$(5.10)\quad Y(z_1,z_2,z_3)=H(z_1,z_2,z_3)U(z_1,z_2,z_3)=(z_1z_2z_3)^L H(\frac{1}{z_1},\frac{1}{z_2},\frac{1}{z_3})U(z_1,z_2,z_3)$$

This leads to

$$(5.11)\quad Y(z_1,z_2,z_3)=(z_1z_2z_3)^M U(\frac{1}{z_1},\frac{1}{z_2},\frac{1}{z_3})=(z_1z_2z_3)^N Y(\frac{1}{z_1},\frac{1}{z_2},\frac{1}{z_3})U(z_1,z_2,z_3)$$

Equating coefficients would result in a doubly nested Toeplitz matrix. The matrix size is now $(N+M-1)^3\times(2M^3)=(2M+L-2)^3\times(2M)^3$. If $M=8$ and $L=3$ then the matrix would be 4913×1024 in size. It is evident that without Fourier decomposition, 3-D blind deconvolution would be impractical using this approach.

5.2.5 Fourier Decomposition in 3-D

Let $x_k=e^{j2\pi k/M}$ and y_k and z_k be similarly defined. Setting $y=y_k$ in (5.11) yields

$$(5.12)\quad Y(z_1,y_k,z_3)(z_1y_kz_3)^M U(\frac{1}{z_1},\frac{1}{y_k},\frac{1}{z_3})=(z_1y_kz_3)^N Y(\frac{1}{z_1},\frac{1}{y_k},\frac{1}{z_3})U(z_1,y_k,z_3)$$

Conjugate symmetry allows us to rewrite the above equation as

$$(5.13)\quad Y(z_1,y_k,z_3)(z_1y_kz_3)^M U^*(\frac{1}{z_1^*},\frac{1}{y_k},\frac{1}{z_3^*})=(z_1y_kz_3)^N Y^*(\frac{1}{z_1^*},\frac{1}{y_k},\frac{1}{z_3^*})U(z_1,y_k,z_3)$$

We recognize the above equation as a coupled set of 2-D problems. Each of these 2-D problems can further be solved by decoupling them into a set of 1D problems as shown before. The same can be done by substituting $z_1=x_k$ or $z_3=z_k$, leading to the following expressions.

$$(5.14)\quad Y(x_k,z_2,z_3)(x_kz_2z_3)^M U^*(\frac{1}{x_k},\frac{1}{z_2^*},\frac{1}{z_3^*})=(x_kz_2z_3)^N Y^*(\frac{1}{x_k},\frac{1}{z_2^*},\frac{1}{z_3^*})U(x_k,z_2,z_3)$$

$$(5.15)\quad Y(z_1,z_2,z_k)(z_1z_2z_k)^M U^*(\frac{1}{z_1^*},\frac{1}{z_2^*},\frac{1}{z_k}) = (z_1z_2z_k)^N Y^*(\frac{1}{z_1^*},\frac{1}{z_2^*},\frac{1}{z_k})U(z_1,z_2,z_k)$$

5.2.6 Scale Factors in 3-D

As in the 2-D case, each decoupled 2-D problem is only solvable to a scale factor. Hence (5.13) yields $c_kU(z_1,y_k,z_3)$. In other words, we have slices of the solutions, depending on the way in which the 3-D problem was decoupled. Each slice has the right solution to a scale factor, and hence we have to scale these slices with respect to a common coefficient.

An easy way to achieve this is to solve (5.13) for $c_kU(z_1,y_k,z_3)$, (5.14) for $d_kU(x_k,z_2,z_3)$ and (5.15) for $e_kU(z_1,z_2,z_k)$, and read off relative ratios using two of the three given sets of coefficients. The choice of which two sets to use is arbitrary, and in fact one could perform all three possible combinations to choose the best possible reconstruction. This is useful especially when a 3-D image matrix might have a non-trivial nullspace along a certain direction.

5.2.7 Implementation Issues

Specific to the 3-D case, there are a few implementation issues that we need to report. 3-D images obtained from microscopy often have many black areas representing zeros in the digitized format. When we take the 1-D Fourier transform along a direction, it is quite likely that we obtain a 2-D problem, that has a non-trivial null space. This causes problems, as one of the assumptions, for solving the 2-D case is that the nullspace has dimension one.

One way of overcoming this is to add minute quantities of broadband noise (variance of the order of 10^{-6} of the signal power levels). This seems to avoid the multidimensional nullspace problem. In practice, there will always be some additive noise

[44] anyway, so this is reasonable.

We also note that since the PSF is even and if its size is an even intege0r, then its 3-D DFT will have zeros at $\omega_k = \pi$ To see this consider the 1-D even PSF $h_0, h_1, h_2, h_2, h_1, h_0$

Real images often have a zero at $\omega = \pi$;indeed, there should. If the image is properly sampled using a DFT of odd order (which does not use $\omega = \pi$) , then the problem seems to be avoided.

5.3 Noisy Data Case

5.3.1 Formulation

We now consider the noisy data problem (1). Our approach generalizes the approach we used in [71] for the 2-D case.The log-likelihood function is

(5.16)

$$\log p_{Y|U}(y|u) = -\frac{N^2}{2}\log(2\pi\sigma^2) - \frac{1}{2\sigma^2}\sum_{i_1=0}^{N-1}\sum_{i_2=0}^{N-1}\sum_{i_3=0}^{N-1}[y(i_1,i_2,i_3) - h(i_1,i_2,i_3) *** u(i_1,i_2,i_3)]^2.$$

Since the problem is overdetermined, the maximum likelihood estimate (MLE) of $u(i_1, i_2, i_3)$ is the solution to a 3-D blind deconvolution problem in which the noisy data $y(i_1, i_2, i_3)$ has been replaced with $\hat{y}(i_1, i_2, i_3)$. $\hat{y}(i_1, i_2, i_3)$ has the following two properties:

1. A solution exists to the overdetermined blind deconvolution problem

$$\hat{y}(i_1, i_2, i_3) = \hat{h}(i_1, i_2, i_3) * * * \hat{u}(i_1, i_2, i_3)$$

2. $\sum_{i_1=0}^{N-1}\sum_{i_2=0}^{N-1}\sum_{i_3=0}^{N-1}[y(i_1, i_2, i_3) - \hat{y}(i_1, i_2, i_3)]^2$ is minimized.

That is, we need to find the minimum least-squares norm perturbation of the noisy data $y(i_1, i_2, i_3)$ to admissible data $\hat{y}(i_1, i_2, i_3)$ for which a solution to the overde-

termined 2-D blind deconvolution problem exists. Then $\hat{u}(i_1, i_2, i_3)$ is the MLE of $u(i_1, i_2, i_3)$.

Another way to say this is that we need to project the noisy data onto the set of admissible data for which the overdetermined problem can be solved.

5.3.2 Resultant Solution

Fortunately, the formulation (5.11) allows a straightforward solution to this problem. Since each column of the resultant matrix R consists of the noisy data $y(i_1, i_2, i_3)$ unwrapped by columns and some zeros (similar to the 2-D case), we have

$$3M^2 \sum_{i_1=0}^{N-1} \sum_{i_2=0}^{N-1} \sum_{i_3=0}^{N-1} [y(i_1, i_2, i_3) - \hat{y}(i_1, i_2, i_3)]^2 = ||R - \hat{R}||_F^2 \tag{5.17}$$

where

1. R is the resultant matrix constructed from $y(i_1, i_2, i_3)$;
2. $\hat{R}$ is the resultant matrix constructed from $\hat{y}(i_1, i_2, i_3)$;
3. The $3M^2$ comes from the $3M^2$ columns of R and $\hat{R}$. We note that in the 2-D case there are $2M^2$ columns in R and $\hat{R}$.
4. $||A||_F^2 = \sum_{i=1}^{N} \sum_{j=1}^{N} \sum_{k=1}^{N} |A_{i,j,k}|^2$ is the Frobenius or Hilbert-Schmidt matrix norm of a matrix A (excluding a factor of N).

Hence the problem has been reformulated as follows: Compute the minimum Frobenius norm perturbation $\hat{R}$ of R such that: (1) $\hat{R}$ keeps the multilevel Toeplitz structure of R; and (2) $\hat{R}$ drops rank.

This is a well-know problem in linear algebra. There are at least two known approaches: (1) structured total least squares (STLS) [37] ; and (2) iterative projection. Since these are quite well known we do not review them here.

5.3.3 Fourier Decomposition

We show that if the above approach is applied to the Fourier decomposition of the 3-D blind deconvolution problem, the result is the maximum likelihood estimator for a problem with fewer constraints.

Consider the problem defined by (1), but with the support constraints

1. $u(i_1, i_2) \neq 0$ only for $0 \leq i_1 \leq M - 1$;

2. $h(i_1, i_2) \neq 0$ only for $0 \leq i_1 \leq L - 1$;

3. $y(i_1, i_2) \neq 0$ only for $0 \leq i_1, i_2 \leq N - 1$.

That is, the image and PSF have support constraints in only one dimension, even though their 3-D convolution is constrained in three dimensions. In the noiseless case this makes no difference; there is only one solution (to a scale factor), so dropping some of the constraints has no effect, as long as the remaining constraints are sufficient to determine a unique solution. In the noisy case, where we are projecting the data onto the set of feasible solutions, fewer constraints means the closest feasible data set is likely to be different from before. Then the reconstructed image will have some energy in the unconstrained region. But for low noise levels, this is unlikely to matter much.

Using the Fourier decomposition (5.14) produces a set of decoupled 2-D blind deconvolution problems, which can further be broken into 1-D problems so that no support constraints are imposed in either the y or z direction (depending on how the 2-D problem is decoupled). This is precisely the problem defined above. Hence solving each of the decoupled 1-D noisy blind deconvolution problems separately and then combining them will produce the maximum likelihood estimate for the above problem, since

1. The k^{th} 1-D problem will involve the doubly-transformed data $\tilde{y}(i_1, y_k, z_k)$, which will be arranged into a resultant matrix. Since the different Fourier components are independent, the perturbations used in one problem have no effect or constraint on those used in another problem;

2. To ensure this, use $y_k = e^{\frac{j2\pi k}{N-1}}$ to obtain N different 2-D problems. Further, use $z_k = e^{\frac{j2\pi k}{N-1}}$ to obtain N different 1-D problems to each of the 2-D problems. Since $M < N$, this also provides a constraint when the 1-D problem estimates are recombined into the 2-D problem estimate and further on to the 3-D estimate; this can only help;

3. The total squared perturbation of $y(i_1, i_2, i_3)$ is the square of the sum of the magnitude-squared perturbations of the 1-D problems, by Parseval's theorem.

5.3.4 Overview of Simulations

Simulations were performed to study the following major effects:

- Performance in the absence of noise
- Performance with noise
- Comparison with Lucy Richardson algorithm

5.3.5 Performance in the Absence of Noise

A 30×30×30 simulated image of a bead (Figure (5.1)) with a background intensity gradient was convolved with a 3×3×3 PSF in the absence of noise. The mean square error between the deconvolved image and the original phantom was measured and was found to be of the order of 10^{-31}. The results is shown in Figure (5.2). Figure (5.3) shows the convolution of the same image with a $5 \times 5 \times 5$ Gaussian PSF with the edges clipped off (partial problem). Figure (5.4) displays the deconvolution of

the same. Note that the deconvolved image is still blurry. The MSE here was of the order of 10^{-3}.

5.3.6 Performance in Noise

In the 3-D blind deconvolution algorithm, the critical step determining solution accuracy is when the null space of a block Toeplitz matrix as to be found. Therefore, we studied the algorithms performance using

1. *Least Squares* which is fast but does not exploit the structure of the Toeplitz matrix, and

2. *Structured Total Least Norm (STLN)* which is slower but uses the matrix structure. [37]

The tolerance for STLN was set at $\epsilon = 10^{-8}$ with a 100 iterations maximum limit and was solved for a 2 norm minimization. The results are shown. STLN is clearly better at low and medium SNRs, but at high SNRs, least squares gives us better solutions. We also noticed that the lowest SNR needed to achieve a MSE lower than a specified bound increased as the size of the input image increased. We speculate this is because of the increased ill-conditioning of the problem associated with the increase in the image size.

5.3.7 Scaling Comparisons

As noted previously, one could use two of the three solutions obtained, to deconvolve the 2D slices. The graph shows that for this 10×10×10 image x vs y scaling always yielded the best results while that of x versus z yielded the worst. This is not always true. Infact sometimes, the opposite is true. In other words, the accuracy of deconvolution obtained by using a given set of slices depends on the image itself.

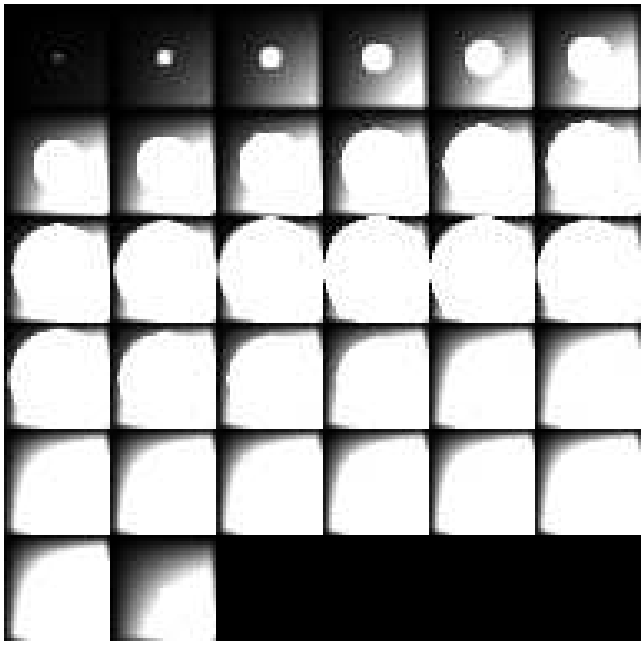

Figure 5.1: 30×30×30 bead image convolved with 3×3×3 PSF

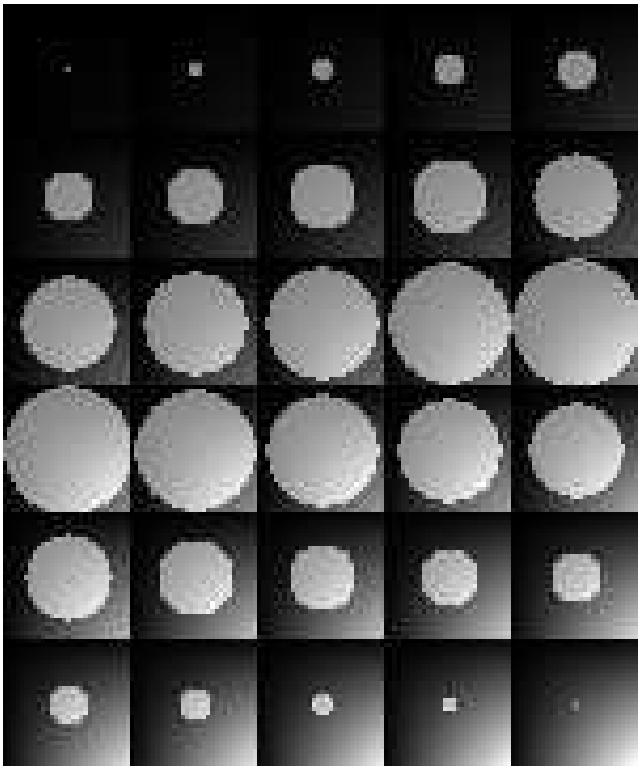

Figure 5.2: Deblurred image

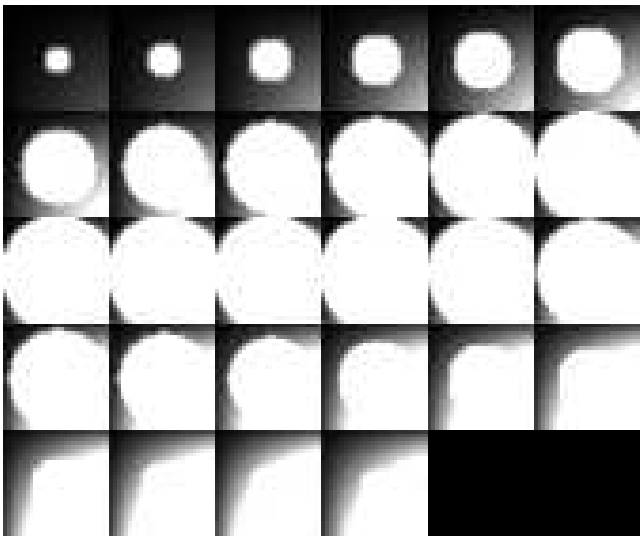

Figure 5.3: 30×30×30 bead image convolved with 5×5×5 PSF with sides clipped off.

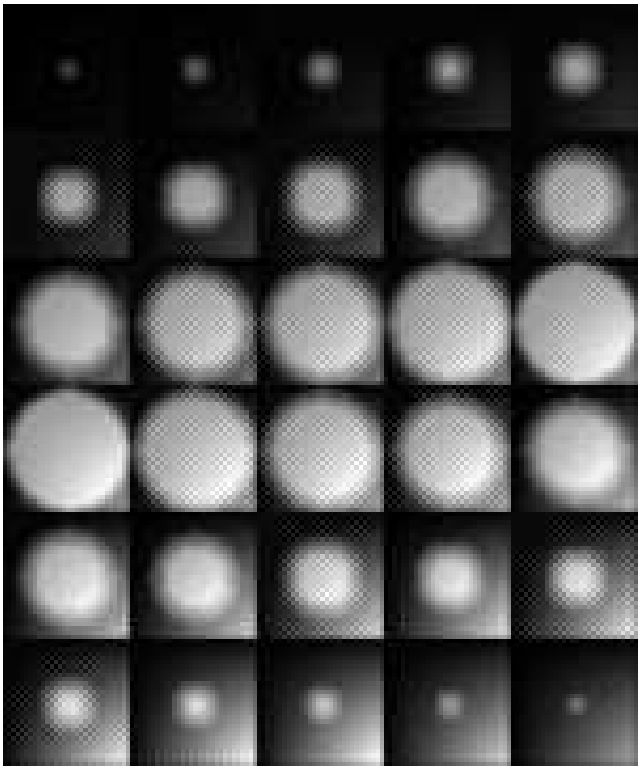

Figure 5.4: Deblurred image. Note that the image is still a little blurry.

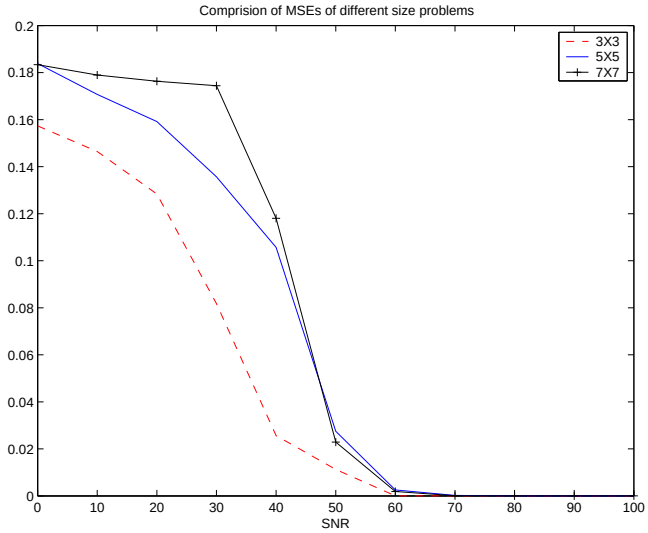

Figure 5.5: MSE v/s SNR Comparisons of deconvolution of 3×3×3,5×5×5 and 7×7×7 images with 3×3 PSF

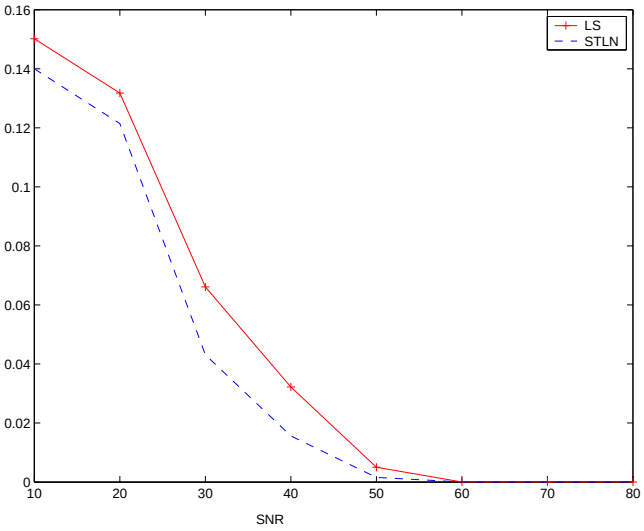

Figure 5.6: MSE v/s SNR of STLN and Least Squares for a 9×9×9 image with a 3×3×3 PSF

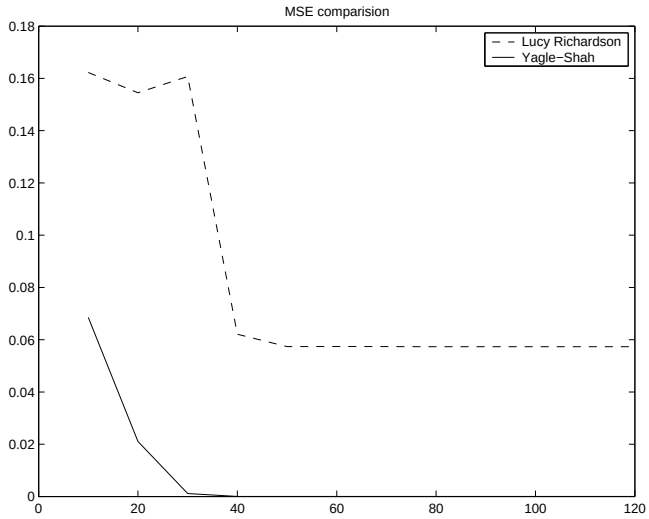

Figure 5.7: MSE v/s SNR comparisions for our algorithm with Lucy-Richardson . Image:7×7, PSF 3×3

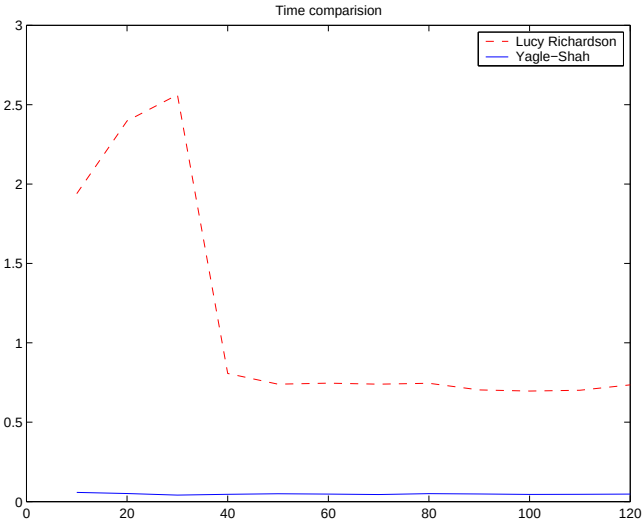

Figure 5.8: Solution time v/s SNR comparison for our algorithm with Lucy-Richardson. Time axis is in seconds. Image 7×7, PSF 3×3

This is easily understood when one realizes that for an ideal solution one requires that the resultant matrix be well conditioned when the 1-D Fourier transform of the 3-D signal is taken along x,y or z. This is easily met for noiseless signals. But for most real images with lots of zero areas (black areas), the presence of even tiny amounts of noise makes the problem ill-posed along a certain direction. However, one could always check to see which scaling yields the best results and hence this is not a serious problem.

5.3.8 Comparison with Lucy-Richardson Algorithm

To test the effectiveness of the algorithm we compared the 2-D version of the algorithm to it to the 2-D Lucy-Richardson algorithm for both speed and effectiveness of deconvolution.

We found that for all the images we tested, our algorithm gave a lower MSE and also took a much lower time to solve. The figures show two such examples. The example as shown in Figure (5.7) compares the deconvolution of a 7×7 image with a 3×3 PSF at different SNRs. The results are averaged over 50 iterations. The time to solve in seconds is shown in Figure (5.8).

5.4 Conclusions

We have shown that

1. It is possible to formulate 3-D blind deconvolution problems with even point spread functions as a linear problem in the unknown image pixel values, although the data are used in a nonlinear manner.

2. In the presence of noise, STLN gives better results than conventional least squares. In the presence of Gaussian noise; these results are the maximum likelihood estimates of the original image.

3. Fourier decoupling is a very effective tool when solving the deconvolution problem for large 3-D matrices.

4. Compared to Lucy-Richardson, this algorithm is superior both in terms of the accuracy of the solution and time needed to solve the problem.

CHAPTER VI

QUILL: A blind deconvolution algorithm for the partial data problem

6.1 Introduction

6.1.1 Overview

The problem of blind deconvolution has been an active area of research for approximately the past thirty years [48]. The 2-D version of the problem appears in areas such as astronomy [40, 41], microscopy [53] and remote sensing [38]. For a good review of the history and applications of blind deconvolution, we refer the reader to [44].

2-D deconvolution refers to the problem of reconstructing a 2-D image from its 2-D convolution with a point-spread function (PSF). Often, the PSF is known, or at least known to a very good approximation. There are several methods to solve this problem such as Lucy-Richardson [48] or Maximum Entropy deconvolution [60]. However, in many cases the PSF is *unknown*. This leads to the *blind* version of the problem. 2-D blind deconvolution refers to deconvolving the 2-D object from its convolution with a PSF when the PSF is not known.

Most images are approximately bandlimited to the extent that they may be spatially sampled. This leads to the *discrete* version of this problem, in which a discrete image is to be reconstructed from its discrete convolution with an also-unknown dis-

crete PSF. If the PSF is known, this becomes the solution of an often-ill-conditioned linear system of equations. When the PSF is unknown, the problem is even harder.

A common approach for blind deconvolution problems is to use an iterative transform algorithm [44, 24] which alternates between spatial and wavenumber domains. However, these algorithms often stagnate, failing to converge to a solution [24]. Another approach, NAS-RIF [45] is guaranteed to converge, but it requires the existence of a small-support inverse filter.

The problem addressed in this paper should be distinguished from the problem of *multiple-channel blind deconvolution* which has received much attention of late [28, 21, 62, 75]. In this problem, a single unknown signal or image is filtered with several unknown PSFs resulting in several known outputs. This is conceptually much simpler than the single blur problem addressed here. To see this quickly, note that an unknown 1-D signal with compact support can be recovered from its convolutions with two unknown 1-D PSFs with compact support by simply computing the greatest common divisor of the z-transforms of the two known convolutions.

6.1.2 The Partial Data Problem

In many applications, such as remote sensing or microscopy, the unknown image often does not have compact support. Rather, it is just part of a bigger image. The blurred image that constitutes the data is actually smaller than the image to be reconstructed. This is called the *partial data problem* [28].

The difficulty of the partial data problem can be seen by noting that even if the PSF is known, the image cannot be uniquely determined. This is evident since the deconvolution problem with an unknown PSF becomes an underdetermined system of linear equations. We overcome this problem by using an image model that decomposes the single blur problem to that of a single image with four blurs. By doing

this, we will show how a unique solution can be obtained.

6.1.3 New Contributions of This Paper

The specific contributions of this paper to the single-blur partial-data 2-D blind deconvolution problem are as follows:

1. Solution of the partial data problem requires an image model. We propose a QUILL (Quincunx-Upsampled Interpolated LinearLy) image model which upsamples or expands (inserts zeros) into a Quincunx-sampled image, and then interpolates it using linear splines. This model seems to represent oversampled images quite well;

2. Using this model, we reformulate the single-blur blind deconvolution problem as a four-channel multiple-blur blind deconvolution problem, which has been studied extensively in the literature of late [28, 21, 62, 75];

3. We employ a 2-D version of Bezout's lemma to enable us to solve for *deconvolvers*, rather than the point-spread function itself. Since the reconstructed image is just a convolution of this deconvolver with the data, our algorithm is a *direct* method, effectively reconstructing the image directly without estimating the PSF and then deconvolving it from the data;

4. We provide several examples, using various types of images and PSFs. This includes: (1) two real-world images convolved with known PSFs, so that the reconstructed image can be compared to the true image; and (2) two truly blind examples in which the algorithm was simply applied directly to real data of a real-world blurred image; both the PSF and image are unknown.

The rest of the paper is organized as follows. Section (6.2) will define the problem we attempt to solve. Section (6.3) will explain our assumed image model and will explain its implications and limitations. Section (6.4) will describe the algorithm. Section (6.5) reports the results we obtained on simulated and actual data. Section (6.6) concludes with a summary.

6.2 Problem Definition

6.2.1 Problem Assumptions

The 2-D discrete blind deconvolution problem is as follows [44]. We observe

$$y(n_1, n_2) = h(n_1, n_2) * *u(n_1, n_2) + n(n_1, n_2) \tag{6.1}$$

where ** represents 2-D convolution.

The 1-D convolution $*$ is defined here as

$$h(n) * u(n) = \sum_{i=0}^{n} h(n-i)u(i) = \sum_{i=0}^{n} h(i)u(n-i) \tag{6.2}$$

We assume the PSF $h(n_1, n_2) = 0$ outside $0 \leq n_1, n_2 \leq L-1$. We do **not** assume that the image $u(n_1, n_2)$ has compact support. The 2-D blind deconvolution problem is to reconstruct the image $u(n_1, n_2)$ (and presumably the PSF $h(n_1, n_2)$) from the known data $y(n_1, n_2)$, hence the term "blind deconvolution." No stochastic assumptions are made about either the image or the point-spread function. This precludes use of methods based on cumulants, ARMA or Poisson image models or stochastic equalization.

To solve the overall 2-D blind deconvolution problem, we partition it into sub-problems. *For each sub-problem*, we make the following assumptions:

1. $u(n_1, n_2) = 0$ outside $0 \leq n_1, n_2 \leq M-1$;

2. $h(n_1, n_2) = 0$ outside $0 \leq n_1, n_2 \leq L-1$;

3. $y(n_1, n_2)$ is known only for $L-1 \leq n_1, n_2 \leq M-1$;

4. $n(n_1, n_2)$ is a zero-mean 2-D white Gaussian noise random field;

5. All quantities are real-valued.

Note the data $y(n_1, n_2)$ are known only for $L-1 \leq n_1, n_2 \leq M-1$. This is the partial data case: no edge information about the image $u(n_1, n_2)$ is used (the "valid" convolution). Hence without loss of generality we may set $u(n_1, n_2) = 0$ outside $0 \leq n_1, n_2 \leq M-1$.

6.2.2 Problem Ambiguities

There are three trivial ambiguities in the 2-D blind deconvolution problem:

1. *Scale factor:* If $\{h(n_1, n_2), u(n_1, n_2)\}$ is a solution, then $\{ch(n_1, n_2), \frac{1}{c}u(n_1, n_2)\}$ is also a solution for any real constant c. If c cannot be determined from the image energy, it usually is irrelevant. We consider the problem to be solved when the image is determined to a scale factor;

2. *Translation:* If $\{h(n_1, n_2), u(n_1, n_2)\}$ is a solution, then $\{h(n_1+d_1, n_2+d_2), u(n_1-d_1, n_2-d_2)\}$ is also a solution for any constants d_1, d_2. We eliminate this ambiguity by specifying the supports above;

3. *Exchange:* We need to be able to distinguish $h(n_1, n_2)$ from $u(n_1, n_2)$. Since we need $M > L$ above, this is not a problem here.

We also assume that the 2-D z-transforms

$$H(x, y) = \sum_{n_1=0}^{L-1} \sum_{n_2=0}^{L-1} h(n_1, n_2) x^{-n_1} y^{-n_2} \tag{6.3a}$$

$$U(x, y) = \sum_{n_1=0}^{M-1} \sum_{n_2=0}^{M-1} u(n_1, n_2) x^{-n_1} y^{-n_2} \tag{6.3b}$$

are irreducible (they cannot be factored) for each subproblem. This is almost surely true [44].

6.3 QUILL Image Model

Sampled images, especially those of large size, tend to be sufficiently lowpass that they can be approximated by an upsampled or expanded version of the image convolved with a basis function such as the Haar basis or the linear spline basis. We shall explain this for the 1-D case.

6.3.1 1-D Image Basis Representation

Consider a discrete 1-D signal $u(n)$. Then, as per our image basis model, we assume it can be written in the form

$$u(n) = \sum_{i=-D}^{D} u(2i)\phi(n-2i) = \tilde{u}(n) * \phi(n) \tag{6.4}$$

where $\phi(n)$ is a basis function of duration $4D+1$ and

$$\tilde{u}(n) = \begin{cases} u(n) & \text{if n is even} \\ 0 & \text{if n is odd} \end{cases} \tag{6.5}$$

$\tilde{u}(n)$ is obtained from $u(n)$ by setting $u(n) = 0$ for odd n. We refer $\tilde{u}(n)$ as the upsampled or expanded version of $u(n)$ (both terms can be found in various DSP textbooks).

6.3.2 Specification of the QUILL model

Quincunx sampling refers to the 1-in-4 sampling pattern in images that results in a checkerboard sampled image [82]. If $u(n_1, n_2)$ is a 2-D image and $\tilde{u}(n_1, n_2)$ is its Quincunx-sampled version, then

$$\tilde{u}(n_1, n_2) = \begin{cases} u(n_1, n_2) & \text{if } n_1 + n_2 \text{ is even} \\ 0 & \text{if } n_1 + n_2 \text{ is odd} \end{cases} \tag{6.6}$$

Consider $\tilde{u}(n_1, n_2)$. If we (2×2) upsample or expand this image along lines inclined at 45 and 135 degrees, we then get an *upsampled or expanded* Quincunx image $\widetilde{u2}(n_1, n_2)$. If $\widetilde{u2}(n_1, n_2)$ is now convolved with a 2-D linear spline basis function also inclined at 45 and 135 degrees, then this approximation to the original image is a Quincunx Upsampled Interpolated Linearly (QUILL) image model.

Define the two basis functions

$$\phi 1(n_1, n_2) = \begin{bmatrix} 0 & 0 & \frac{1}{4} & 0 & 0 \\ 0 & \frac{1}{2} & 0 & \frac{1}{2} & 0 \\ \frac{1}{4} & 0 & 1 & 0 & \frac{1}{4} \\ 0 & \frac{1}{2} & 0 & \frac{1}{2} & 0 \\ 0 & 0 & \frac{1}{4} & 0 & 0 \end{bmatrix} \tag{6.7}$$

and

$$\phi 2(n_1, n_2) = \begin{bmatrix} 0 & \frac{1}{4} & 0 \\ \frac{1}{4} & 1 & \frac{1}{4} \\ 0 & \frac{1}{4} & 0 \end{bmatrix} \tag{6.8}$$

Then the Quincunx-sampled $\tilde{u}(n_1, n_2)$ is

$$\tilde{u}(n_1, n_2) = \widetilde{u2}(n_1, n_2) * *\phi 1(n_1, n_2) \tag{6.9}$$

Note that $\widetilde{u2}(n_1, n_2)$ has 7/8 of its values equal to zero, while $\tilde{u}(n_1, n_2)$ has only half of its values equal to zero.

The QUILL image model $\hat{u}(n_1, n_2)$ of $u(n_1, n_2)$ is

$$\hat{u}(n_1, n_2) = \tilde{u}(n_1, n_2) * *\phi 2(n_1, n_2) \tag{6.10}$$

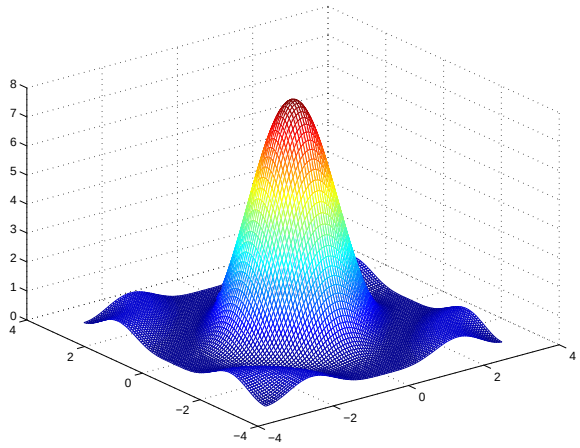

Figure 6.1: Magnitude response of $\phi(n_1, n_2) = \phi 1(n_1, n_2) * *\phi 2(n_1, n_2)$

from the Quincunx-sampled $\tilde{u}(n_1, n_2)$, which becomes

$$\hat{u}(n_1, n_2) = \widetilde{u2}(n_1, n_2) * *(\phi 1(n_1, n_2) * *\phi 2(n_1, n_2)) \tag{6.11}$$

Note that convolution with $\phi 1(n_1, n_2)$ converts the 1-in-8 image $\widetilde{u2}(n_1, n_2)$ into the regular Quincunx-sampled image $\tilde{u}(n_1, n_2)$. Then convolution of this result with $\phi 2(n_1, n_2)$ converts the 1-in-2 Quincunx approximation to a linear spline approximation of the full image. We also remark that $\widetilde{u2}(n_1, n_2)$ is the kernel image. If this is known then the QUILL approximation can be constructed since $\phi 1(n_1, n_2)$ and $\phi 2(n_1, n_2)$ are known.

6.3.3 Examples of the QUILL Model

The QUILL image model works best if the image is roughly low-pass. This is evident from the 2-D Discrete-Space-Fourier-Transforms (DSFT) of $\phi(n_1, n_2) = \phi 1(n_1, n_2) * *\phi 2(n_1, n_2)$ shown in Figure (6.1). The cutoff of this filter is approximately $|\omega| = 2$. This means that the image should have most of its frequency components within this frequency range to minimize model error. This is not unreasonable, since oversampling of images is quite common.

In the spatial domain, we see that using 1-in-8 samples implies that this model is

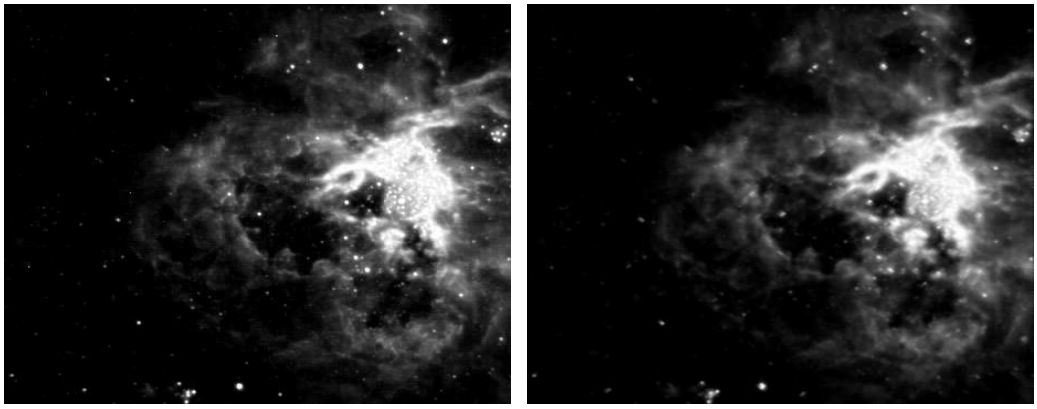

(a) Original Nebula image.

(b) QUILL model of Nebula image. Note poor representation of stars.

Figure 6.2: Sample QUILL model representation of an astronomical image.

not well-suited to astronomical images, where point-like objects are common. However, many natural images and (in particular) light-microscopy-based images are suitable candidates for this model. Furthermore, the more oversampled the image, the better it is modelled by this image model.

Figs. (6.2(a))-(6.4(b)) compare actual images and their QUILL-model approximations. Comparing the "nebula" image Figure (6.2(a)) with its QUILL model Figure (6.2(b)) shows that point-like stars are blurred, although the nebula itself is only slightly blurred.

Comparing the "chief" image Figure (6.3(a)) with its QUILL model Figure (6.3(b)) shows that distinguishing them visually is difficult. Similar comments apply to the onion cell model Figure (6.4(a)) and its QUILL model Figure (6.4(b)).

6.4 Solution to the QUILL Deconvolution Problem

6.4.1 QUILL Image Deconvolution as 4-Channel Deconvolution

Convolution of a QUILL-model image with a PSF is closely related to 4-channel convolution [21, 62, 75, 82, 27]. To show this, we define the complete basis function

$$\phi(n_1, n_2) = \phi 1(n_1, n_2) * *\phi 2(n_1, n_2) \tag{6.12}$$

(a) Original Chief image.

(b) QUILL model of Chief image. Note the model works well visually.

Figure 6.3: Sample QUILL model representation of a natural image.

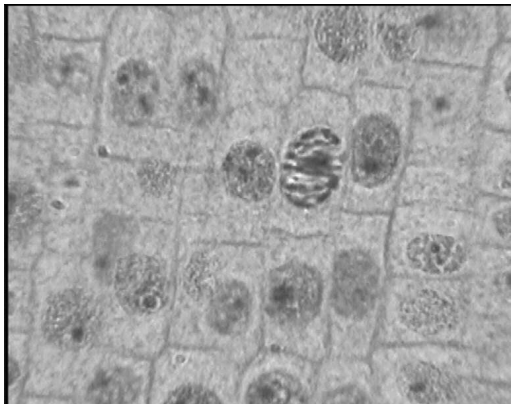

(a) Original Onion Cell image.

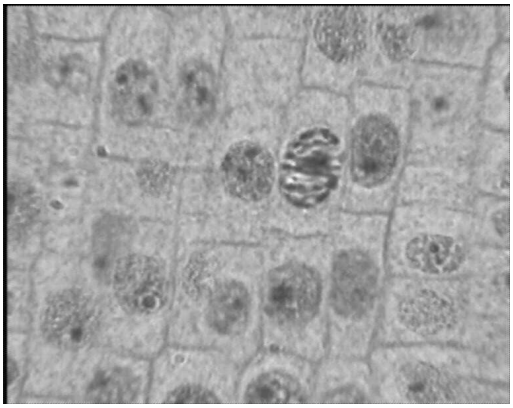

(b) QUILL model of Onion Cell. The model works well visually.

Figure 6.4: Sample QUILL model representation of a optical microscope image.

and the revised PSF

$$\tilde{h}(n_1, n_2) = h(n_1, n_2) * *\phi(n_1, n_2) \tag{6.13}$$

The 2-D blind deconvolution problem for the QUILL image model can be restated as follows. Omitting the noise term (only for the moment) for clarity, the original problem becomes

$$\begin{aligned} y(n_1, n_2) &= h(n_1, n_2) * *u(n_1, n_2) \\ &= h(n_1, n_2) * *(\phi(n_1, n_2) * *\widetilde{u2}(n_1, n_2)) \\ &= \tilde{h}(n_1, n_2) * *\widetilde{u2}(n_1, n_2) \end{aligned} \tag{6.14}$$

If we now define the polyphase components

$$\begin{aligned} y^1(n_1, n_2) &= y(2n_1, 2n_2) \\ y^2(n_1, n_2) &= y(2n_1 + 1, 2n_2) \\ y^3(n_1, n_2) &= y(2n_1, 2n_2 + 1) \\ y^4(n_1, n_2) &= y(2n_1 + 1, 2n_2 + 1) \\ \tilde{h}^1(n_1, n_2) &= \tilde{h}(2n_1, 2n_2) \\ \tilde{h}^2(n_1, n_2) &= \tilde{h}(2n_1 + 1, 2n_2) \\ \tilde{h}^3(n_1, n_2) &= \tilde{h}(2n_1, 2n_2 + 1) \\ \tilde{h}^4(n_1, n_2) &= \tilde{h}(2n_1 + 1, 2n_2 + 1) \end{aligned} \tag{6.15}$$

then we have the following relationships

$$\begin{aligned} y^1(n_1, n_2) &= \tilde{h}^1(n_1, n_2) * *\tilde{u}(n_1, n_2) \\ y^2(n_1, n_2) &= \tilde{h}^2(n_1, n_2) * *\tilde{u}(n_1, n_2) \\ y^3(n_1, n_2) &= \tilde{h}^3(n_1, n_2) * *\tilde{u}(n_1, n_2) \\ y^4(n_1, n_2) &= \tilde{h}^4(n_1, n_2) * *\tilde{u}(n_1, n_2) \end{aligned} \tag{6.16}$$

since the 1-in-8 sampled $\widetilde{u2}(n_1, n_2)$ is effectively convolved with four different PSFs $\tilde{h}^k(n_1, n_2)$, each of which is a (2×2) downsampled version of $\tilde{h}(n_1, n_2)$.

This is evidently a four-channel SIMO (Single Input Multiple Output) system, where $\tilde{u}(n_1, n_2)$ is the input and each of the $\tilde{h}^k(n_1, n_2)$ represents the PSF in a given channel.

6.4.2 2-D Bezout's Lemma

Let $h^k(n_1, n_2)$, k=1,2,3,4 be four linearly independent $(L \times L)$ 2-D functions. Then there exists, almost surely, four (L-1)×(L-1) 2-D functions $g^k(n_1, n_2)$, k=1,2,3,4 such that

$$\sum_{k=1}^{4} h^k(n_1, n_2) * * g^k(n_1, n_2) = \delta(n_1, n_2) \tag{6.17}$$

This lemma has been proved for the general multichannel case in [21]. We shall only outline the proof here so as to provide continuity. We use lexicographic ordering to define the following matrices and vectors. Let

$$h(n_1, n_2) = [h^1(n_1, n_2) \dots h^4(n_1, n_2)]' \tag{6.18}$$

For $l_1 \in [1, L]$, define the $(L^2 \times 4L)$ matrix with (4X1) all-zero vectors 0 such that

$$H_{l_1} \doteq \begin{bmatrix} h'(l_1, 0) & 0' & \dots & 0' \\ h'(l_1, 1) & h'(l_1, 0) & \dots & 0' \\ \vdots & \vdots & \vdots & \vdots \\ h'(l_1, L) & h'(l_1, L-1) & \dots & h'(l_1, 1) \\ 0' & h'(l_1, L) & \dots & h'(l_1, 2) \\ \vdots & \vdots & \cdots & \vdots \\ 0' & 0' & \dots & h'(l_1, L) \end{bmatrix} \tag{6.19}$$

We then define the block Toeplitz matrix H as

$$H = \begin{bmatrix} H_0 & 0 & \dots & 0 \\ H_1 & H_0 & \dots & 0 \\ \vdots & \vdots & \vdots & \vdots \\ H_L & H_{L-1} & \dots & H_1 \\ 0 & H_L & \dots & H_2 \\ \vdots & \vdots & \cdots & \vdots \\ 0 & 0 & \dots & H_L \end{bmatrix} \tag{6.20}$$

If $g_(l_1, l_2)$ is defined as

$$g(l_1, l_2) = [g^1(l_1, l_2) \dots g^4(l_1, l_2)]' \tag{6.21}$$

then (6.17) can be restated as

$$Hg(l_1, l_2) = \delta(l_1, l_2) \tag{6.22}$$

Further, if H has full column rank, then it can be shown that the solution $g(l_1, l_2)$ exists and is unique [21]. H has full column rank when $H_m(z_1, z_2), m = 1 \dots 4$ are strongly coprime and H_0 is full rank [21]. Four 2-D polynomials are almost certainly co-prime, since three or more lines passing through the same point in the (z_1, z_2) plane is an event of measure zero. Moreover, the full-rank requirement of H_0 implies that $H_m(z_1, z_2), m = 1 \dots 4$ polynomials corresponding to the first column of $h_m(0, l_2)$ are co-prime. This is not a stringent requirement, as this is the event of two points coinciding on a line; again this is an event of measure zero.

The bottom line is that a unique set of deconvolvers $g^k(n_1, n_2), k = 1, 2, 3, 4$ almost surely exists such that

$$\sum_{k=1}^{4} \tilde{h}^k(n_1, n_2) * * g^k(n_1, n_2) = \delta(n_1, n_2) \tag{6.23}$$

where we are now using $\tilde{h}^k(n_1, n_2)$ constructed by (2×2) downsampling $\tilde{h}(n_1, n_2) = h(n_1, n_2) * *\phi(n_1, n_2)$.

It may seem as though $\phi(n_1, n_2)$ is a common factor of the $\tilde{h}^k(n_1, n_2)$. But this is not the case, since the $\tilde{h}^k(n_1, n_2)$ are *downsampled* from $\tilde{h}(n_1, n_2)$. A problem will arise only if $\phi(n_1, n_2)$ is an *ideal* low-pass filter; Figure (6.1) shows clearly that this is not the case.

In fact, if $\phi(n_1, n_2)$ is an ideal low-pass filter, another problem will arise with the QUILL model $\hat{u}(n_1, n_2)$ of the image $u(n_1, n_2)$. The QUILL model has an implicit spectral redundancy, since the upsampling or expanding (inserting zeros) makes the high frequency part of the spectrum identical to the low frequency part of the spectrum. The spectrum of the QUILL image model does not show this explicitly, due to convolution with $\phi(n_1, n_2)$, but it is still there implicitly. If $\phi(n_1, n_2)$ were an ideal low-pass filter, this redundancy would be destroyed, and multichannel deconvolution would no longer be possible.

This is implicit in the use of basis functions to parametrize the image–some information is lost. Here, this manifests itself as high frequencies being related to low frequencies, which of course is not true in practice. This is the high-frequency error in using the model.

6.4.3 Overall Approach

Using the 2-D Bezout Lemma, we can solve the blind deconvolution problem as follows:

Convolving each of (6.16) with the corresponding $g^k(n_1, n_2)$ and summing yields

$$\sum_{k=1}^{4} y^k(n_1, n_2) * * g^k(n_1, n_2) = \tag{6.24}$$
$$\sum_{k=1}^{4} \tilde{h}^k(n_1, n_2) * * g^k(n_1, n_2) * * \tilde{u}(n_1, n_2) =$$
$$\tilde{u}(n_1, n_2) * * \sum_{k=1}^{4} \tilde{h}^k(n_1, n_2) * * g^k(n_1, n_2)$$

using the distributive property of convolution. Then (6.23) yields

$$\sum_{k=1}^{4} y^k(n_1, n_2) * * g^k(n_1, n_2) = \tilde{u}(n_1, n_2) \tag{6.25}$$

which is a linear system of equations in the unknowns $g^k(n_1, n_2)$ and $\tilde{u}(n_1, n_2)$. Note that half of the $\tilde{u}(n_1, n_2)$ values are zero, since 7/8 of the $\widetilde{u2}(n_1, n_2)$ values are zero; this is the reason for using the QUILL-type upsampling in the first place, so that the known zero values of $\tilde{u}(n_1, n_2)$ could be used to determine the $g^k(n_1, n_2)$.

Once we know $\tilde{u}(n_1, n_2)$, we compute $\hat{u}(n_1, n_2)$ using (6.10). This is the reconstructed image, which is in the form of a QUILL model.

6.4.4 Implementation of QUILL on Real Data

We have just shown how to obtain $\hat{u}(n_1, n_2)$ from $y(n_1, n_2)$. Practically, the algorithm can be broken down as follows:

1. Obtain $y^k(n_1, n_2), 1 \leq k \leq 4$ using (6.15);

2. Form four Toeplitz-Block-Toeplitz (TBT) matrices Y_1, Y_2, Y_3, Y_4 from each of the $y^k(n_1, n_2)$;

3. Concatenate the TBT matrices to form the matrix $Y = [Y_1|Y_2|Y_3|Y_4]$. Then $Y\vec{g} = \vec{u}$ where:

4. $\vec{g}$ is the stack of the four lexicographically-unwrapped deconvolvers $g^k(n_1, n_2)$;

5. $\vec{u}$ is the lexicographically-unwrapped Quincunx image $\tilde{u}(n_1, n_2)$;

6. Half of the rows of $Y\vec{g} = \vec{u}$ become $Y_1\vec{g} = \vec{0}$, since half of the values of $\tilde{u}(n_1, n_2)$ are zero. These can be used to determine $\vec{g}$;

7. Here Y_1 is the matrix consisting of half of the rows of Y; Y_2 is the matrix containing the remaining rows of Y;

8. $Y_2\vec{g} = \vec{u}$ computes $\tilde{u}(n_1, n_2)$ directly from $g^k(n_1, n_2)$. No deconvolution of $\tilde{h}^k(n_1, n_2)$ from data is needed.

In fact, these two steps can be combined into the single step

$$\begin{bmatrix} Y_1 & 0 \\ Y_2 & -I \end{bmatrix} \begin{bmatrix} \vec{g} \\ \vec{u} \end{bmatrix} = \begin{bmatrix} 0 \\ 0 \end{bmatrix} \tag{6.26}$$

so that the computation consists of computing the null vector of a single matrix, followed by convolutions with the four deconvolvers $g^k(n_1, n_2)$.

6.4.5 Implementation Issues

Several regularization techniques were tried. We discovered that Truncated Singular Value Decomposition [63] worked best on this problem. The reason for this is not clear, but use of regularization techniques in inverse problems is known to be very problem-dependent.

Another issue is selecting the size L of the PSF. Choosing L too small produced ringing artifacts in the image. Choosing L too large produced a nullspace of dimension greater than one. This is not surprising, since translational ambiguity is now present; the actual PSF can "rattle around" inside its assumed $(L \times L)$ support. This too-low rank could be used as a criterion for choosing L: Choose L so that the dimension of the null space is one. In practice, the singular values could be thresholded, so that the smallest is much smaller than the next-smallest. Long tails in the

PSF have a minor effect on the data, which already has some modelling error since the actual image is not modelled perfectly by a QUILL model.

6.4.6 Stochastic Formulation

Until now, we have neglected the additive noise term $n(n_1, n_2)$ in the original problem statement. Recalling that $n(n_1, n_2)$ is a zero-mean white Gaussian noise random field, the effect of the noise will be to render $Y_1\vec{g} = 0$ unsolvable. After adding noise to the data, matrix Y_1 has full rank.

It is easy to show that the log-likelihood function for computing the maximum-likelihood estimates $\hat{\vec{g}}$ and $\hat{\vec{u}}$ from the data $y(n_1, n_2)$ requires that the minimun least-squares perturbation of the data $y(n_1, n_2)$ that makes the matrix in (6.26) drop rank by one.

This suggests the use of a total-least-squares approach to find this minimum data perturbation. However, there are other considerations, including stabilization of the reconstructed image. That is, the problem must be regularized, so that further perturbation of the data does not radically change the reconstructed image. This is discussed above.

We hypothesize that the modelling error in approximating an actual image with the QUILL model can itself be approximated with a zero-mean white Gaussian noise random field. This is because the modelling error tends to be highpass which after 2-D convolution with a generally low-pass PSF (such as a Gaussian PSF) tends to be roughly equalized to a flat spectrum error. This is not an important point as we do not employ any explicit stochastic model.

6.5 Numerical Examples

Many experiments were performed. However, in the interest of brevity, we present only four examples.

- A known "hand" image convolved with a known (but not to the algorithm!) low-pass PSF. The algorithm was applied to the data, and the resulting reconstruction compared to the known original image. This is not trivial, since the image is NOT a QUILL image;
- A known "pentagon" image convolved with a known (but not to the algorithm!) band-reject PSF. The algorithm was applied to the data, and the resulting reconstruction compared to the known original image. This is not trivial, since the image is NOT a QUILL image;
- A blurred "beads and cells" image acquired using a microscope. The algorithm was run directly on the data. The original image is unknown; evaluation is subjective;
- A blurred "Sydney opera house" image acquired using a digital camera. The algorithm was run on the data. The original image is unknown; evaluation is subjective.

6.5.1 Real Images with Synthetic Blurring

Example 1: The 151×151 "hand" image shown in Figure (6.5(a)) image was convolved with an 8X8 Gaussian PSF. The algorithm does not "know" the PSF, except that $L = 8$. Further, the original image was NOT constructed using the QUILL model; an actual image was used. The purpose of this simulation is to test the effect of the modelling error.

(a) Original "hand" image.

(b) "Hand" image blurred with a 8X8 Gaussian PSF with $\sigma = 4$.

(c) Deblurred "hand" image.

Figure 6.5: Deconvolution of an image that was not constructed from the QUILL model.

The reconstructed image is shown in Figure (6.5(c)). The example demonstrates a fundamental limitation of the algorithm; the loss of high frequency information during deconvolution. However, the reconstruction is significantly better (by visual inspection) than the blurred image.

The reader should note that the original image has black spots in the ring (perhaps due to a scanning error). As expected, these are not well deblurred in the reconstruction. This is because QUILL does not represent point-like features well. However, other details in the image are recovered.

Example 2:The 500×500 "Pentagon" image in Figure (6.6(a)) was convolved with a PSF having the spectrum shown in Figure (6.6(b)). The PSF was unknown

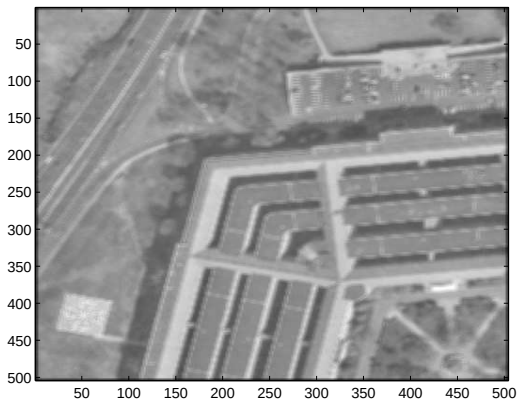

(a) "Pentagon" image blurred with unknown PSF.

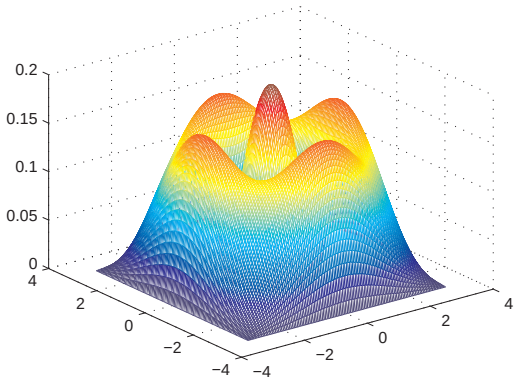

(b) (Unknown) spectrum of PSF.

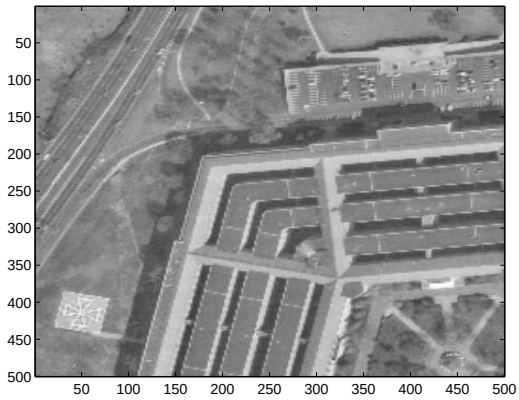

(c) Deblurred "Pentagon" image.

Figure 6.6: Deconvolution of an image that was convolved with a bandpass PSF.

to the algorithm. The purpose of this example was to test the performance of the algorithm on a non-low-pass PSF (colleagues asked about this).

The reconstructed image is shown in Figure (6.6(c)). Significant details can be observed in the reconstructed image that are not apparent in the blurred image (e.g., the cars).

6.5.2 Real Data

In these two examples the algorithm is applied directly on real data acquired using a microscope and digital camera.

Example 3: Figure (6.7(a)) is a blurred image of beads and cells acquired from a Zeiss Axiovert S100 microscope. The algorithm was run directly on this real-world

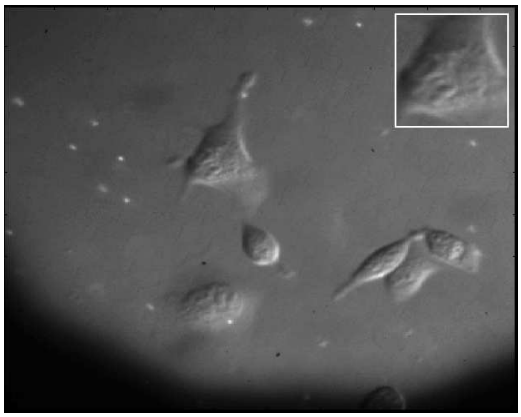

(a) Image of fluorescent beads and cells.

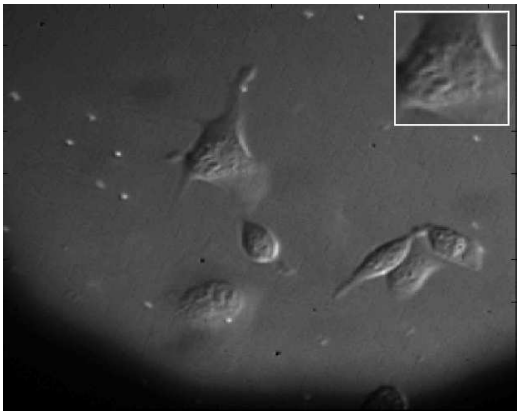

(b) Deconvolved beads and cells image.

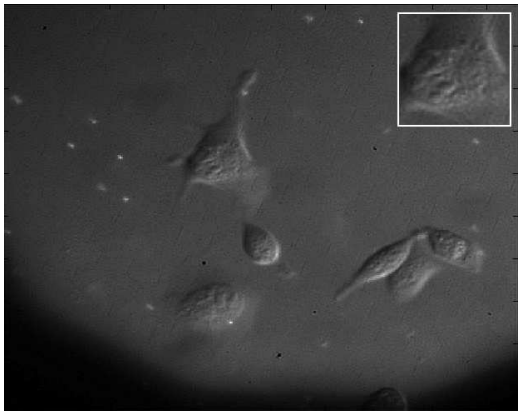

(c) Deconvolved image of beads and cells using Lucy-Richardson.

Figure 6.7: Blind deconvolution of an image obtained from an optical microscope.

data; this is truly blind deconvolution.

Figure (6.7(b)) is the deconvolved image. One can observe more structures in the deconvolved image. One of the cells has been zoomed to demonstrate the improvement; note several features are apparent in the deblurred image that were not apparent in the original data. Since the "true" image is unknown, objective evaluation of these results is impossible, but visually there seems to be improvement.

We also compared our algorithm to the iterative Lucy-Richardson algorithm. Lucy-Richardson (LR) has four disadvantages compared to our algorithm:

- LR requires deconvolution at each step; this is computationally intensive compared to our algorithm, which never requires deconvolution since it computes

deconvolvers;

- LR is iterative, and it can take a long time to converge;
- LR may not converge at all, even to an incorrect answer;
- LR requires initial guesses for the image and the PSF.

To be fair, we used a truncated Gaussian of the same size as the actual PSF as an initial guess. LR required much more computation than our algorithm, since convergence was slow.

The reconstructed image using LR is shown in Figure (6.7(c)). Visually, the results of our algorithm seem to be better than those from LR. Note the ringing artifacts and the graininess in the zoomed insert in the reconstructed-using-LR image.

Example 4: Figure (6.8(a)) is a blurred image of the Sydney Opera house taken using a 3 Megapixel digital camera. The 939×939 image suffers from blurring, due to focus and motion. The algorithm was run directly on this real data.

Figure (6.8(b)) is the deconvolved image. It has an improved perceptual quality to it. Note that the windows and roof top patterns are more visible in the restored image. We have zoomed the windows in the inset in both of the images to illustrate this. The original images are in color and the results are more impressive.

6.6 Conclusion

We have proposed using the QUILL model in conjunction with Bezout's lemma for blind deconvolution from partial data (no image edge effects are used). The method reconstructs finite deconvolvers and thus avoids estimating the PSF and deconvolving it. This results in a blind deconvolution method that is fast and well-suited for deblurring oversampled images.

(a) Blurred image of Sydney opera house.

(b) Deconvolved image of Sydney opera house. Note sharper image of windows and roof.

Figure 6.8: Blind deconvolution of an image shot from a 3 Megapixel camera.

Our analysis and simulations have shown that:

- The QUILL representation is a reasonably accurate model for many sampled natural images;
- The algorithm, while best suited to oversampled images, still improves the image quality for many blurred images;
- The algorithm is much faster than the Lucy-Richardson algorithm, and does not require accurate initial guesses for either the image or the PSF.

The use of an image model is necessary for the single-blur partial data problem. The QUILL model seems to model real-world images well, and permits a fast non-iterative algorithm that does not require estimating the PSF and then deconvolving it from the data, but estimates a deconvolver which filters the data directly. As with any model, some error is introduced and some information is lost; "All models are wrong, but some models are useful." This model seems to be useful.

Some issues that require further work are as follows:

- Further study of regularization methods for computing a well-conditioned null

vector from the data matrix. This means that the null vector (which includes $\tilde{u}(n_1, n_2)$) is not sensitive to data perturbations;

- Development of algorithms for perturbing data to create a 1-D null space for the specific case of Poisson noise;

- Further study of proper choice of the PSF size L. Although this does not seem to be a major issue in practice, it would be nice to have a model-order-selection-type stochastic procedure.

CHAPTER VII

Contrast Transfer Function estimation for cryo and cryo-tomo electron microscopy images

7.1 Introduction

Cryo-electron microscopy (EM) is an important tool for visualizing the structure of molecular assemblies and sub-cellular structure allowing delicate biological samples to be preserved in their native states. Unfortunately, cryo samples are extremely sensitive to radiation damage and thus must be imaged at very low electron doses, resulting in low contrast images having poor signal to noise ratios. This problem is exacerbated in cryo-EM tomography, where the maximum allowable dose must be spread over the 100-200 tilted images usually recorded from a single specimen.

Since thin biological samples are weak phase objects, contrast is generated via a combination of spherical aberration and defocusing. Unfortunately, this introduces significant distortions in the image [67], which along with other factors such as specimen drift and the non-ideal response characteristics of the detection media ultimately limit the maximum useful resolution of the electron micrograph. Accurately correcting image aberrations is important to maximize the obtainable resolution [57, 34, 52, 64]. For thin biological specimens, the characteristic response of the EM system is expressed by the contrast transfer function (CTF), which describes the fidelity with which spatial information is transferred from input to output across a

range of spatial frequencies. Due to the image formation process and non-idealities of the imaging system, the CTF power spectrum of a typical EM system has characteristic oscillatory rings known as Thon rings [78] as seen in Figure 7.1.

While the analytical form of the CTF is well known [15], its estimation from cryo-EM data is challenging due to the low dose of electrons that can be tolerated when imaging unstained biological specimens. This results in an extremely noisy CTF power spectrum. The problem is compounded by inelastic scatter which appears in the Fourier spectrum of the image as background signal that overwhelms the signal of interest. Moreover, due to temporal and spatial incoherence of the electron beam [67], only low frequency CTF information is available for CTF estimation.

Current CTF estimation algorithms suffer from several drawbacks. First, many algorithms simplify the problem by radially averaging the power spectrum of the CTF, which is the same as assuming that no astigmatism is present in the imaging system. Second, almost all algorithms are unable to directly estimate the CTF of protein samples embedded in ice when the SNR of the image is very low [34, 16, 52]. Third, all but one of these algorithms [52] require significant user input and a good starting guess to estimate the CTF parameters. Lastly, no current algorithm can perform CTF estimation on EM tomographic data where the CTF changes across the image plane [86].

In this chapter, we describe a fully automatic CTF estimation algorithm that uses a two dimensional approach to solve the CTF estimation problem. We first review the EM phase contrast image formation process and the theoretical form of the CTF for planar and tomographic EM images. Next, we explain our algorithm and the rationale for each step. We demonstrate the robustness of the algorithm by estimating the CTF of cryo-EM samples backed by carbon film and the more

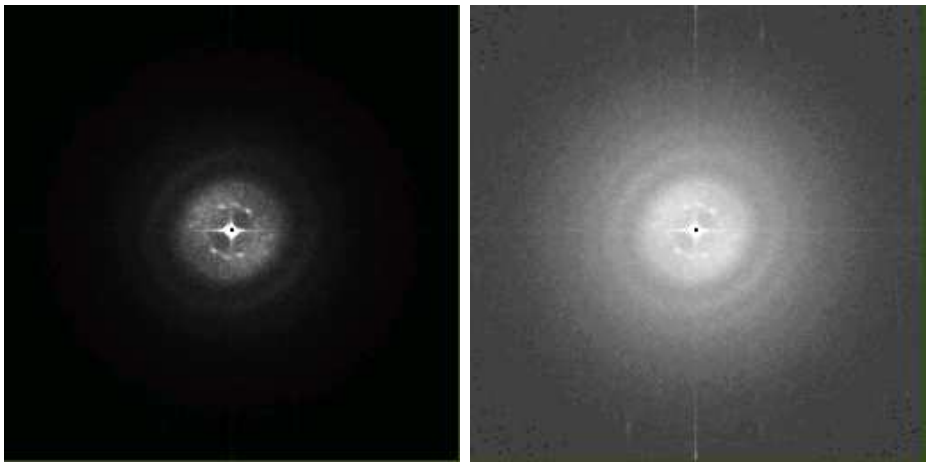

(a) (b)

Figure 7.1: A representative CTF power spectrum estimated from carbon film backed cryo-EM data in (a) linear contrast and (b) logarithmic contrast stretch where the Thon rings are clearer. The elliptical shape is a result of astigmatism.

difficult problem of estimating the CTF of protein samples on ice in regions without a carbon support film. Finally, we also demonstrate the efficacy of the algorithm in estimating the defocus parameters of cryo-tomographic data.

7.2 Theory of Image formation

The formation of contrast in an EM image is primarily due to sample induced elastic and inelastic scattering. Inelastically scattered electrons are responsible for the formation of an almost featureless background in the power spectrum of the image that gradually decays with increasing frequency. Elastically scattered electrons produce image contrast; low angle scattered electrons produce phase contrast whereas high angle scattered electrons produce amplitude contrast. In the next section, we briefly study the theory of EM image formation for biological specimens.

7.2.1 Mathematical Description of Image Formation

In absence of inelastic scatter, the image formation process can be described by a linear theory of contrast transfer [67, 79] as:

$$i(r,\theta) = h(r,\theta) \otimes o(r,\theta) \otimes e(r,\theta) + n \tag{7.1}$$

where i,h and o are the image, transfer function of the system and object respectively and r, θ are polar co-ordinates. The $\otimes$ operator describes the convolution operation. The envelope function $e(r,\theta)$ describes the reduction in image contrast with increasing spatial frequency due to the coherence of the electron beam, lens current instability, stage drift and modulation transfer function (MTF) of the recording media [67]. We assume the noise in the system, n, is a combination of Poisson noise due to photodetection and Gaussian noise, e.g., due to detector or scanner electronics. We approximate both by using a mixed Gaussian noise model as described in [46, 31].

Applying the Fourier transform to (7.1):

$$I(q,\phi) = CTF(q,\phi)O(q,\phi)E(q,\phi) + N \tag{7.2}$$

where q is the spatial frequency, ϕ is the angle ordinate and $CTF(q,\phi)$ is the Fourier transform of $h(r,\theta)$ or contrast transfer function (CTF) of the system.

In biological samples, inelastic scattering contributes significantly to the image formation process [58]. This is seen in the *power spectrum* of the image as an additive low frequency background, $S(q,\phi)$:

$$I^2(q,\phi) = S(q,\phi) + CTF^2(q,\phi)O^2(q,\phi)E^2(q,\phi) + N^2 \tag{7.3}$$

7.3 CTF Formula

7.3.1 Planar EM

For thin biological specimens assuming a weak amplitude-weak phase approximation [67, 58, 84], the theoretical form of the CTF can be expressed as:

$$CTF(q,\phi) = \sqrt{1-\alpha^2}\sin\chi(q,\phi) - \alpha\cos\chi(q,\phi) \tag{7.4}$$

where α is an amplitude contrast factor ($0 \leq \alpha \leq 1$) and $\chi(q,\phi)$ is the scattering angle dependent path length difference of the wavefront of the electron beam [67]. χ can be expressed as:

$$\chi(q,\phi) = \pi/2\{C_s\lambda^3 q^4 - \lambda q^2(2\Delta f_{mean} + \Delta f_{diff} cos(2\phi - 2\phi_A))\} \tag{7.5}$$

where C_s is the spherical aberration of the objective lens, Δf_{mean} is a mean defocus parameter, Δf_{diff} and ϕ_A are parameters describing the astigmatism of the CTF and λ is the wavelength of the electron beam.

7.3.2 Tomographic EM

In EM tomography, images are formed as projections of a sample tilted incrementally with respect to a horizontal plane. The mean defocus is no longer uniform across the sample plane but is dependent on the point of measurement and the tilt angle. Apart from this difference, the theoretical form of the tomographic CTF is identical to (7.4). As shown in the Appendix, for a specimen rotated by an angle θ_{tilt} and whose the rotation axis makes an angle θ_{rot} with respect to the y axis, the mean defocus, Δf_{mean} is related to θ_{tilt} and θ_{rot} at a point $U(x,y,z)$ on the sample plane by the equation

$$\Delta f_{mean} = (x\cos\theta_{rot} + y\sin\theta_{rot})\tan\theta_{tilt} + \Delta f_o \tag{7.6}$$

where $x\cos\theta_{rot} + y\sin\theta_{rot}$ is the projection of the distance between $U(x,y,z)$ on the sample plane and the rotation axis on the zero-tilt plane.

The tilt angle can be estimated by measuring the mean defocus at any two points on the sample plane. If the mean defoci for two points (x_1, y_1, z_1) and (x_2, y_2, z_2) on the sample plane are $\Delta f_{x_1,y_1,z_1}$ and $\Delta f_{x_2,y_2,z_2}$ respectively , the tilt angle θ_{tilt} can be determined as $\theta_{tilt} = \tan^{-1}((\Delta f_{x_1,y_1,z_1} - \Delta f_{x_2,y_2,z_2})/((x_1 - x_2)\cos\theta_{rot} + (y_1 - y_2)\sin\theta_{rot}))$.

7.4 Algorithm for CTF Estimation

A description of the CTF requires knowledge of the parameters described in (7.4). Of these, the spherical aberration term C_s is provided by the microscope manufacturer and the wavelength λ is a known function of accelerating voltage [67]. That leaves the terms Δf_{mean}, Δf_{diff}, ϕ_A and the amplitude contrast factor, α to be determined.

Our CTF estimation algorithm first approximates the CTF power spectrum using an approach similar to periodogram averaging [16]. A residual power spectrum $I^2_{res}(q, \phi)$ is computed by estimating and subtracting the background term $S(q)$ from the CTF power spectrum. The lowest and the highest frequencies are then masked in $I^2_{res}(q, \phi)$ in which the power spectrum of the object (also known as "structure factor") and noise respectively dominate. Finally, the algorithm estimates the CTF parameters from the residual power spectrum using a combination of coarse grid search and a constrained conjugate gradients (CCG) scheme. The one parameter that does need to be estimated by the user is the amount of amplitude contrast, α.

7.4.1 Obtaining the Power Spectrum of the CTF

In cryo-EM, the CTF power spectrum is usually approximated by calculating the power spectrum of a small blank region where there is a carbon support film. As seen in (7.3), the power spectrum of the image $I^2(q, \phi)$, contains a strong noise term,

N^2, that dominates the CTF power spectrum.

To supress noise, an average power spectrum was calculated over 50 random areas of the micrograph similar to periodogram averaging [16]. Averaging over random areas also helps to suppress the contributions from specimen structure when determining the CTF over the sample region. The success of this scheme depends on one of the following assumptions: (1) only a few sampling areas contain the specimen so that the contribution of the sample structure factor in the estimate is small, or (2) the structure factor over the random areas is sufficiently incoherent to be averaged out. In practice, we have found these assumptions to be quite valid. The power spectrum equation (7.3), averaged over these random image samples can then be written as:

$$\langle I^2(q,\phi)\rangle = S(q,\phi) + c_1 CTF^2(q,\phi)E^2(q,\phi) + k \tag{7.7}$$

where c_1 and k are constants. We will refer to this mean power spectrum as the *CTF power spectrum*. Representative CTF power spectra obtained under 4 common imaging conditions are shown in Figure 7.2.

7.4.2 Background Fitting and Subtraction

Since the background $S(q,\phi)$ dominates the CTF power spectrum $\langle I^2(q,\phi)\rangle$, its removal makes the parameter estimation step more reliable. While the background power spectrum is a two-dimensional function, its estimation in a 2D parametric form is problematic due to the low signal to noise ratio (SNR) of cryo-EM images. It is important to note that because of sample structure, drift, tilt, etc., the anisotropy in the background need not match the anisotropy in the CTF caused by astigmatism. Thus it is important to independently determine the radial asymmetry of the

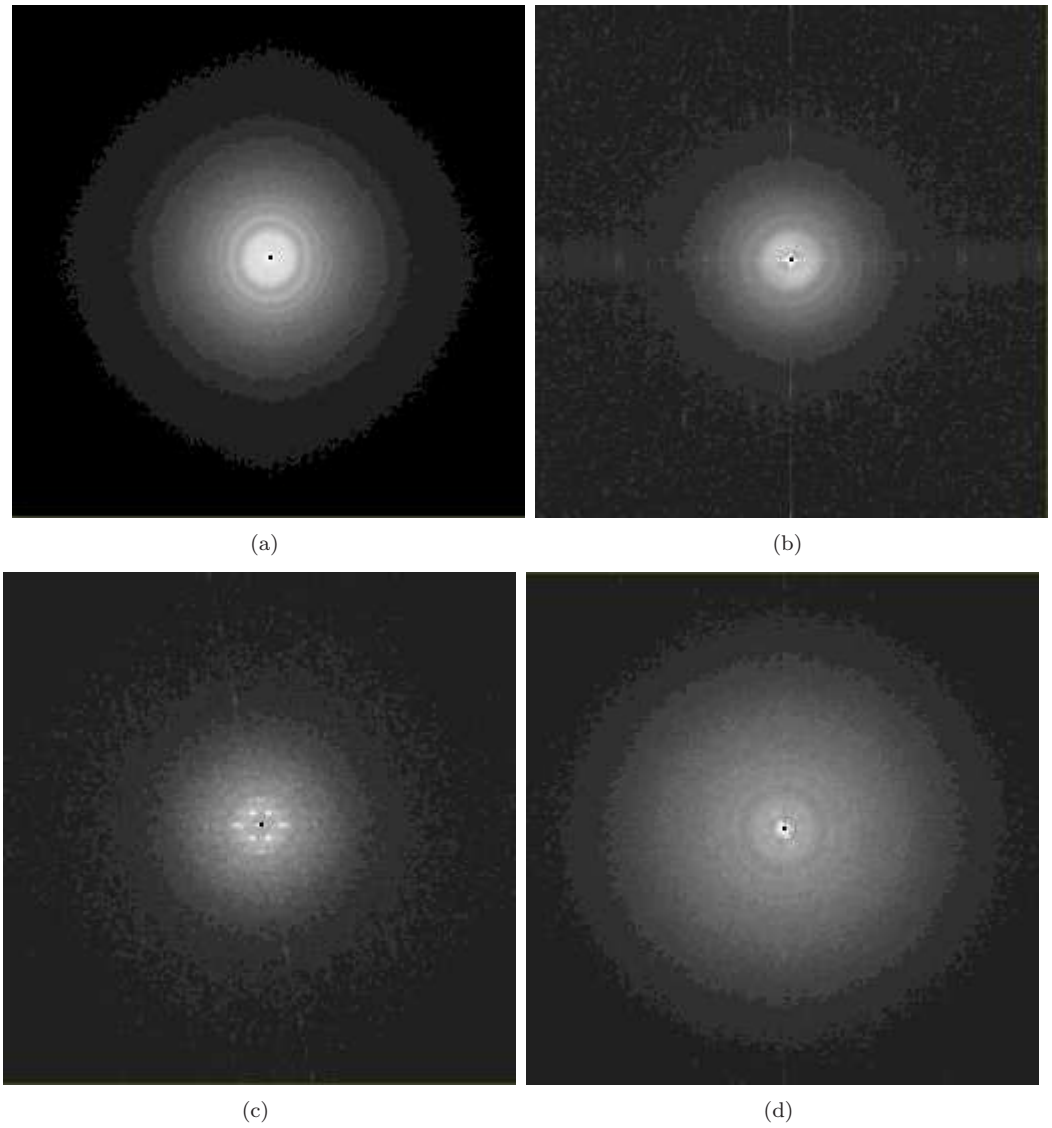

(a) (b)

(c) (d)

Figure 7.2: Examples of averaged CTF power spectra in logarithmic scale, obtained after sampling at 50 random points in the micrograph. Figure 7.2(a) is a representative CTF obtained from a negative stained image. Due to the high SNR, Thon rings are clearly visibile. Figure 7.2(b) is the CTF power spectrum obtained from a cryo sample with carbon support film. Despite a lower SNR the first three Thon rings are still visible. Figure 7.2(c) depicts a CTF power spectrum obtained from a sample of bacteria flagella filament in ice. Due to the absence of carbon support film the CTF is barely visible. The Fourier transform of the specimen is also observed as lines in the power spectrum.[91] Figure 7.2(d) shows a representative power spectrum from a cryo-EM tomograph. Due to the very low electron dose, the SNR of the CTF power spectrum is very low and the Thon rings are barely seen.

background. As a compromise between SNR and accounting for these effects, we estimate the background by dividing $\langle I^2(q,\phi)\rangle$ into 8 sectors and fitting a quartic polynomial to the sector averages.

The resultant background $S(q,\phi)$ is subtracted from $\langle I^2(q,\phi)\rangle$ to form a residual power spectrum, $P(q,\phi)$.

$$P(q,\phi) = \langle I^2(q,\phi)\rangle - S(q,\phi) = c_1 CTF^2(q,\phi)E^2(q,\phi) + k \tag{7.8}$$

7.4.3 Masking

The CTF power spectrum is dominated by the sample structure factor at low frequencies and by noise at high frequencies. Masking out frequencies at these extremes from the residual power spectrum improves the reliability of the CTF parameter estimation.

For the higher frequency cutoff, we use what is known as the predominant power frequency [34]. This is defined as the frequency below which 99 percent of the signal energy is present in the residual CTF. The lower frequency cutoff is chosen within the first CTF ring. The location is not critical and is easily estimated from the approximate defocus parameters obtained in the initial coarse grid search as described in the next section. The masked CTF power spectrum, $P_m(q,\phi)$ is given by:

$$P_m(q,\phi) = P(q,\phi)M(q,\phi) \tag{7.9}$$

where $M(q,\phi)$ is the mask.

7.4.4 Determination of Defocus and Astigmatism Parameters

CTF defocus parameters are estimated using $I^2_{res,m}(q,\phi)$. The parameter estimation problem is solved by a cost function minimization using a robust constrained

conjugate gradients approach (CCG) [23]. We chose the following cross correlation function as our cost function as it has been shown to be an effective measure in CTF parameter estimation [57]:

$$\psi = 1 - \frac{\Sigma_{x,y} P_m * CTF^2}{\sqrt{(\Sigma_{x,y} CTF^4)(\Sigma_{x,y} P_m^2))}} \tag{7.10}$$

Directly using the entire two dimensional data in the cost function maximizes the use of the experimental data and minimizes the need for ad hoc pre-processing. The non-convexity of the CTF parameter optimization surface gives rise to several local minima many of which are eliminated by providing a good starting guess. This step is automated in our algorithm by performing a 256 point grid search across the optimization plane keeping the amplitude contrast parameter (α) constant. To expedite the algorithm, we use the following optimization constraints:

$$0.5\mu m \leq \Delta f_{mean} \leq 15\mu m \tag{7.11}$$

$$0\mu m \leq \Delta f_{diff} \leq 6\mu m \tag{7.12}$$

$$0 \leq \phi_A \leq \pi \tag{7.13}$$

These constraints which are appropriate for the CTFs observed in our datasets, can be readily modified to suit individual needs.

In practice, the amplitude contrast parameter, α, is quite difficult to estimate accurately, and in other programs is a user supplied parameter typically around 7% for cryo images and 15% for negative stain [79]. In our software, this is one term that needs to be provided by the user.

7.4.5 CTF estimation for Tomographic Micrographs

Cryo-EM tomography, especially when coupled with averaging, has now progressed to the point where CTF correction of tilted images is becoming useful. Similarly, determining and correcting the CTF on tilted images could be equally beneficial when using the Random Conical Tilt method [66]. In either case, the first step is the accurate determination of appropriate CTF parameters across the tilted image. Apart from astigmatism and amplitude contrast parameters, the CTF of a tomographic image is completely described when the tilt angle and mean defocus at a given point on the specimen plane are specified. For tomographic CTF estimation, the planar EM algorithm was modified to account for a variable mean defocus and tilt angle.

A schematic of the CTF estimation algorithm for tomographic EM data is shown in Figure 7.3. The algorithm approximates the CTF power spectrum and estimates CTF parameters in 6 areas that are parallel to the tilt axis (we refer to these areas as stripes). The CTF parameter estimates of each stripe are assumed to correspond to the CTF at the centroid of the stripes. The astigmatism of the CTF is assumed to be constant over the specimen plane and independent of the tilt angle, θ_{tilt}. It is estimated by calculating the mean Δf_{diff} and ϕ_a estimates over all the stripes for the tilted sample. From (7.6), the mean defocus estimates of each stripe (Δf_{mean}) should lie on a line with slope $\tan\theta_{tilt}$. The mean defocus at the rotation axis, Δf_o is given by the y-intercept of the fitted line and tilt angle, $\tan\theta_{tilt}$ by the slope. In practice, for cryo EM images, the tilt angle estimates of the algorithm are not as accurate as the nominal tilt angles of the microscope. As a result, the program performs two least squares fits to improve the accuracy of the mean defocus parameter. Δf_o is estimated as the y-intercept of a least squares fit using the tangent of the nominal

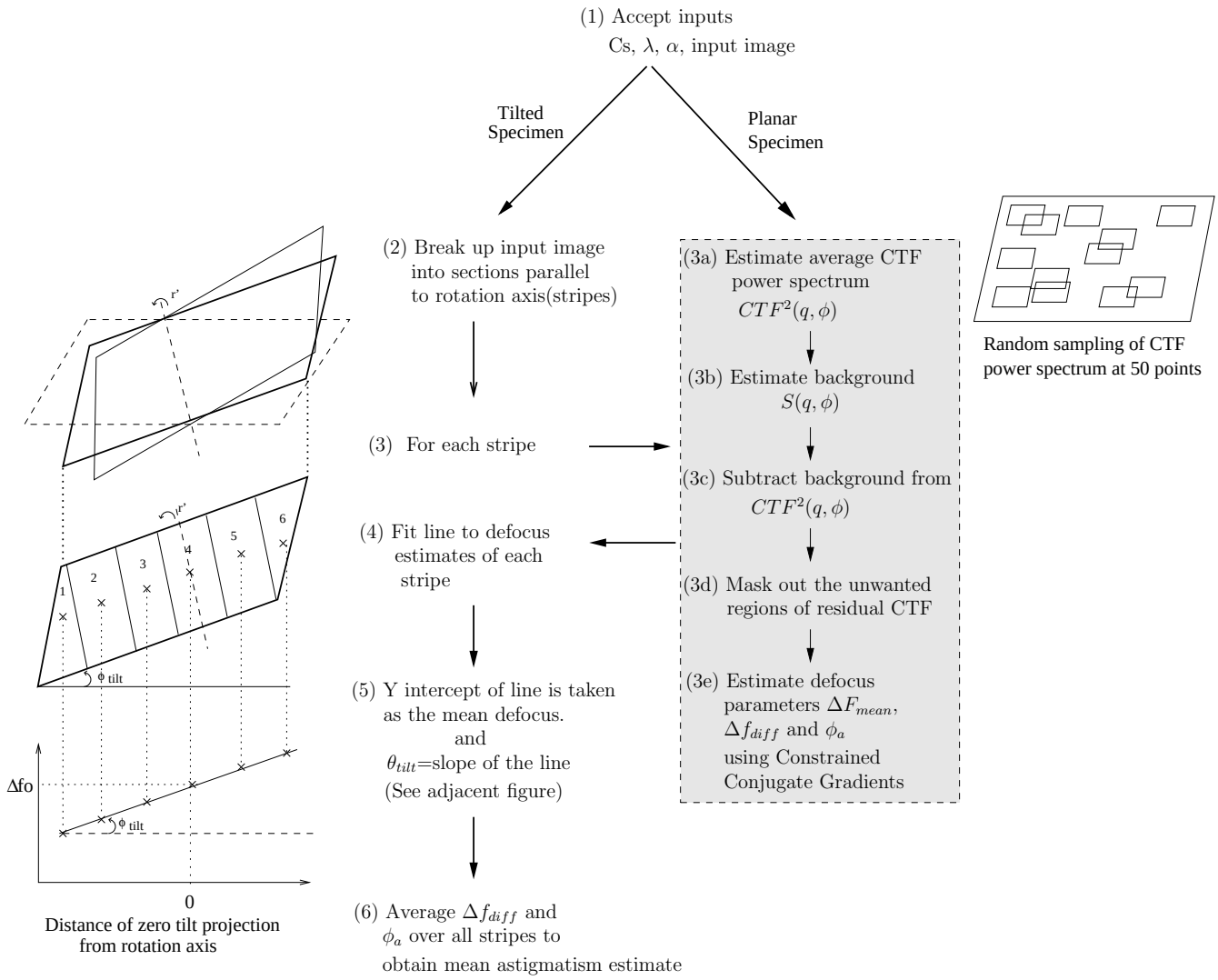

Figure 7.3: Flowchart of defocus parameter estimation algorithm for planar and tilted samples.

tilt angle as the slope of the fit line. θ_{tilt} is estimated as the slope of the fit line in a second least squares fit where no nominal tilt angle information is provided.

We note that the CTFs of each stripe can be expressed as a function of the distance of its centroid from the rotation axis on the zero tilt plane, Δf_o and θ_{tilt}. Δf_o and astigmatism parameters can then be estimated by optimizing a cost function that is the sum of correlation cost functions for each stripe. In this case, the tilt angle will have to be supplied by the user.

7.5 Results

7.5.1 Ice on Carbon Film Defocus Series Data

To evaluate the effectiveness of the algorithm in measuring defocus parameters of cryo-EM data , the nominal defocus was compared to the estimated mean defocus, Δf_{mean}, over a range of defoci. Comparing the relative differences between nominal defocus and Δf_{mean} is a better measure of accuracy than comparing their absolute values due to inherent offset error in the nominal defocus [52].

The nominal defocus of the microscope was changed manually from 1.44 μm to 8 μm in increments keeping astigmatism constant. Defocus was estimated using the algorithm for a series of micrographs imaged at a magnification of 61,000 with a dose of 5 electrons per $\mathring{A}^2$. Fig. 7.4 shows a plot of measured defocus versus nominal defocus. The correlation coefficient of the points with the least squares fit line is 0.999 indicating that the measured defocus accuracy is quite good. The offset error of the nominal defocus is 0.099 μm as indicated by the x-intercept of the line.

7.5.2 Validation of Determined Defocus Values

Tani [77] and Mullick [52] have developed programs that have been shown to estimate CTFs of cryo-EM data with carbon support film quite accurately. Tani's program, PLTCTFX, approximates the CTF power spectrum by calculating the power spectrum of a manually selected region of the micrograph. CTF parameters are estimated by one dimensional parameter fitting on 5 sector averages of the CTF power spectrum. Mullick's program, Automatic CTF Estimation (ACE), uses a different approach. The first CTF ring is detected using two-dimensional edge-detection to determine astigmatism. Defocus parameters are determined by one dimensional fitting of the elliptically averaged CTF. A key difference between our algorithm and

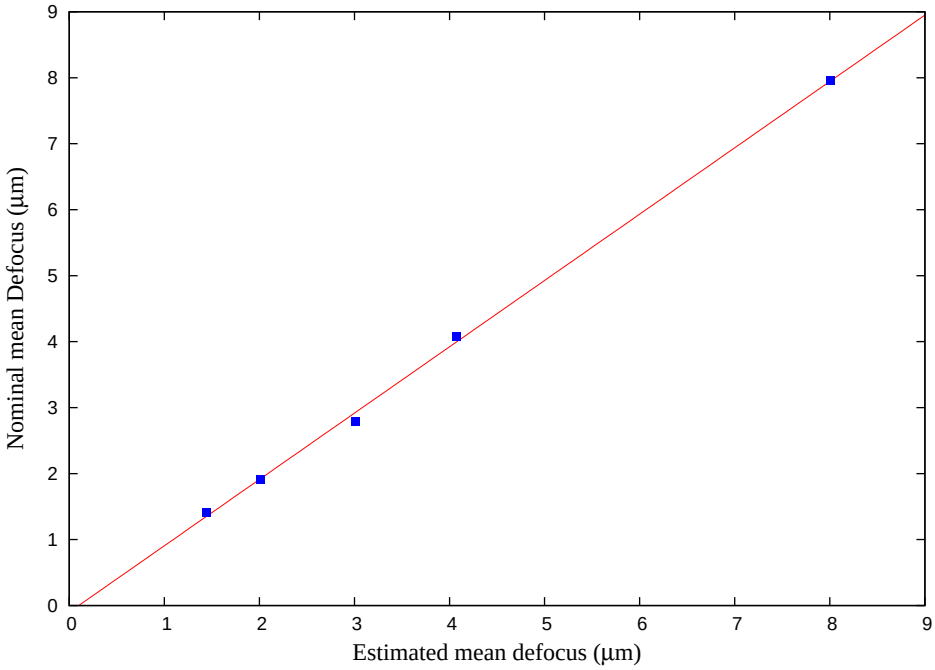

Figure 7.4: Measured defocus vs. Nominal defocus for carbon film EM data. The zero defocus offset of the nominal defocus is 0.099 μm and is represented by the y-intercept of the least squares fit. The slope of the line is 1.005 and the correlation coefficient of the points with the least squares fit is 0.999 indicating that the quality of the fit is very good.

both these algorithms is that we perform parameter estimation in two dimensions unlike the partially two dimensional approach of PLTCTFX and the one dimensional approach of ACE.

We compared the CTF parameter estimates of our algorithm with PLTCTFX and ACE for five carbon film backed samples imaged at a magnification of 86,000 and a dose of 10 electrons per $\mathring{A}^2$ and repeated the estimation 10 times to test the consistency of our algorithm. A different set of 50 random points was used for each of the 10 measurements. The results are presented in Figure 7.5. The mean defocus estimates of our algorithm are within 10% while the astigmatism estimates are with 15% of PLTCTFX and ACE. We observed less agreement in the astigmatism estimates of our algorithm with corresponding PLTCTFX and ACE estimates than when comparing the mean defocus estimates due to the different approaches used by these algorithms to treat astigmatism. The standard deviation of the mean defocus estimate Δf_{mean} was less than 2% of the mean indicating very high consistency in the estimates. The Δf_{diff} estimate varied less than 6% and ϕ_a varied by less than 13° from their respective means. The close agreement in the estimates of our algorithm with PLTCTFX and ACE and the low variation of CTF parameter estimates over 10 iterations indicate that our algorithm is accurate and consistent.

7.5.3 Defocus Estimation of Protein in Ice

Macromolecular complexes are most often imaged in ice without a carbon support film. Since the SNR of the CTF power spectrum is very low in the absence of carbon film, the CTF in these cases is generally approximated from neighboring carbon film containing areas.[52] Local variations in the properties of the specimen and in the thickness of ice can lead to different CTFs in carbon and protein regions making CTF parameter estimates inaccurate. Recent CTF estimation algorithms have attempted

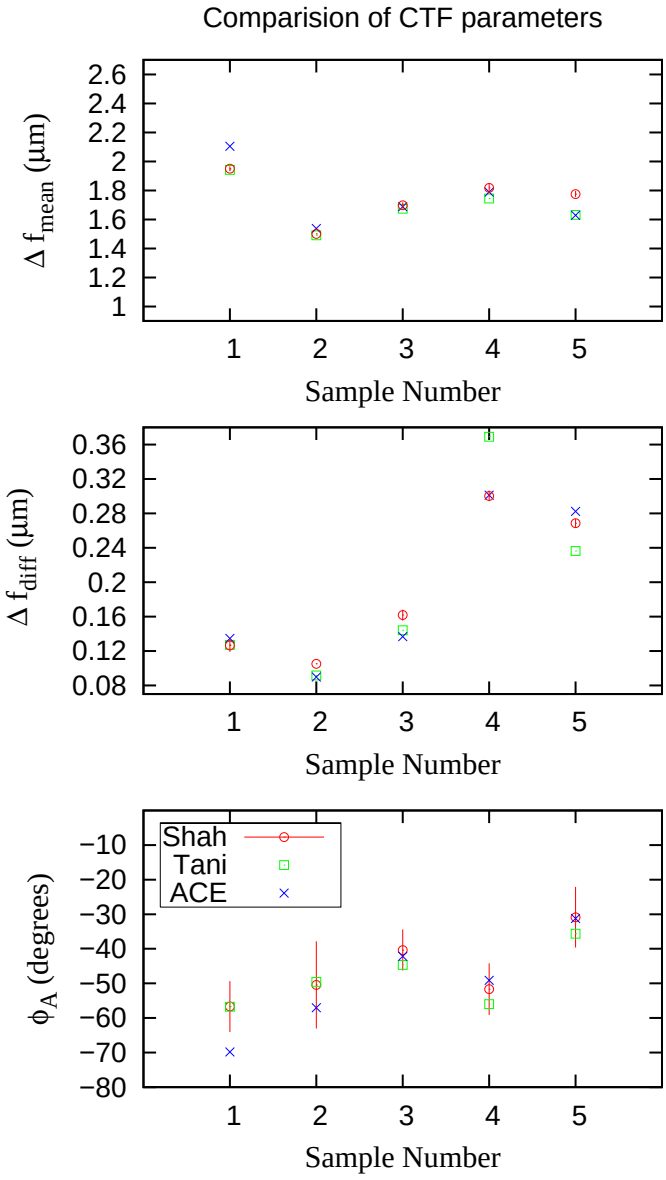

Figure 7.5: Comparision of defocus parameters obtained from 10 measurements our algorithm with PLTCTFX [77] and ACE [52]. The graphs (from top to bottom) compare the estimates obtained for Δf_{mean}, Δf_{diff} and ϕ_A. The standard deviation of our estimates are represented by the error bars.

to solve this problem with varying degrees of success by directly estimating CTF parameters of a cryo-sample without a carbon support film [57, 52]. In these cases, it is the sample itself that provides the necessary signal for CTF determination.

We estimated the CTF parameters of 10 samples of bacteria flagella filaments in ice. As seen in Figure 7.6, the mean defocus (Δf_{mean}) estimates obtained were within $1200\mathring{A}$ to those obtained from carbon film regions of the same sample. The CTF estimation process was repeated 10 times for each sample. The standard deviation of Δf_{mean} was within 2% of the mean indicating that the estimates were very consistent.

By constrast, the astigmatism estimates were neither consistent nor reliable. Δf_{diff} estimates differed by up to 60% of the carbon film values and the standard deviation was as high as 70% of the carbon film estimate. For some samples, ϕ_a estimates were observed to differ by over a 100% compared to the carbon film estimate. Thus, adjacent carbon areas should be used to determine the astigmatism parameters with only the Δf_{mean} estimated from the sample itself.

7.6 Estimation of CTF for Tilted and Tomographic Data

We performed three experiments to demonstrate the performance of the algorithm in determining the CTF parameters for tilted micrographs. In the first experiment, CTF parameters were estimated for several image samples of negatively stained conical tilt data. This is a relatively simple problem as the SNR of the images obtained by negative staining is much higher than that obtained for cryo-EM data [15, 95]. In the second experiment, CTF parameters were estimated for a cryo-EM defocus series dataset for image samples tilted nominally to $-45°$. In the third experiment, the CTF was estimated for 4 tomographic cryo-EM data stacks where the specimens were rotated through a series of tilts from -60° to +60° and their projections at each

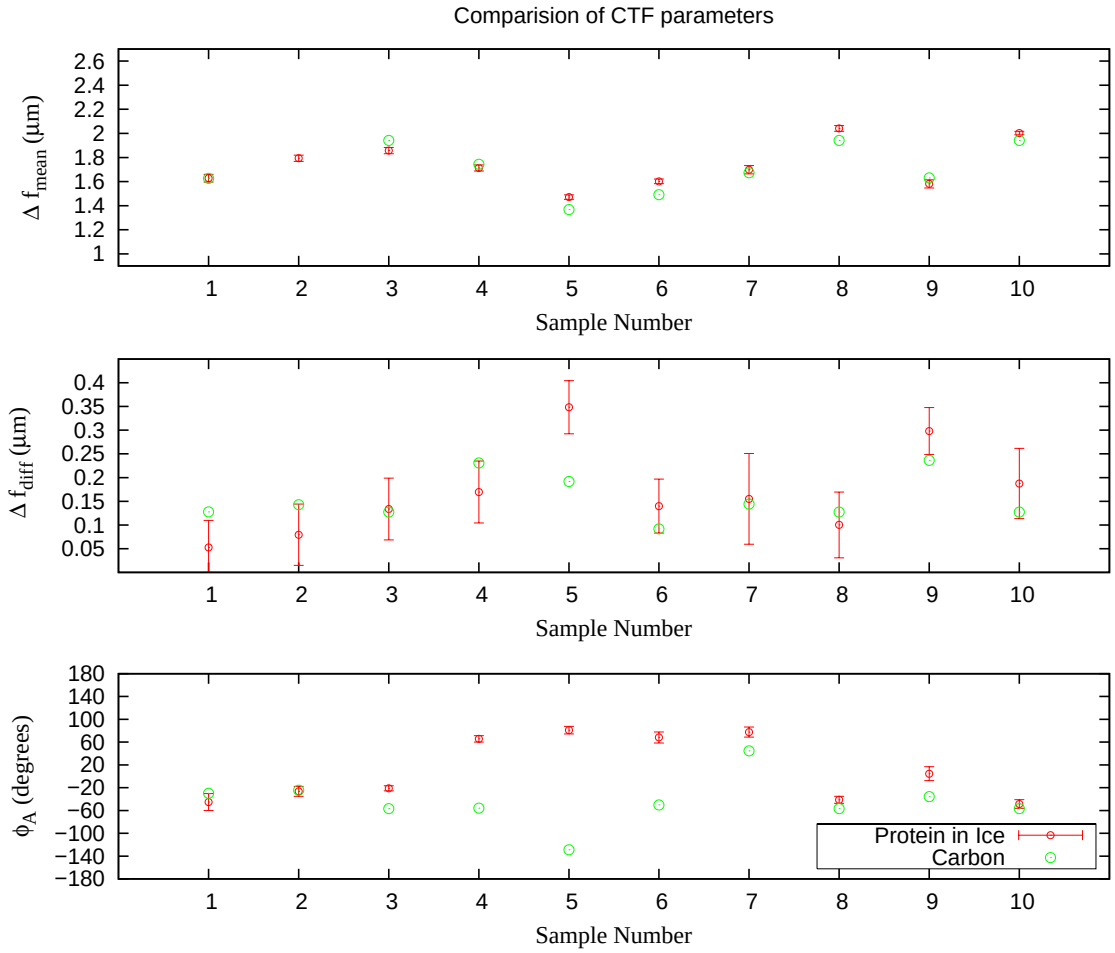

Figure 7.6: Comparision of defocus parameters obtained from 10 measurements on 10 bacterial flagella filament samples embedded in ice with those of carbon film samples from the same micrograph. The mean defocus estimates in ice samples are in excellent agreement with the corresponding carbon film estimates (within 1200$\mathring{A}$). The astigmatism estimates are not reliable or consistent as indicated by the large differences with the carbon film estimates and by the high standard deviation of the Δf_{diff} estimates in ice.

tilt angle was recorded.

7.6.1 CTF Parameter Estimation of Negatively Stained Conical Tilt Data

We estimated the CTF parameters of 57 negative stained conical tilt images that were imaged at 62,000 magnification at at a dosage of 5-10 electrons per $\mathring{A}^2$. The tilt angle of all these images was known to be nominally tilted to about 60° and the rotation axis was rotated about 2° with respect to the Y axis ($\theta_{rot} = 2°$). The amplitude contrast parameter was set at 15%, the typical value for negatively stained data.

The CTF parameters and the mean defocus at the rotation axis (Δf_o) were estimated. Since the defocus at the rotation axis, Δf_o, varied for the image samples, Δf_o was subtracted from the mean defocus estimates resulting in offset adjusted defocus estimates. From (7.6) the subtraction leads to the following equation

$$\underline{\Delta} f_{x,y,z} \equiv \Delta f_{x,y,z} - \Delta f_o = x \tan 60° \tag{7.14}$$

where $\underline{\Delta} f_{x,y,z}$ is the offset adjusted defocus estimate.

When the CTF is estimated at points on a line perpendicular to the rotation axis, the $\underline{\Delta} f_{x,y,z}$ estimates for all image samples should theoretically lie on a line of slope tan(60°), independent of the mean defocus at the rotation axis (Δf_o).

The solid line in Figure 7.7 indicates the theoretical estimate of $\Delta f_{x,y,z}$ as a function of the distance from the rotation axis while the error bars indicate the average mean defocus and the standard deviations of the 57 image samples estimated for stripes parallel to the rotation axis. The correlation coefficient between the theoretical and estimated values is 0.952 and the tilt angle of the samples obtained from the least squares fit of the average mean defocus estimates is 63.14°. The close agreement between the theoretical and estimated values of defocus and tilt angle

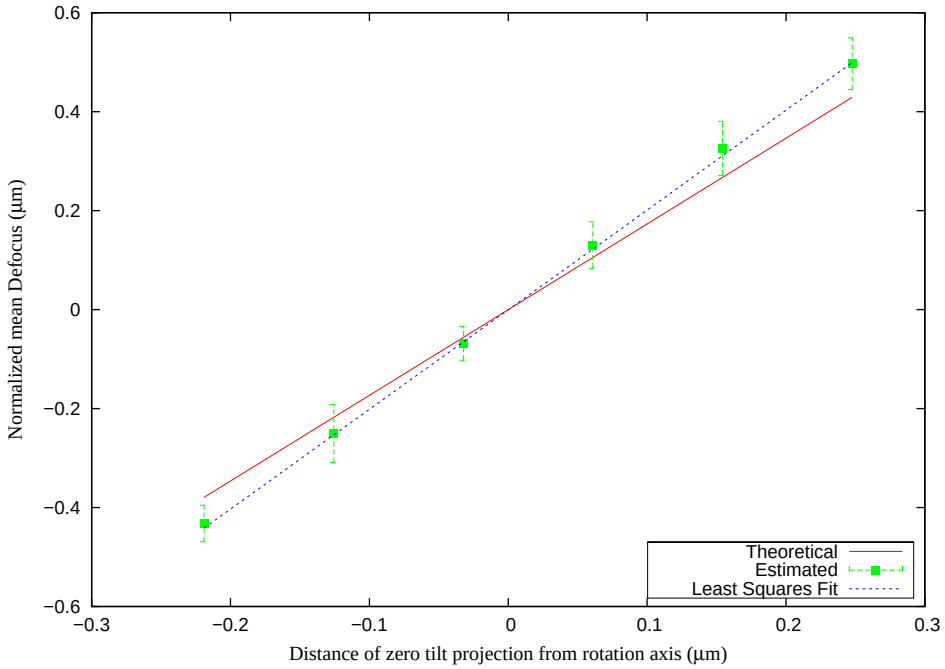

Figure 7.7: Plot of theoretical and estimated offsets vs. distance from the rotation axis for 57 negatively stained image samples tilted to 60°. The solid line indicates the theoretical defocus while the points indicate the average defocus estimate obtained for stripes parallel to the rotation axis. The error bars represent the standard deviation of the estimates. The correlation coefficient between the theoretical and the estimated defocus is 0.952 indicating a high degree of agreement. The small error bars indicate that the estimates are stable across the entire dataset. The slope of the least squares fit through the average defocus estimates is tan(63.14°) which is close to the theoretical value of tan(60°).

indicate that the CTF estimation was successful.

7.6.2 Tilted Defocus Series Experiment with Cryo-EM Data

The defocus series experiment as described in Sec. (7.5.1) was repeated for a specimen of tobacco mosaic virus (TMV) tilted to 45°. The nominal defocus was changed incrementally from 1.44 μm to 8 μm keeping astigmatism constant. At each nominal defocus, the CTF parameters were estimated for an image recorded at a magnification of 61,000 with a dose of 5 electrons per $\mathring{A}^2$.

Figure 7.8 shows a plot of measured mean defocus at the rotation axis and nominal defocus. The correlation between the points and the least squares fit was 0.997

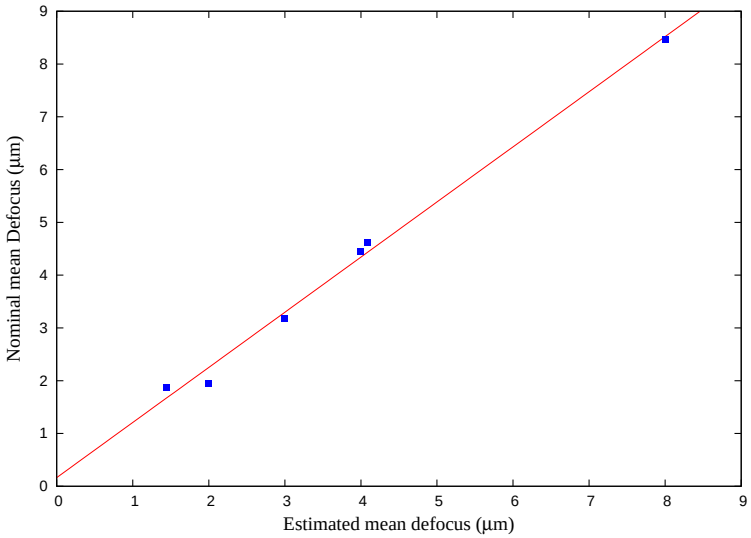

Figure 7.8: Estimated mean defocus at rotation axis versus nominal mean defocus for Cryo-EM tilted series data. The specimen was rotated to 45°. The CTF parameters were determined for the projection of the specimen at the rotation axis at different nominal defocii. The x-intercept of the plot is -0.156 μm which is the estimate of the absolute error in the nominal defocus value obtained from the microscope setting. The slope of the line is 1.045 and the correlation coefficient between the points and the least squares fit is 0.997 indicating that the quality of the fit is good.

showing that the measured defocus accuracy at the rotation axis is good. The zero error in the nominal defocus value is estimated to be -0.156 μm as indicated by the x-intercept of the plot.

7.6.3 Estimation of CTF on Tomographic Cryo-EM data

We performed tomographic CTF estimation for 4 image stacks of Tobacco Mosaic Virus (TMV) data. Each stack consisted of 61 projections of the sample which was tilted from $-60°$ to $+60°$ at a final magnification of 62,000 and a dose of 1 electron per $\mathring{A}^2$ per projection. The estimation was repeated 10 times to measure the consistency of the CTF parameter estimates.

In Figure 7.9, the mean defocus estimate at the rotation axis for each tilt of the image stack, Δf_o is plotted against the tomographic slice number for an image stack. Though ideally a constant value of Δf_o is expected across all tilt angles, a significant

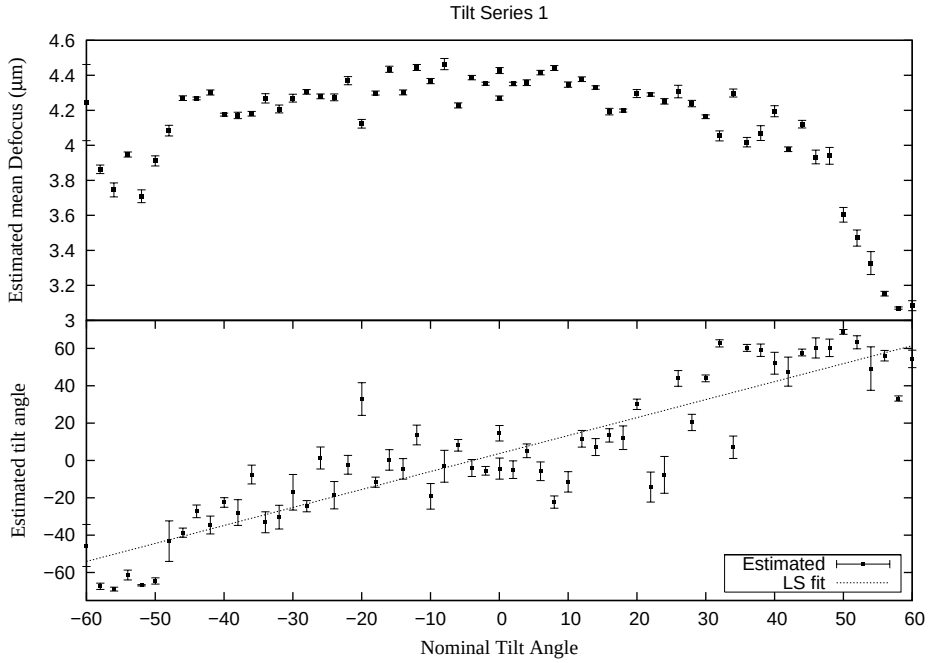

Figure 7.9: Plots of Δf_o (mean defocus at rotation axis) and θ_{tilt}(tilt angle) versus slice number for a stack of tomographic cryo-EM data. The change in Δf_o with tilt angle is due to eucentricity and specimen thickness. The tilt angle estimate agrees closely with the nominal tilt indicating that the tilt angle was estimated correctly. The least squares fit over the tilt angle estimates (*LS fit*) closely follows the nominal tilt angle over the tilt series.

shift in estimated defocus shift was observed over the projections in the tilt series. This shift can be ascribed to errors in sample eucentricity and specimen thickness [94]. The standard deviation of Δf_o was close to 0.01 μm across a range of defoci indicating that the estimate was very consistent. The tilt angle was estimated for every projection and is plotted against the nominal tilt. The standard deviation in the tilt angle estimates was usually less than 5° though it was as high as 10° for a few projections. The close agreement of the least squares fit through the estimated tilt angle with the nominal tilt angle lends credence to accuracy of our algorithm. Normally, the known value of the sample tilt would be used as it is more accurate than that calculated from the data.

7.7 Discussion

We have implemented an automatic CTF estimation algorithm. Unlike other algorithms [57, 77, 52, 34] the estimation of the defocus parameters is completely done in 2 dimensions. No initial guess of the CTF is needed as the algorithm generates an initial guess by performing a coarse grid search covering for the mean defocus, differential defocus and orientation of the astigmatism over the entire parameter range in a total of 256 sample points.

For negative stained specimens and for ice samples backed by carbon film, the algorithm performed quite well. The defocus values were in close agreement to the values obtained from the algorithms of Tani et al. and Mullick et al. [77, 52]. The algorithm was also able to accurately measure the mean defocus for protein specimens embedded in ice without a carbon film. In these cases, astigmatism values should be taken from adjacent carbon film areas.

Reliable and accurate defocus estimates were found for tilted images, either random conical tilt or tomographic data. Due to the low SNR , the tilt angle estimates for cryo EM tomographic data varied by up to 10°. However, in practice the tilt angle is known quite accurately, and thus we can use this information to provide an even more accurate estimate of Δf_o. At present, the algorithm neither estimates the amount of amplitude contrast nor does it estimate the envelope function. Reasonable estimates exist for the magnitude of the amplitude contrast, and to date, the envelope function is not used by CTF correction algorithms. While the current approach is quite effective, the background estimation step could be further improved, perhaps by using limited Bessel functions to minimize the number of parameters, but allow smooth variation with angle. We are presently working on alternative optimization

functions and improved handling of envelope and background functions.

The program was developed on Python, an open source platform, and is freely available from the authors.

CHAPTER VIII

Edge-preserving deconvolution for cryo-electron microscopy images

8.1 Introduction

Cryo-electron microscopy (cryo-EM) is a powerful method for observing macromolecular complexes in their native states. Under typical conditions, cryo specimens are imaged at moderate values of defocus to produce sufficient contrast. While necessary, the defocus and spherical aberration of the objective lens introduce significant distortions into the image that must subsequently be corrected. The image formation process can be mathematically modeled as a convolution of the object being imaged with the imaging system's Contrast Transfer Function (CTF), which characterizes the fidelity by which spatial information is transferred from input to output across a range of spatial frequencies [52, 72, 14, 57]. As a result, *deconvolving* the image by the CTF - or "CTF correction" - is essential for obtaining accurate, high-resolution object information [14].

Typically, images are deconvolved using one of two approaches: (1) phase flipping algorithms, that deconvolve the image by assuming the CTF has a constant amplitude and (2) algorithms such as Wiener filters which attempt to correct for amplitude and phase changes, Such simple linear filters can be considered as members of a more general class of regularized least squares deconvolution algorithms

[49, 56, 14, 19, 6]. *Regularization* refers to the inclusion of information about the object being imaged in order to obtain a stable and useful solution [63]. Both phase flipping and Wiener filtering suffer from significant drawbacks. On the one hand, phase flipping does not correct for the amplitude distortions due to the CTF thereby underemphasizing selective spatial frequencies in the reconstruction. On the other hand, most regularized least squares methods such as Wiener filters and quadratic gradient regularizers tend to yield oversmooth solutions that blur out object edges [39, 31, 27, 17]. While algorithms that combine Wiener filtering and phase flipping have been proposed [56, 80], they ultimately suffer from the same problems. Hence, there is a need for an algorithm that deconvolves the image by the CTF and at the same time, optimally preserves high frequency object information.

While the application of deconvolution algorithms for resolution enhancement is relatively new to electron microscopy, it is a well established technique in the signal processing and astronomy community with a history of over 30 years [48, 69, 76]. Recently, a new class of myopic, edge-preserving deconvolution algorithms have been developed that perform demonstrably better than conventional methods for astronomical and optical images [59, 31]. However, until now, these algorithms have not been applied to EM images.

In this chapter, we present an edge-preserving deconvolution algorithm that corrects for the phase and amplitude effects of the CTF and preserves the edges of the object being imaged. First, we briefly review the phase image formation process in EM. Second, we discuss our CTF correction strategy in a mathematical framework. Finally, we describe the methodology of our experiments and demonstrate that our algorithm corrects images by the CTF better than phase flipping with amplitude correction, Wiener filtering and their variants over most resolutions.

8.2 Theory of Image Formation and CTF Correction

8.2.1 Image Formation

The EM phase image formation process is described by the theory of contrast transfer as

$$i(r,\theta) = h(\mathbf{r}) \otimes o(\mathbf{r}) \otimes e(\mathbf{r}) + n \tag{8.1}$$

where $\mathbf{r}$ is the vector of co-ordinates and i,h and o are the image, transfer function of the system and object respectively. The $\otimes$ operator describes the convolution operation. $e(\mathbf{r})$ represents a Gaussian-like function known as the envelope function that describes the reduction in image contrast with increasing spatial frequency due to the coherence of the electron beam, lens current instability, stage drift and measured modulation transfer function (MTF) of the detector [67]. We assume the noise in the system, n is a combination of Poisson noise due to electron-detection and Gaussian noise, e.g., due to detector or scanner electronics and approximate both by using the mixed Gaussian model [46, 31].

Applying the Fourier transform to (8.1) we get

$$I(\mathbf{q}) = CTF(\mathbf{q})O(\mathbf{q})E(\mathbf{q}) + N \tag{8.2}$$

where the term $CTF(\mathbf{q})$ is the contrast transfer function, the Fourier transform of $h(\mathbf{r})$.

The CTF is theoretically well characterized for thin samples and using the weak-phase-weak-amplitude approximation can be expressed as:

$$CTF(\mathbf{q}) = \sqrt{1-\alpha^2}\sin\chi(\mathbf{q}) - \alpha\cos\chi(\mathbf{q}) \tag{8.3}$$

where α is an amplitude contrast factor ($0 \leq \alpha \leq 1$) and $\chi(\mathbf{q})$ is the scattering angle dependent path length difference of the electron wavefront [67]. χ is a parametric function of the spherical aberration of the objective lens, wavelength of electron beam and defocus and astigmatism parameters of the CTF. Thus, the CTF is usually known to a high degree of accuracy as these parameters are either provided by the manufacturer or can be easily determined using CTF estimation algorithms [72, 52, 57, 77].

8.2.2 Deconvolution

As seen in (8.2), the EM image can be considered as a representation of the object distorted by the CTF and the envelope function. In this chapter, we focus only on correcting the errors introduced by the CTF , and thus aim to recover the envelope function filtered version of the object, $O_e(\mathbf{q}) = O(\mathbf{q})E(\mathbf{q})$ from the image. Our concern was that since the envelope function is small at the higher frequencies, its deconvolution could lead to an amplification of high frequency signals where the noise power spectrum dominates the signal power spectrum leading to unstable and noisy object estimates [14].

There are two common deconvolution strategies currently used to process EM imaging data. The first, phase flipping, corrects for the phase effects of the CTF by reversing the phase of the image Fourier transform in regions of the frequency plane where the CTF is negative. This approach implicitly assumes that the amplitude of the CTF is a non-zero constant at all frequencies; although conservative, this assumption is, of course, not accurate. The second class of methods correct for the CTF in a regularized least squares framework. Here, the object estimate $\hat{o}_e(\mathbf{r})$ is given by that choice of $o_e(\mathbf{r})$ which minimizes

$$\|i(\mathbf{r}) - o_e(\mathbf{r}) \otimes h(\mathbf{r})\|^2 + \lambda_R R \tag{8.4}$$

Here, λ_R is a constant known as the regularization parameter and R is the regularization factor. When $R = \|o_e(\mathbf{r})\|^2$, we aim to keep the object estimate $\hat{o}_e(\mathbf{r})$ small by penalizing large solutions of $o_e(\mathbf{r})$. For this choice of R, the object estimate minimizing (8.4) can be expressed as,

$$\hat{o}_e(\mathbf{r}) = FT^{-1}(I(\mathbf{q})W(\mathbf{q})) \tag{8.5}$$

where

$$W(\mathbf{q}) = \frac{CTF^*(\mathbf{q})}{\mid CTF(\mathbf{q}) \mid^2 + \lambda_R} \tag{8.6}$$

is known as the Wiener filter [6, 95, 50].

Other choices for R are empirically derived from the observation that natural object surfaces are generally smooth with constant or slowly changing intensities between pixels where as noisy areas are discontinuous exhibiting a rapid change of intensities in neighboring pixels. This property is quantified by the norm of the spatial gradient of the object defined as

$$\|\nabla o(\mathbf{r})\| = \left[(\nabla o_x(\mathbf{r}))^2 + (\nabla o_y(\mathbf{r}))^2\right]^{\frac{1}{2}} \tag{8.7}$$

The choices $R = \frac{1}{2}\sum_{\mathbf{r}} \|\nabla o_e(\mathbf{r})\|^2$ and $R = \sum_{\mathbf{r}} \|\nabla o_e(\mathbf{r})\|$ represent quadratic and linear gradient regularizers which penalize gradients in the image.

Edge-Preserving regularizer

While, both Wiener filtering and quadratic gradient regularizers are effective in smoothing out noise, they tend overcompensate for large gradients caused by edges thereby unnecessarily blurring them. In contrast, linear gradient regularizers do not sufficiently suppress noise, but are effective in preserving edges as they do not over-penalize large gradients. Another class of functions, known as Huber functions overcome this problem and act as edge-preserving regularizers by behaving like quadratic gradient regularizers for small gradients and as less severe linear gradient regularizers for large gradients [11]. We use the function originally proposed by Brette and Idier and implemented by Hom et al [7, 31].

$$R = \sum_{\mathbf{r}} \gamma - ln(1+\gamma) \tag{8.8}$$

$$\gamma = (\frac{\|\nabla o_e(\mathbf{r})\|}{\beta(\mathbf{r})}) \tag{8.9}$$

Here γ is the reduced gradient modulus. When γ is small, $\gamma - ln(1+\gamma) \approx \gamma^2/2$ and when γ is large $\gamma - ln(1+\gamma) \approx \gamma$. Thus, R behaves like a quadratic gradient regularizer when γ is small and as a linear gradient regularizer when γ is large. The terms $\beta(\mathbf{r})$ and λ_R from Eqs. (8.8) and (8.4) are known as the hyperparameters of the object and can be determined automatically. The scheme for estimating these hyperparameters is discussed in greater detail by Hom et al [31].

We note that due to the non-linearity of edge-preserving regularizers, analytical solutions that minimize (8.4) do not exist in general [17]. This necessiates the use of iterative optimization algorithms such as Conjugate Gradients [23] to calculate $\hat{o}_e(\mathbf{r})$.

For the sake of brevity, we shall refer to the deconvolution using the edge preserving regularizer and the quadratic gradient regularizer as the edge-preserving algorithm and the quadratic gradient algorithm respectively.

8.3 Methods

The structure of the R-type bacterial flagella filament was recently resolved to atomic resolution [93] and thus provides an excellent test specimen for exploring image processing methodology. The filament is shaped roughly like a hollow cylinder and made up of helically repeating subunits. The overall architecture is an outer projection and a densely packed core region comprised of two concentric tubes surrounding a central channel, each tube being made up of α-helices running almost parallel to the filament axis.

We compared helical 3-D reconstructions of the R-type bacterial flagellar filament after deconvolving the primary cryo-micrographs using either the edge preserving algorithm or other more conventional techniques with the atomic structure. The reconstructions were qualitatively examined by visual inspection of the core regions and quantitatively compared using amplitude-weighted phase residuals [2] between the deconvolved reconstructions and the reference atomic model.

8.3.1 Sample Preparation and Acquisition

Five cryo-EM micrographs, each containing several straight R-type bacterial flagellar filament images were acquired using an FEI Polara TF-30 Electron Microscope operating at 300 KeV equipped with an UltraCam lens-coupled CCD camera and a post-column energy filter [90]. The chip size of the CCD array was 4096×4096. The images were acquired at a final magnification of 113,000 X at a sampling resolution of 1.33 $\mathring{A}$/pixel.

8.3.2 Image Processing of Individual Samples

Images of five filaments, each filament containing 400 subunits, were isolated from the micrographs. After determining the CTF parameters from the micrographs using the algorithm of Shah et al. [72], each image was deconvolved using the following methods: (1) the edge-preserving algorithm, (2) phase flipping, (3) phase flipping with amplitude correction [80, 56], (4) Wiener filtering, (5) least squares without regularization, and (6) the quadratic gradient least squares algorithm. In the case of the edge-preserving and the quadratic gradient least squares algorithms, (8.4) was minimized using a Constrained Conjugate Gradients algorithm [23] in the framework of the AIDA image deconvolution algorithm [31]. In this framework, the edge-preserving algorithm required approximately 2 minutes for the deconvolution of a 512 by 512 image on a 3 GHz, Pentium 4 computer. The flagella filament was reconstructed in 3-D with the deconvolved images at 10 $\mathring{A}$ resolution using the method described by Yonekura et al. [90]. Figure 8.1 describes the deconvolution and reconstruction process.

8.3.3 Quantitative Analysis

Due to the helically repeating structure, the Fourier transform of bacterial flagellar filaments can be described in terms of a set of Fourier-Bessel layer lines parallel to the equator [56]. The amplitude weighted phase difference between layer-line data of the object and the reference data (calculated from the atomic model) at a given resolution is known as the phase residual error [85, 2]. A low phase error indicates a high degree of similarity between the object and the reference data. Phase residuals become large when noise overwhelms the layer-line information. Here, a phase error of 70° is considered as the noise threshold beyond which the signal is assumed to

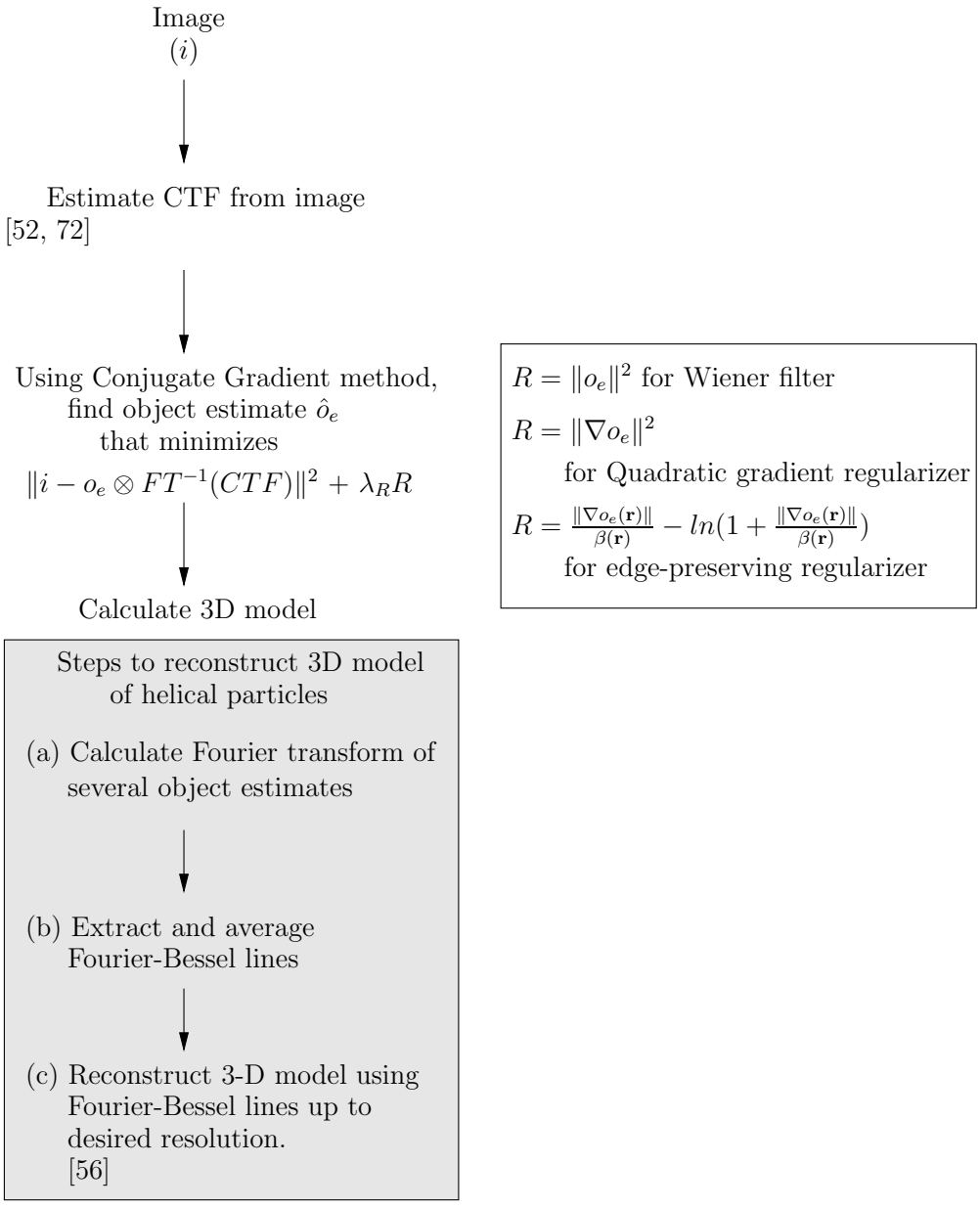

Figure 8.1: Flowchart of deconvolution process.

contain no useful information.

While the Fourier Shell Correlation (FSC) is often the metric of choice for comparing reconstruction quality, we chose the phase residual error over FSC as the comparison metric because of the improved signal to noise afforded by using only the information that falls on layer lines. For our calculations, we used all points with amplitudes larger than 5% of the highest off-equatorial amplitude.

We compared the phase residuals between the averaged layer-lines of the deconvolved micrographs and the reference layer-lines calculated from the atomic model of the R-type bacterial flagellar filaments [92, 93] at resolutions ranging from $(25\mathring{A})^{-1}$ to $(12.5\mathring{A})^{-1}$.

8.3.4 Qualitative Analysis

The 3-D reconstruction of the filaments were visually compared to the atomic model. The quality of the reconstructions were analyzed in three areas: (1) visual similarity of the reconstruction to the atomic model (2) overall noise level in the reconstruction and (3) presence of reconstruction artifacts.

8.4 Results

8.4.1 Analysis of Phase Residual Error

A comparison of phase residual errors calculated between images deconvolved by the various methods and reference layer-line data made from the atomic model [92, 93] is shown in Figure 8.2 Owing to the limited number of filaments used, phase residuals beyond 15 resolution are uniformly high and beyond a reasonably noise threshold. However at all but one of the lower resolutions, the phase residuals were significantly lower for the edge-preserving algorithm than for all of the other deconvolution algorithms. While the quadratic gradient algorithm showed a marked

improvement compared to phase flipping and Wiener filtering, its performance at higher resolutions deteriorated due to its tendency to blur out edges and other high-resolution information. Significantly, all the algorithms performed better than the unregularized least squares deconvolution.

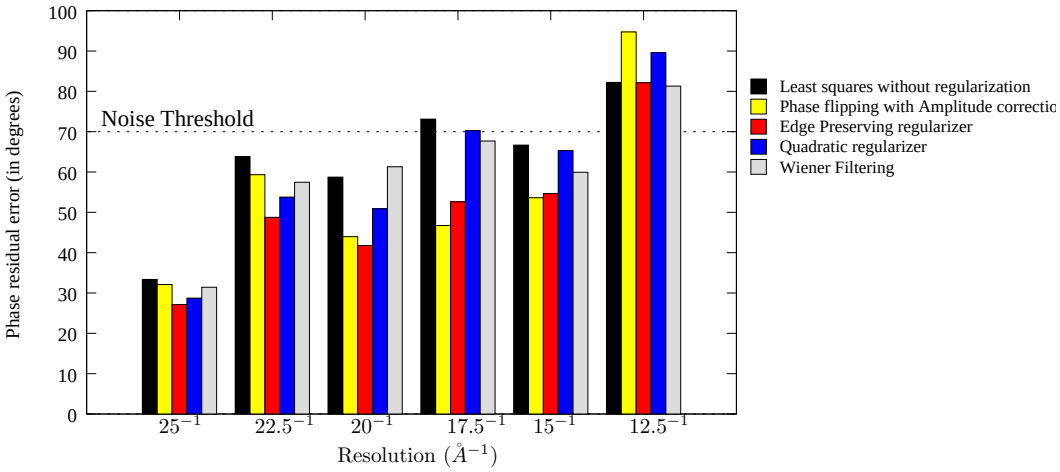

Figure 8.2: Comparison of phase residual errors using edge preserving deconvolution with other methods. The dashed line indicates the threshold above which noise is considered to dominate the signal. The edge-preserving algorithm shows the least overall phase residual error among all the algorithms. Wiener filtering and phase flipping produce comparable results. While both phase flipping with amplitude correction and the quadratic gradient algorithm produce lower phase errors than phase flipping at the lower resolutions, their performance deteriorates at higher resolutions. All algorithms perform better than unregularized least squares at all resolutions below the noise threshold.

8.4.2 Visual Analysis of Data

The central 2-D cross sections of the 3-D reconstructions of the bacterial flagella filaments are shown in Figure 8.3 for (1) the atomic model data, denoted by M,(2) phase flipped and amplitude corrected data denoted by P, and (3) the edge-preserving deconvolution data denoted by E. The two α-helical regions surrounding the core region are highlighted as α_1 and α_2 which are enlarged below to better permit inspection. As seen in the figure, the separation in the α_1 helices is not as clear in the phase flipped and amplitude corrected reconstruction as it is in the edge-preserving deconvolution reconstruction. Similar results were observed in the

α_2 region. In contrast to the α_2 region of the phase flipped and amplitude corrected reconstruction where the α helices appear as poorly resolved stacked disks, the shape of the α-helices in the α_2 region of the edge preserving deconvolution reconstruction appears better preserved.

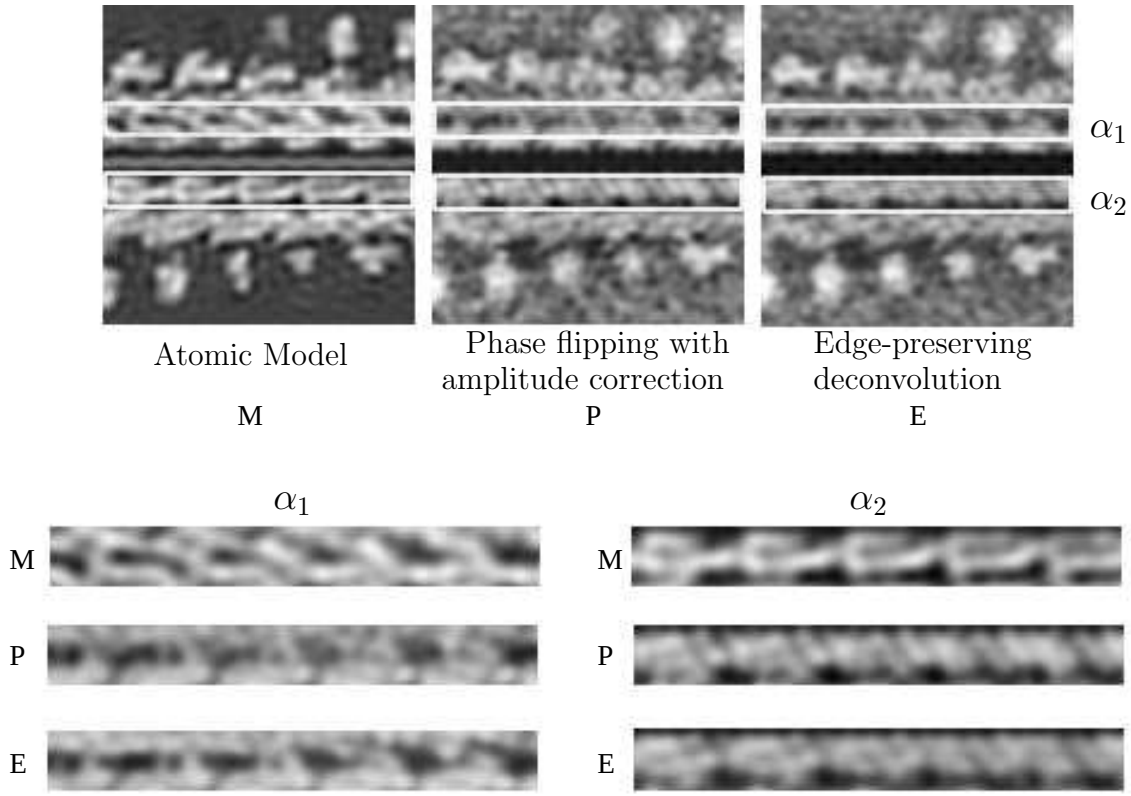

Figure 8.3: A comparison of the cross sections of the 10 $\mathring{A}$ 3D reconstruction of R-type bacteria flagella filament. The top row figure denoted by M is the cross-section of the atomic model. It shows two well separated α helices in the core region indicated by the boxed regions marked by α_1 and α_2. The other top row figures denoted by P and E are obtained after phase flipping with amplitude correction [56] and after edge preserving deconvolution respectively. The columns α_1 and α_2 highlight the α_1 and α_2 regions in the reference, phase flipped and edge preserved reconstructions. From the figures, the α_1 helices appear better separated in the edge preserving deconvolution reconstruction as compared to that obtained from the phase flipped and amplitude corrected version. Further, α_2 helices of edge preserved reconstruction are more evident than the phase flipped image where they appear disk-like in shape.

8.5 Discussion

CTF deconvolution is essential to obtain high-resolution information in cryo-EM. The challenge is to optimally correct for the aberrations introduced by the CTF but to minimize noise amplification. The latter problem is especially significant given the very low signal-to-noise ratio for cryo-EM images. While traditional methods succeed in correcting some of the phase and amplitude effects of the CTF they also introduce artifacts such as oversmooth object edges or they may poorly suppress noise.

We have presented a deconvolution algorithm in the regularized least squares framework that aims to perform both amplitude and phase correction of the CTF while at the same time preserves object edge information and suppresses noise. This is achieved by using a regularizer that behaves like a quadratic gradient regularizer for small gradients, thus suppressing noise, and like a linear gradient regularizer when the gradients are large, thereby preserving edges. Both qualitative and quantitative results indicate that this method produces better results than phase flipping, phase flipping with amplitude correction, Wiener filtering and quadratic gradient regularized deconvolution algorithms.

The algorithm presented in this chapter performs deconvolution on individual 2-D projections before the 3-D reconstruction. A significant advantage of this approach is that operations such as classification and alignment should be greatly facilitated by more accurate image data. While a potential drawback is that any artifacts introduced during the deconvolution stage would be present in the 3-D reconstruction, the results presented here indicate that our approach is considerably more accurate than the alternative methods such as phase flipping or Weiner filtering. Thus

edge-preserving deconvolution should be considered a robust alternative to more conventional CTF correction schemes performed on individual images. A better, albeit more time consuming, approach would be to perform CTF deconvolution as part of the 3-D reconstruction process as demonstrated by Zhu et al. [49] and include edge-preserving regularization to preserve object properties and control noise amplification. We aim to combine the deconvolution and reconstruction steps in the future.

While estimating the electron coherence envelope function can be problematic with cryo-images because it is multiplied by the power spectrum of the sample or carbon-film, the detector MTF is well characterized and can be measured to a high degree of accuracy [49]. As a consequence, including the detector MTF in the overall deconvolution algorithm should provide a relatively simple way to further enhance the results. This is likely to be important when using CCD detectors as their MTFs vary more dramatically with spatial resolution than does film. Once measured, the MTF could be included in the problem formulation along with the CTF to deconvolve out from the image.

CTF deconvolution offers the potential to extend the useful resolution of tomographic and tilted cryo-EM data such as collected for conical tilt reconstructions. Unfortunately, tomographic CTFs vary across the image plane making the deconvolution problem more challenging. Presently, there are two approaches to overcome this issue. The first divides the tilted image into stripes parallel to the rotation axis where the CTF is assumed constant and each section is deconvolved. This approach is problematic for images that are tilted to high angles where the approximation of CTF constancy requires many narrow stripes leading to edge artifacts that can be enhanced by the deconvolution process. Another approach is to perform one-

dimensional deconvolution along stripes parallel to the tilt axis fully accounting for the defocus variation in the CTF due to the tilt [86]. This method assumes that astigmatism is absent in the imaging system.

We are presently adapting the algorithm to account for the MTF and are also directing our efforts in the area of edge preserving deconvolution for cryo-tomographic data.

CHAPTER IX

Conclusion

This thesis can be divided into two parts in terms of approach. In the first part we developed two algorithms for blind deconvolution of images, with an aim to use them for incoherent bio-imaging applications, such as fluorescence microscopy. The first algorithm was developed for imaging systems with even PSFs. Such PSFs are common in optical and fluorescence microscopy. We then extended this algorithm to the 3-D case. Next, we developed a blind deconvolution algorithm based on the QUILL image model, and demonstrated its effectiveness on a variety of images.

The second part of the thesis was primarily concerned with electron microscopy. Two algorithms have also been developed and deployed here. The first algorithm was developed to determine the Contrast Transfer Function (CTF) of electron microscopes automatically from planar and tomographic EM images. The second algorithm was based on an edge-preserving algorithm first demonstrated by Mugnier et al. [59] and later by Hom et al. [31] in the context of optical microscopy and astronomy.

In this final section, we briefly review the pros and cons of the algorithms described in this thesis. Potential extensions of these methods are discussed next.

9.1 Current State of the Algorithms

9.1.1 Blind Even-PSF Deconvolution

The algorithms presented in Chapters III and IV aimed to perform blind deconvolution of 2-D and 3-D images that were convolved with an even PSF. The only assumptions made were the support size of the PSF was known and that the image has finite support. Unlike most other blind deconvolution algorithms that have been developed, this algorithm was non-iterative. The only problem with the algorithm *formulation* was that it was intractable for medium and large sized 2-D images, and almost all 3-D images. This problem was overcome using the Fourier decoupling approach, which simplified the problem from a single large 2-D or 3-D problem to several simple 1-D problems. The only drawback with using Fourier decomposition is that the Mean Square Error (MSE) is slightly increased with respect to the direct approach, due to the necessity of determining scale factors.

However, from both theoretical and practical perspectives, there are a few drawbacks. First, the decoupled version of the algorithm is more sensitive to errors. Here, a bad result in one of the 1-D problems manifests itself in the overall reconstruction during to the recoupling process. Second, the finite support constraint precludes its use in many microscopy applications, where the structures being observed do not have finite support. Third, in most cases, the PSF is not truly symmetric due to lens defects.

Fortunately, PSF symmetry can be assumed for low resolution imaging, since the approximation of symmetry has little effect on the overall reconstruction result at low resolutions. We also note that these algorithms are more applicable in areas such as astronomy, where images having compact support are common (e.g., a nebula on a black background).

9.1.2 Blind Deconvolution using QUILL

Chapter V discussed the QUILL-model-based blind deconvolution algorithm. The key assumption here is that the QUILL model is a reasonably good approximation of the object, and that the support size of the PSF is known. This algorithm is also non-iterative, and fast as most of the unknown pixels are found by simple convolution. Unlike the previous algorithm, it can also handle the partial data case (i.e. compact support is not required).

The chief drawback of this method is that many realistic microscopic images do not fit the model very well. This is especially true in high resolution imaging. However, we note that in high speed microscopy objects are often viewed at low resolution and the images thus formed should be modeled well by QUILL.

9.1.3 Contrast Transfer Function (CTF) Estimation Algorithm

While the CTF estimation algorithm discussed in Chapter VI is not the first algorithm in its class, it incorporates many features that make it unique. First, it is one a rare class of fully automatic CTF estimation algorithms for cryo-electron microscopy. This is achieved by using several novel CTF pre-processing steps that eliminate the need for manual input. Second, it is the only algorithm that can estimate the CTF parameters of *tilted* images. This is a significantly harder problem than the planar image case, as the CTF for a tilted image changes across the imaging plane. Third, the program is user-friendly, and has been developed on an Open Source platform that makes it easily extensable for future work.

This algorithm can be improved by changing some of the pre-processing steps. The background fitting is presently done in an inelegant partial 2-D curve-fit. A better approach would be to use a fully 2-D approach. We also note that while the

background is modeled as an additive component in the observed CTF, we use a least squares fit that minimizes the sum of squares of the fit with respect to the observed CTF. As a result, the estimated background can be larger at times than the observed CTF. Subtracting of the estimated background often leads to spurious negatively-valued areas in the residual CTF that is used for estimation. This is theoretically incorrect and needs to be rectified.

9.1.4 Deconvolution of EM Images using the edge-preservation Algorithm

The algorithm presented in this paper is an attempt to deconvolve EM images using an edge-preserving regularizer. Our preliminary results indicate that the algorithm performs better than other commonly used "CTF correction" approaches. The algorithm is automatic, and does not need any user input apart from the CTF parameters, which can also be estimated automatically using the previous algorithm.

The main drawback of this algorithm is that it does not include the envelope function as part of the formulation. This might play a significant role at higher resolutions. Unfortunately, due to the low SNR of the sample-set on which the deconvolution was tried, the deconvolution would have amplified high-frequency noise more than it would have restored the object, and consequently would have degraded performance significantly.

While all of the algorithms discussed above have drawbacks, there are several ways in which they could be improved. We discuss some of these, along with more ambitious ideas, in the next section.

9.2 Future Work

9.2.1 Deployment of Blind Deconvolution Algorithms for Fluorescence Microscopy Applications

While both the symmetric PSF algorithm and the QUILL algorithm have shown very promising simulation results, they have yet to be tested on a large number of real deconvolution problems. The symmetric PSF algorithm is well-suited for imaging systems that show small or almost no spherical aberrations, so that the PSF symmetry is maintained. The QUILL algorithm requires that the object be heavily oversampled so that subsequent undersampling does not affect the deconvolution significantly. For this reason, the QUILL algorithm is a good candidate for deconvolution of high speed confocal microscopy images, where the emphasis is not only on performance of the deconvolution algorithm, but also on time taken to deconvolve the image.

9.2.2 Choice of a Different Regularizer for QUILL Algorithm

The QUILL algorithm was demonstrated using a Truncated Singular Value Decomposition method for regularization [63]. The TSVD method is closely related to the Tikhonov method, and is essentially a linear regularization method. These class of methods, while fast, suffer from the resolution-noise tradeoff problem, i.e., if one increases the contribution of the regularizer to remove noise, then the overall image appears blurry. A better way to regularize would be to use a non-linear edge-preserving regularizer, which attempts to remove noise, while at the same time preserving image edges [17].

9.2.3 Improvements and Extensions to CTF Estimation Algorithm

The CTF estimation algorithm can be improved in three key ways.

First, the background estimation step, which is presently done as a partial 2-D

problem, could be implemented as a 2-D curve-fit problem, where a 2-D polynomial could be fit over the entire fit area.

Second, the envelope function and background estimation step is presently fitted using a least squares fit. Given that the background is modelled as an additive function in the observed CTF, the background will be better estimated as a constrained least squares problem, where the upper bound of the fit is the observed CTF.

Third, the algorithm does not calculate the envelope function of the CTF. This can easily be done using a constrained least squares approach.

Another related potential area of improvement would be to provide a better graphics front end for ease of use for electron microscopists.

9.2.4 Improvements to the Edge-Preserving Deconvolution Algorithm

While the edge-preserving algorithm presented in Chapter VI is promising, the results presented are only preliminary. It needs to be applied to the deconvolution of a variety of structures to be accepted in the EM community. There are also three ways in which the algorithm may be improved.

First, the envelope function must be part of the problem formulation. While the envelope function does not play a big role at lower resolutions, where it is mostly flat, it rapidly decays at the higher resolutions affecting the high-frequency object information. One way to incorporate this would be use many more images (50-100), so that the SNR of the data at high resolutions is good enough to deconvolve by the envelope function.

Second, unlike AIDA or MISTRAL [31, 59], the algorithm is not myopic. Given that CTF estimation may yield transfer function parameters that are not as accurate [52], a myopic approach to deconvolution may correct the CTF slightly to give a better object estimate.

Third, and perhaps most ambitious, is that algorithm could be adapted for use for tomographic data. This is especially difficult because the CTF changes across the imaging plane, so the deconvolution is no longer spatially invariant. Two approaches currently exist to deal with this issue, both making approximations to simplify the problem. One approach breaks up the imaging plane where the CTF is assumed constant in each plane, while the other approach assumes the CTF does not have astigmatism [86]. If it is possible to model the problem where the CTF and image over the entire plane are considered, the solution, apart from being more elegant, would theoretically be better.

Several potential future improvements discussed here are challenging. However, they offer the promise of being rewarding, especially to the microscopy community.

APPENDICES

APPENDIX A

Derivation of tomographic CTF formula

We assume the origin of the coordinates is at the center of the object plane and is marked by O. O_s is the center of the specimen plane. The sample is tilted by θ_{tilt} with respect to the object plane. The rotation axis r' passes through O_s and is rotated θ_{rot} with respect to the y-axis, as shown in Fig. (A.1). The mean defocus of a point is defined as the distance of the point on the specimen plane to the object plane. So, the z-ordinate Δf_o of O_s denotes the mean defocus at the rotation axis.

$U(x_1, y_1, z_1)$ is an arbitrary point on the specimen where we wish to measure the mean defocus. If $p(x_1, y_1, \theta_{rot})$ is the projection of the distance between a point on the specimen plane and the rotation axis on the zero tilt plane, then

$$p(x_1, y_1, \theta_{rot}) = x_1 \cos\theta_{rot} + y_1 \sin\theta_{rot} \tag{A.1}$$

Δf and $p(x_1, y_1, \theta_{rot})$ are related as

$$\Delta f = p(x_1, y_1, \theta_{rot}) \tan\theta_{tilt} \tag{A.2}$$

The defocus at $U(x_1, y_1, z_1)$ is

$$\Delta f_{x_1,y_1,z_1} \equiv z_1 = \Delta f + \Delta f_o \tag{A.3}$$

Applying Eqs. A.1, A.2 and A.3, the mean defocus at $U(x_1, y_1, z_1)$ is given by

$$\Delta f_{x_1,y_1,z_1} = (x_1 \cos\theta_{rot} + y_1 \sin\theta_{rot}) \tan\theta_{tilt} + \Delta f_o \tag{A.4}$$

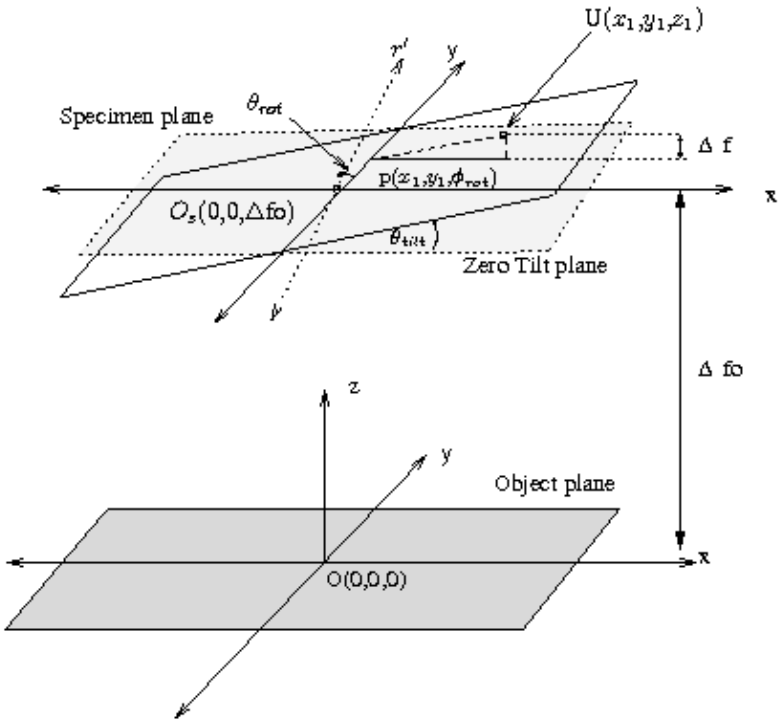

Figure A.1: Defocus determination for a point $U(x_1, y_1, z_1)$ for a tilted image. O is the origin of the coordinates. r' is the rotation axis which is rotated θ_{rot} with respect to the y-axis. $p(x_1, y_1, \theta_{rot})$ is the distance of the projection of $U(x_1, y_1, z_1)$ from the rotation axis on the zero tilt plane.

BIBLIOGRAPHY

BIBLIOGRAPHY

[1] D. Agard, "Optical sectioning microscopy: cellular architecture in three dimensions," *Annual Reviews in Biophysics and Bioengineering*, vol. 13, pp. 191–219, 1984.

[2] L. Amos and A. Klug, "Three-dimensional image reconstruction of the contractile tail of T4 bacteriophage," *Journal of Molecular Biology*, vol. 99, pp. 51–73, 1975.

[3] Andrews and Hunt, "Digital image restoration," *Prentice Hall*, 1974.

[4] R. Aster, B. Borchers, and C. Thurber, "Parameter estimation and inverse problems," *Elselvier Academic Press*, 2004.

[5] J. Besag, "On the statistical-analysis of dirty pictures," *J Royal Statistical Society B*, vol. 48, pp. 259–302, 1986.

[6] J. Biemond, R. L. Lagendijk, and R. M. Mersereau, "Iterative methods for image deblurring," *Proceedings of the IEEE*, 1990.

[7] S. Brette and J. Idier, "Optimized single site update algorithms for image deblurring," *Image Processing, Proceedings., International Conference on*, vol. 3, pp. 65–68, 1996.

[8] J. Cadzow, "Signal enhancement-a composite property mapping algorithm," *IEEE Transactions on Signal Processing*, vol. 36, no. 1, pp. 49–63, 1988.

[9] A. Carasso, "Linear and nonlinear image deblurring: A documented study," *SIAM Journal on Numerical Analysis*, vol. 36, no. 6, pp. 1659–1689, 1999.

[10] P. Charbonnier, L. Blanc-Feraud, G. Aubert, and M. Barlaud, "Deterministic edge-preserving regularization in computed imaging," *IEEE Transactions on Signal Processing*, vol. 44, no. 10, pp. 2464–2474, 1996.

[11] ——, "Deterministic edge preserving regularization in computed imaging," *IEEE Transactions in Image Processing*, vol. 6, no. 2, pp. 298–311, 1996.

[12] J. Conan, L. Mugnier, T. Fusco, V. Michau, and G. Rousset, "Myopic deconvolution of adaptive optics images by use of object and point-spread function power spectra," *Appl. Opt.*, vol. 37, pp. 4814–4622, 1998.

[13] J. Conchello and J. McNally, "Fast regularization technique for expectation maximization algorithm for optical sectioning microscopy," *Symp. Electronic Imaging Sci. Technol. San Jose, CA 2655*, pp. 199–208, 1996.

[14] J. F. Conway and A. C. Steven, "Methods for reconstructing density maps of "'single"' particles from cryoelectron micrographs to subnanometer resolution," *Nature*, vol. 424, pp. 643–650, 2003.

[15] H. P. Erikson and A. Klug, "The fourier transform of an electron micrograph: Effects of defocussing and aberrations, and implications for the use of underfocus contrast enhancement," *Ber. Bunsenges. Phys. Chem.*, 1970.

[16] J.-J. Fernandez, J. R. Fernandez, and J.-M. Fernandez, "A spectral estimation approach to contrast transfer function detection in electron microscopy," *Ultramicroscopy*, 1997.

[17] J. Fessler, *Image Reconstruction: Algorithms and Analysis*. Book in Preparation, 2006.

[18] J. Fienup, "Phase retrieval algorithms: A comparison," *Appl. Opt.*, vol. 21, pp. 2758–2769, 1982.

[19] J. Frank, M. Radermacher, P. Penczek, J. Zhu, Y. Li, M. Ladjadj, and A. Leith, "SPIDER and WEB: Processing and visualization of images in 3D electron microscopy and related fields," *Journal of Structural Biology*, vol. 116, no. 1, pp. 190–199, 1996.

[20] T. Fusco, J. P. Veran, J. Conan, and L. Mugnier, "Myopic deconvolution method for adaptive optics images of stellar fields," *Astron. Astrophys. Suppl. Ser.*, vol. 134, pp. 193–200, 1999.

[21] G. GB and H. RW, "Blind identification of multichannel fir blurs and perfect image resotration," *IEEE Transactions on Image Processing*, vol. 9, no. 11, pp. 1877–1896, 2000.

[22] S. Geman and D. Geman, "Stochastic relaxation, gibbs distribution and bayesian restoration of images," *IEEE Trans. Pattern Anal. Mach. Intell.*, vol. 6, no. 721-741, 1984.

[23] D. M. Goodman, E. M. Johansson, and T. W. Lawrence, "On applying the conjugate gradient algorihm to image processing problems, chapter 11," *Multivariate Analysis: Future Directions: North-Holland Series inStatistics and Probability*, vol. 5, pp. 209–232, 1993.

[24] A. GR and D. JC, "Iterative blind deconvolution method and its applications," *Optics letters*, vol. 13, no. 7, pp. 547–549, 1988.

[25] P. Hansen, "Regularization tools for matlab 6.0," *software*, vol. ver 3.1.

[26] K. J. Hanzen, "The optical transfer theory of the elctron microscope: fundamental principles and applications," *Advanced Optical and Electron Microscopy*, vol. 4, pp. 1–84, 1971.

[27] G. Harikumar and Y. Bresler, "FIR perfect signal reconstruction from multiple convolutions:minimum deconvolver orders," *IEEE Transactions on Signal Processing*, vol. 46, no. 1, pp. 215–218, 1998.

[28] ——, "Perfect blind restoration of images blurred by multiple filters: Theory and efficient algorithms," *IEEE Transactions on Image Processing*, vol. 8, no. 2, pp. 202–219, 1999.

[29] T. Holmes, S. Bhattacharya, J. Cooper, D. Hanzel, V. Krishnamurthi, W. Linand, B. Roysam, D. Szaowski, and J. Turner, "Light microscopic images reconstructed by maximum liklihood deconvolution," *Handbook of Biological and Confocal Microscopy*, vol. 2, 1995.

[30] T. Holmes and N. O'Connor, "Blind deconvolution of 3d transmitted light brightfield micrographs," *Journal of Microscopy*, vol. 200, no. 2, pp. 114–127, 2000.

[31] E. Hom, F. Marchis, S. Haase, T. Lee, D. A. Agard, and J. W. Sedat, "AIDA: An adaptive image deconvolution algorithm with application to multi frame and three-dimensional data," *in preparation*, 2006.

[32] T. Homes, "Maximum-likelihood image restoration adapted for noncoherent optical imaging," *Journal of the Optical Society of America A*, vol. 5, pp. 666–673, 1988.

[33] ——, "Expectation-maximization restoration of band-limited, truncated point-process intensities with application in microscopy," *Journal of Optical Society of America A*, vol. 6, no. 7, pp. 1006–1014, 1989.

[34] Z. Huang, P. R. Baldwin, S. Mullapudi, and P. A. Penczek, "Automated determination of parameters describing power spectra of micrograph images in electron microscopy," *Journal of Structural Biology*, 2003.

[35] S. Huffel, "Tls applications in biomedical signal processing," *Recent Advances in Total Least Squares Techniques and Errors-in-Variables modeling (Van Huffel S,. ed.), SIAM*, pp. 307–318, 1997.

[36] S. Huffel, N. Mastronardi, and P. Lemmerling, "Fast structured total least squares algorithm for solving the basic deconvolution problem," *SIAM Journal of Matrix Analysis and Applications*, vol. 22, pp. 533–553, 2000.

[37] S. Huffel, H. Park, and J. Rosen, "Formulation and solution of structured total least norm problems for parameter estimation," *IEEE Transactions on Signal Processing*, vol. 44, no. 10, pp. 2464–2474, 1996.

[38] A. Jalobeanu, L. Blanc-Fraud, and J. Zerubia, "Satellite image deconvolution using complex wavelet packets," in *ICIP, Vancouver, Canada*, sep 2000.

[39] A. Jalobeanu, L. Blanc-Feraud, and J. Zerubia, "Hyperparameter estimation for satellite image restoration by a MCMCML method," in *Energy Minimization Methods in Computer Vision and Pattern Recognition*, 1999, pp. 115–130. [Online]. Available: citeseer.ist.psu.edu/jalobeanu99hyperparameter.html

[40] J. Jefferies and J. Christou, "Restoration of astronomical images by iterative blind deconvolution," *Astrophysics Journal*, vol. 415, pp. 862–874, 1993.

[41] S. JL, P. E, and M. F, "Deconvolution in astronomy: A review," *Publications of the Astronomical Socienty of the Pacific*, vol. 114, pp. 1051–1069, 2002.

[42] S. Kay, *Modern Spectral Estimation*. Philadelphia: Prentice-Hall, 1998.

[43] K. Krakauer, T. Schneider, J. Randerson, and S. Olsen, "Linear inversion methods and generalized cross validation," *Geophysical Research Letters*, vol. 31, 2004.

[44] D. Kundur and D. Hatzinakos, "Blind image deconvolution," *IEEE Signal Processing Magazine*, vol. 13, no. 3, pp. 43–64, 1996.

[45] ——, "A novel blind deconvolution scheme for image restoration using recursive filtering," *IEEE Transactions on Signal Processing*, vol. 46, no. 2, pp. 375–390, 1998.

[46] R. G. Lane, "Blind deconvolution of images blurred by atmospheric speckle," *Image Reconstruction from Incomplete Data (Proc. SPIE)*, 2000.

[47] P. Lemmerling, S. V. Huffel, and B. D. Moor, "Structured total least squares methods in signal processing," *Proceedings of the 8th European Signal Processing Conference (EUSIPCO'96), Trieste, Italy*, pp. 819–822, Sep. 1996.

[48] L. Lucy, "An iterative technique for the rectification of observed distributions," *Astronomy Journal*, vol. 74, pp. 745–754, 1974.

[49] S. J. Ludtke, P. R. Baldwin, and W. Chiu, "Three-dimensional reconstruction with contrast transfer function correction from energy-filtered cryoelectron micrographs: Procedure and application to the 70s escherichia coli ribosome," *Journal of Structural Biology*, 1997.

[50] ——, "Eman: semiautomated software for high resolution single-particle reconstructions," *Journal of Structural Biology*, 1999.

[51] G. M, *Principles of Three-Dimensional Imaging in Confocal Microscopes*. World Scientific Pub Co Inc, 1998.

[52] S. P. Mallick, B. Carragher, C. S. Potter, and D. J. Kriegman, "ACE:automated CTF estimation," *Ultramicroscopy*, 2005.

[53] J. Markham and J.-A. Conchello, "Parametric blind deconvolution: A robust method for the simultaneous estimation of image and blur," *Journal of the Optical Society of America-A*, vol. 16, pp. 2377–2391, 1999.

[54] J. Markham and J. Conchello, "Fast maximum-likelihood image-restoration algorithms for threedimensional fluorescence microscopy," *Journal of Optical Society of America A*, vol. 18, no. 5, pp. 1062–1071, 2001.

[55] J. McNally, T. Karpova, J. Cooper, and J.-A. Conchello, "Three dimensional imaging by deconvolution microscopy," *Methods in Microscopy*, vol. 19, no. 3, pp. 1898–1904, 1999.

[56] Y. Mimori, I. Yamashita, M. Kazuyosh, Y. Fujiyoshi, K. Yonekura, C. Toyoshima, and K. Namba, "The structure of the r-type straight flagellar filament of salmonella at 9 a resolution by electron cryomicroscopy," *Journal of Molecular Biology*, 1995.

[57] J. Mindell and N. Grigorieff, "Accurate determination of local defocus and specimen tilt in electron microscopy," *Journal of Structural Biology*, vol. 142, pp. 334–347, 2003.

[58] D. L. Misell, "On the validity of the weak phase and other approximations in the analysis of electron microscope images," *J Phys. D:Appl Phys*, 1976.

[59] L. Mugnier, T. Fusco, and J. Conan, "MISTRAL: a myopic edge-preserving image restoration method, with application to astronomical adaptive-optics-corrected long-exposure images," *Journal of the Optical Society of America A*, 2004.

[60] R. Narayan and R. Nityananda, "Maximum entropy image restoration in astronomy," *Annual Review of Astronomy and Astrophysics*, vol. 24, 1986.

[61] A. Oppenhiem and R. Schafer, *Digital Signal Processing.* Prentice Hall, Englewood Cliffs, 2000.

[62] G. Panci, P. Campisi, S. Colonnese, and G. Scarano, "Multichannel blind image deconvolution using the bussgang algorithm: Spatial and multiresolution techniques," *IEEE Transactions on Image Processing*, vol. 12, no. 11, pp. 1324–1337, 2003.

[63] H. PC, *Rank-Deficient and Discrete Ill-Posed Problems: Numerical Aspects of Linear Inversion.* Philadelphia: SIAM, 1998.

[64] C. S. Potter, H. Chu, B. Frey, C. Green, N. Kisserberth, T. J. Madden, K. L. Miller, K. Nahrstedt, J. Pulokas, A. Reilein, and et al., "Leginon: A system for fully automated acquisition of 1000 micrographs a day," *Ultramicroscopy*, pp. 153–161, 1999.

[65] A. Pruessner and D. O'Leary, "Blind deconvolution using a regularized structured total least norm algorithm," *SIAM Journal on Matrix Analysis and Applications*, vol. 24, no. 4, pp. 1018–1037, 2003.

[66] M. Radermacher, "Three-dimensional reconstruction of single particles from random and nonrandom tilt series," *Journal of Electron Microscopy Technique*, 1988.

[67] L. Reimer, *Transmission Electron Microscopy: Physics of Image Formation and Microanalysis.* Springer Series in Optical Sciences, 1997.

[68] B. Richardson, "Bayesian based iterative method of image reconstruction," *Journal of the Optical Society of America*, vol. 62:55, 1972.

[69] W. Richardson, "Bayesian-based iterative method of image restoration," *Journal of the Optical Society of America*, pp. 55–59, 1972.

[70] H. SB, *Handbook of CCD astronomy.* New York: Cambridge University Press, 2000.

[71] S. Shah and A. Yagle, "2-d blind deconvolution of even point-spread functions from compact support images," *Internal Report*, 2002.

[72] S. Shah, E. Hom, K. Yonekura, D. Agard, and J. Sedat, "Automatic 2-d estimation of defocus parameters for contrast transfer functions," *manuscript in preparation*, 2006.

[73] ——, "Edge preserving deconvolution for cryo-electron microscopy," *Journal of Microscopy*, 2006.

[74] L. Shepp and Y. Vardi, "Maximum liklihood reconstruction in positron emission tomography," *IEEE Transactions on Medical Imaging*, vol. 1, pp. 113–122, 1982.

[75] F. Sroubek and J. Flusser, "Multichannel blind iterative image restoration," *IEEE Transactions on Image Processing*, vol. 12, no. 9, pp. 1094–1106, 2003.

[76] J. Stark and J. Bijaoui, "Multiresolution deconvolution," *Journal of the Optical Society of America A*, vol. 11, no. 5, pp. 1580–21 588, 1994.

[77] K. Tani, H. Sasabe, and C. Toyoshima, "A set of computer programs for determining defocus and astigmatism in electron images," *Ultramicroscopy*, vol. 65, pp. 31–44, 1996.

[78] F. Thon, "Phase contrast electron microscopy, electron microscopy in materials," *Ultramicroscopy*, pp. 570–625, 1971.

[79] C. Toyoshima and K. Yonekura, "Contrast transfer for frozen hydrated specimens ii. amplitude contrast at very low frequencies," *Ultramicroscopy*, vol. 48, pp. 165–176, 1993.

[80] N. Unwin, "Nicotinic acetylcholine receptor at 9 A," *Journal of Molecular Biology*, vol. 229, pp. 1101–1124, 1993.

[81] G. van Kempen, "Image restoration fluorscence microscopy," *PhD. Thesis*, 1998.

[82] M. Vetterli and J. Kovacevic, *Wavelets and Subband coding*. Prentice Hall PTR, 1995.

[83] C. Wackerman and A. Yagle, "Use of fourier domain real-plane zeros to overcome a phase retrieval stagnation," *J. Opt. Soc. Am. A*, vol. 8, no. 12, pp. 1898–1904, 1991.

[84] R. H. Wade, "A brief look at imaging and contrast transfer," *Ultramicroscopy*, vol. 46, pp. 145–156, 1992.

[85] T. Wakabayashi, H. Huxley, L. Amos, and A. Klug, "Three dimensional image reconstruction of actin-tropomyosin complex and actin-tropomyosin-troponin t-troponin i complex," *Journal of Molecular Biology*, vol. 93, pp. 477–497, 1975.

[86] H. Winkler and K. A. Taylor, "Focus graident correction applied to tilt series image data used in electron tomography," *Journal of Structural Biology*, 2003.

[87] A. Yagle, "New analogues of split algorithms for arbitrary toeplitz-plus-hankel matrices," *IEEE Tran. on Sig. Proc.*, vol. 39, no. 11, pp. 2457–2463, 1991.

[88] A. Yagle and S. Shah, "3-d blind deconvolution of even point-spread functions from compact support 3-d images," *SPIE Proceedings*, 2004.

[89] ——, "2-d blind deconvolution from partial data using bezout's lemma and the quill model," *IEEE Trans. Image Proc.*, 2006.

[90] K. Yonekura, M. B. Braunfeld, S. Maki-Yonekura, and D. A. Agard, "Electron energy filtering significantly improves amplitude contrast of thin frozen hydrated protein at 300 kV," *submitted, Journal of Structural Biology*, 2006.

[91] K. Yonekura, S. Maki-Yonekura, and K. Namba, "Complete atomic model of the bacterial flagellar filament by electron cryomicroscopy," *Nature*, vol. 424, pp. 643–650, 2003.

[92] ——, "Complete atomic model of the bacterial flagellar filament by electron cryomicroscopy," *Nature*, vol. 424, pp. 643–650, 2003.

[93] ——, "Building the atomic model for the bacterial flagellar filament by electron cryomicroscopy and image analysis," *Structure*, vol. 13, no. 3, pp. 407–412, 2005.

[94] Q. S. Zheng, M. B. Baunfeld, J. W. Sedat, and D. A. Agard, "An improved strategy for automated electron microscopic tomography," *Journal of Structural Biology*, 2004.

[95] J. Zhu, P. A. Penczek, R. Schroder, and J. Frank, "Three dimensional reconstruction with contrast transfer compensation from defocus series," *Scanning Microscopy*, 1997.

ABSTRACT

DECONVOLUTION ALGORITHMS FOR FLUORESCENCE AND ELECTRON MICROSCOPY

by

Siddharth Shah

Chair: Andrew E. Yagle

In many imaging applications the image formation process is influenced by the device physics of the imaging system. As a result, the image is a distorted version of the object. This distortion effect, mathematically modeled as the transfer function, ultimately limits the resolution of the imaging system. In a high-resolution imaging system, this limitation needs to be overcome either by improving the imaging hardware or by computational post-processing of the image. Deconvolution refers to the class of computational methods that aim to improve the resolution of the observed image by reversing the effect of the transfer function. The focus of this thesis is in the development and deployment of deconvolution algorithms for microscopy applications.

The first part of this thesis discusses two novel deconvolution algorithms that have been developed from a deterministic approach. The key feature of both the

algorithms is that they require no prior information about the transfer function of the imaging system. Instead, they make two key assumptions: The first algorithm assumes that the transfer function of the imaging system is symmetric, a reasonable assumption for many optical microscopy systems, while the second algorithm assumes that the image formed is highly oversampled, a valid assumption for some high-resolution fluorescence microscopy applications.

The second part of this thesis deals with deconvolution algorithms for cryo electron microscopy (cryo-EM). This is a more difficult problem than deconvolution of fluorescence microscopy images, due to the extremely low signal-to-noise ratio of cryo-EM images (typically less than 0 dB). We first present an automatic transfer function estimation scheme for planar and tomographic EM data. We use this in the development of an edge-preserving deconvolution algorithm for cryo-EM data. Preliminary experiments on bacteria flagella filaments indicate that the edge-preserving deconvolution algorithm provides better 3-D reconstructions than present state of the art algorithms in the EM field.